Characterization of Fiber Bragg Grating Sensor Array Embedded in Composite Structures

Yu Fan

A Thesis

in

The Department

of

Electrical and Computer Engineering

Presented in Partial Fulfillment of the Requirements
for the Degree of Master of Applied Science
(Electrical and Computer Engineering) at
Concordia University
Montreal, Quebec, Canada

June 2004

Your file Votre référence
ISBN: 0-612-94697-5
Our file Notre référence
ISBN: 0-612-94697-5

ABSTRACT

Characterization of Fiber Bragg Grating Sensor Array

Embedded in Composite Structures

Yu Fan

FBG (fiber Bragg Grating) sensor becomes a hotspot in recent researches, based on its numerous advantages, especially it can be easily multiplexed to realize sensor network. A number of networking scenarios have been proposed [1] [2], "orthogonal array" is one of the most convincing solutions, in which wavelength division multiplexed FBG sensors are patterned along a single optical fiber and analogical fibers are orthogonally deployed, so that any randomly oriented ambient change can be analytically monitored along two orthogonal sensors of local intersection. Further, by means of various addressing mechanisms [3], stimulus is positioned. However, detailed characterization of a single orthogonal unit is the essence to model entire network.

Fiber reinforced composite materials are always regarded as the most promising candidate to receive FBG sensors upon the fact that, fiber reinforced filamentary topology enables integration of optical fibers within the structure, and effectively protects optical fibers from hostile attack, therefore, a fiber optic smart structure is achievable. Notwithstanding, one must recognize that embedded FBG fibers are foreign entities to host structures, mechanical mismatches may eventually lead to alteration on sensors' responsive behaviors, and measurand interpretation becomes complicated.

This work reports a set of experiments on an orthogonal FBG array unit embedded in specific Graphite/Epoxy composite structure. First of all, photoelastic behaviour of identical bare FBG fiber was observed, which is to profile an "ideal" FBG strain gage. Then optimization process was carried out to determine the optimal layout for FBG array embedment, which induces minimum perturbation to both sensors and host structure. After optimized specimens were fabricated, tensile loads were applied to specimens. Recurring to surface mounted resistance strain gages, embedded FBG strain gages are recalibrated and their sensing alterabilities are evaluated. Finally, suspended concerns are discussed and conclusions are drawn upon experimental data.

This work tends to provide a comprehensive investigation on embedded FBG sensors' strain-optic behaviors, and a quantitative discussion on sensors' inevitable deviations when used as buried strain gages. The results prove the applicability of orthogonal FBG strain sensor network integrated in certain composite structures.

ACKNOWLEDGEMENT

First of all, special thanks are given to Dr. Mojtaba Kahrizi of Electrical and Computer Engineering Department, for his devoting instructions during the entire project.

Meanwhile, thanks must be given to Dr. S. V. Hoa of Mechanical Engineering Department, for his permit to access his lab facilities; Dr. Hoa's PhD student, Mr. Bao Xiao, and technical staff Dr. Ming Xie, for their assistance in composite specimens' fabrication; Mr. Andrew Chociwski and Mr. Danny Roy of Civil Engineering Department, for their permission to use their lab facilities, and provided relative trainings; Dr. Xiupu Zhang of Electrical and Computer Engineering Department, for his permit to use his optical instruments; Mr. Shailesh Prasad and Mr. Guy Gosselin of Electrical and Computer Engineering Department, for their assistance in experiment arrangement; Mr. Jun Chen of Electrical and Computer Engineering Department, for his help in using SEM (Scan Electronic Mirror); Mr. Xiaohong Mu and Mr. Siamak Foulad of Electrical and Computer Engineering Department, for their helps in ANASYS operations.

TABLE OF CONTENTS

TABLE OF CONTENTS (continued)

TABLE OF CONTENTS (continued)

LIST OF FIGURES

LIST OF FIGURES (continued)

LIST OF FIGURES (continued)

LIST OF TABLES

CHAPTER I

INTRODUCTION

This chapter intends to provide an overview of major fiber optic sensor technologies, as well as to clarify the context arrangement of the work.

1.1 Overview

As usually happens, technology developed with one aim sooner or later affects other adjacent areas. In early 1970s, some of the first experiments on low-loss optical fibers were not for telecommunications as had been the prime motivation for their development in 1960s, but for sensing purposes. This pioneering works quickly led to the creation of an active group of researchers who focused on the exploitation of this new technology. Meanwhile, along with the tremendous evolvement of telecommunications technologies in recent years, proficient knowledge and various techniques for optical signal generation, propagation, amplification, interrogation, processing and storage have been significantly developed, which efficiently facilitate the research progress in fiber optic sensors, so that more capable, more reliable and cheaper fiber optic sensors become practical.

The main drive of research in fiber optic sensors today has been to produce a range of optical fiber based techniques, which can be used for versatile sensing purposes, and providing an effective measurement method in key areas. Among other competitive techniques such as electrical sensors, fiber optic sensors are capturing more and more attention in the industry upon their unique advantages in the following aspects [4]:

(1) The typical dimension of most commercially available optical fibers are in the range of several hundred micrometers, thus fiber optic sensors are always featured

with small size and lightweight, which will induce minute alteration to the host ambience under test.

(2) Most optical phenomena are immune to electromagnetic interference (EMI), hence fiber optic sensors are always the most promising candidates for applications with strong electromagnetic field, such as deep artesian detection.

(3) Most fiber optic sensors are susceptive to multiple ambient variances (e.g. strain, pressure and temperature). Thereby a multifunctional sensor system can be produced, and entire testing mechanism is possibly simplified.

(4) Due to low signal attenuation and broad transparent spectrum, fiber optic sensors can be easily multiplexed, thus large scaled distributed or quasi-distributed sensor network is practicable.

1.2 Fiber Optic Sensor Technology Review

Although vast different fiber optic sensor precepts are being presented, and various criteria have been proposed to categorize, from author's point of view, the technology can be classified as following:

(1) **Interferometric Sensors**. The use of interferometers in optical measurement has been well established for decades. In general, this type of sensors are based on the mechanism in which coherent optical signals are interfered, states of resulted optical fringes are consequently varied upon ambient changes. Almost all interferometric mechanisms can be deployed to fabricate fiber optic sensors, which include Michelson, Mach-Zehnder, Fabry-Perot, Sagnac interferometers, polarization based interferometers, and other low-coherent interferometers. In broad sense, in-fiber grating sensors can also be categorized as interferometric sensors.

(2) **In-Fiber Grating Sensors**. Bragg gratings written into optical fibers, have had enormous impact on both optical communication, lasers, and fiber optic sensors since late 1980s. Gratings, acting as sensing elements, are photo-inscribed into silica fibers with excimer lasers and specially patterned masks, which possess all advantages normally attributed to fiber optic sensors. In addition, this type of sensors has inherent self-referencing capability and is easily multiplexed in a series fashion along a single fiber [5]. According to the literature, different in-fiber grating sensors have been reported, including normal fiber Bragg grating (FBG) sensors, chirped grating sensors, laser incorporated fiber grating sensors, blazed fiber grating sensors, long period fiber grating sensors, and hybrid grating sensors, etc.

(3) **Luminescent Sensors**. This fiber optic sensor category is relied on the technique that optical fibers are doped with materials in which luminescence may be generated or intensity of the fluorescence may be varied upon ambient changes. Luminescent fiber optic sensors have been widely used in chemical and biomedical applications.

(4) **Scattering Based Sensors**. In most recent researches, non-linear effects are employed in designing new generation fiber optic sensors, especially in realizing distributed sensor systems. The fundamental reason for this is that these effects exhibit varied and distinctive responses to external measurands, thus providing the development of a range of application-specified sensors. These scattering based sensors include backscattering sensors such as Raleigh scattering sensors and Raman scattering sensors, as well as forward scattering sensors such as Brillouin scattering sensors.

(5) **Other Sensors**. Besides above mentioned categories, there are some other fiber optical sensing techniques for various special applications, which include fiber optic gyroscopes (FOG), Faraday rotators, fiber laser sensors, and integrated optical MEMS (Micro-Electronic-Mechanical-System) sensors, etc.

According to the summary of digest for most recent international conference in this field [6], the 15th Optical Fiber Sensor Conference (OFS – 15: IEEE catalog number 02EX533), which was held in Portland, Oregon, USA in May, 2002, chart below illustrates a statistic distribution of all posted papers in various fiber optic sensor techniques. Upon this chart, one may find in-fiber grating sensors were acquired the most recognition among all in current researches, which shows huge potential in various application fields of this technique.

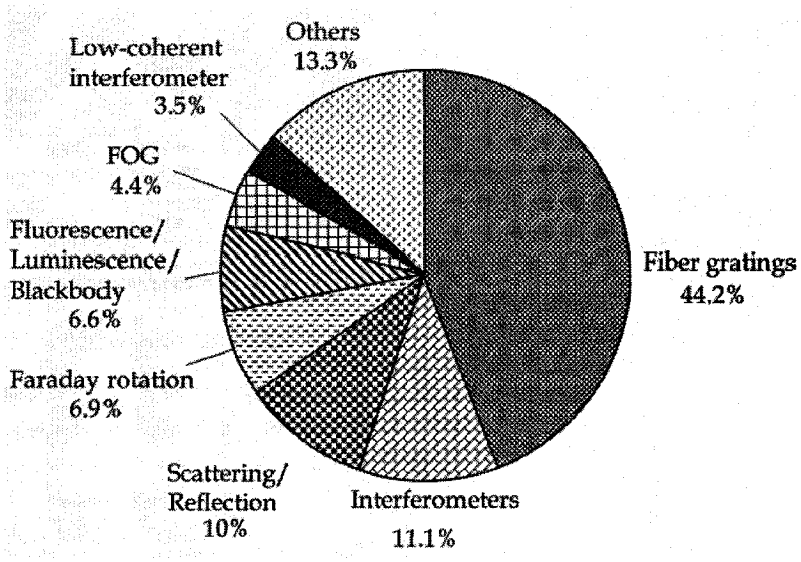

Figure 1.1 Distribution of OFS-15 Papers In Association With Various Techniques

Among the papers in this conference, almost every aspect of an entire sensing system has been involved. These research topics include: sensor integration in the host ambience, interrogations, networking methodology, applicability for various misbrands

and calibrations, etc. Chart below shows the distribution of OFS – 15 papers with subject to measurands [6]. Hence from the chart, it can be seen that strain sensors obtained the most attentions due to the fact that strain is the most prevalent measurand in engineering applications.

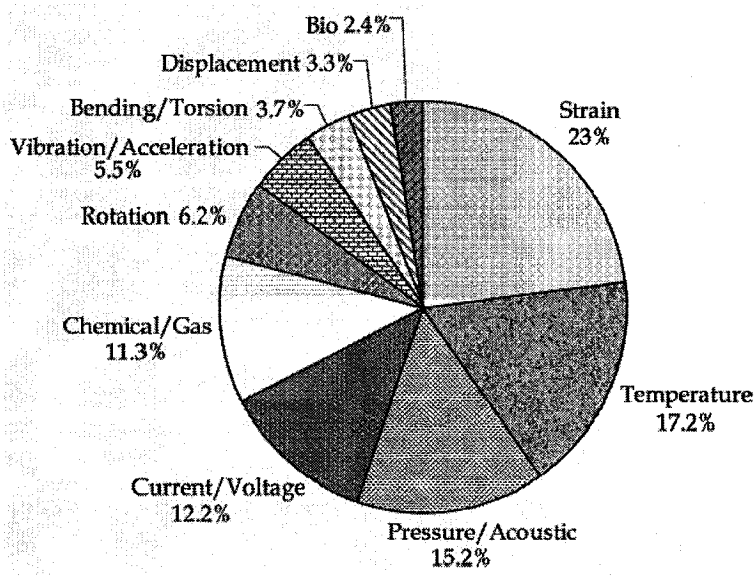

Figure 1.2 Distribution of OFS-15 Papers In Association With Various Measurands

1.3 Summary of The Work

This work reports a comprehensive investigation on an orthorgonal Fiber Bragg Grating (FBG) sensor array embedded in Graphite/Epoxy composite laminate, topics including bare FBG fibers' instinct photoelasticity, fabrication and layout optimization of FBG array embedment, recalibration of embedded FBG strain gages, applicability evaluation and synthetic performance interpretation of the gages.

In general, the report is divided into three sections: the first section includes chapter 1 and chapter 2, in which an overview of fiber optic sensor technology is made, and theoretical backgrounds are prepared for both FBG grating and composite material

techniques. Chapter 3 composes the second section of the paper, in which entire experimental progress is reported and test results are analyzed. Finally, the last section is formed with chapter 4, where conclusions are drawn, and recommendations are proposed for future experiments.

CHAPTER II

THEORETICAL BACKGROUND

This chapter introduces two major technologies that are essential in entire research work – Fiber Bragg Grating and Fiber Reinforced Composite Material. Upon the introduction, a preliminary scheme of fiber optic smart structure is prototyped, and challenges in building such a structure are emphasized.

2.1 FBG (Fiber Bragg Grating)

As mentioned in chapter 1, fiber grating sensors captured the most attention from researchers among other competitive techniques, due to their intrinsic benefits in various applications. In this work, one of the fiber grating sensors, common FBG (fiber Bragg grating) sensor, is studied, and its application to construct embedded strain gage network is investigated.

2.1.1 Basic FBG Theory

Preliminary understanding of a normal FBG grating is demonstrated in Figure 2.1. Despite the circular cross-section of an optical fiber, consider only a medium stack, in which the multiple layers are featured with interleaved refractive indices n_1 and n_2, where n_1 differs from n_2 in magnitude. A light beam possessing monochromic wavelength λ_0 perpendicularly launches into the stack. Suppose the thickness of each medium layer is controllable, one may discover once the thickness of each layer reaches $\lambda_B/4$, in which λ_B is the relative wavelength in the medium, or $\lambda_B = \frac{\lambda_0}{n_{eff}}$, n_{eff} is the average refractive index of the medium stack, then all reflected light waves from the stack interfere constructively at the interface where light is injected, so that give rise to a

substantial reflection at wavelength λ_B. If the number of layers is sufficient, and/or medium stack's refractive index modulation becomes deeper, eventual reflection will approach unity at λ_B.

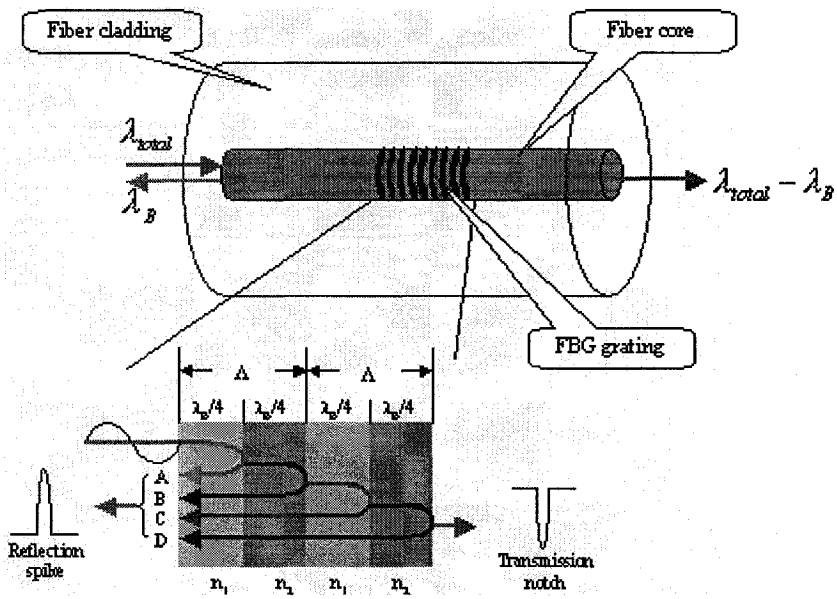

Figure 2.1 Preliminary Understanding of Fiber Bragg Grating

Subsequently if above depicted refractive index grating is constructed in the core of the optical fiber, a fiber Bragg grating (FBG) is produced. If the optical period Λ is defined as the thickness of two adjacent layers, FBG condition can then be expressed as

$$\lambda_B = 2n_{eff}\Lambda \tag{2.1}$$

Therefore, if one designates FBG grating's central wavelength λ_B at 1550nm, and assume optical fiber's average refractive index being 1.46, the grating's optical period will be approximately 530nm. Actually in most cases refractive index fluctuation of common FBG fibers is patterned as

$$n(z) = n_{eff} + \Delta n \cos\left(\frac{2\pi z}{\Lambda}\right) \tag{2.2}$$

where Δn is the amplitude of the refractive index modulation. If one launches a broadband and low coherent light into the FBG fiber, which includes wavelength component λ_B, and monitors the optical responses in wavelength domain at both ends of the fiber, reflection spike at origin side and transmission notch at end side will be observed, where both phenomena are centered λ_B . In this study, grating's central wavelength is designable by means of controlling FBG's optical period Λ, and/or the strength of refractive index.

2.1.2 FBG Inscription

Although the formation of fiber grating was first reported in 1978 [7], intensive study began on this topic after a controllable and effective method for in-fiber grating inscription was devised in 1989 [8]. In that experiment, it showed that a strong refractive index change occurred when a germanium-doped fiber was exposed to UV light close to the absorption peak of a germania-related defect at a wavelength range of 240 - 250nm. Through years of study and debate, nowadays majority accepts that Ge–Si wrong bonds are responsible for the photosensitivy of modified chemical vapor deposition (MCVD) germanosilica fiber, hence induces refractive index modulation in optical fibers. This conclusion is based on the fact that the change of refractive index in a germanosilica fiber is triggered by a single photon at 240 nm, which is well below the band gap at 146 nm, which implies that the point defects in the ideal glass tetrahedral network are responsible for this process. However, Although it appears that the Ge–Si wrong bond has a high efficiency for triggering the processes responsible for the index change in the glass, it must be made clear that Ge–Si bonds may not be the only trigger mechanism, just the most efficient found so far.

Since the discovery of photosensitivity and the first demonstration of grating formation in germanosilica fibers, there has been considerable effort in understanding and increasing the photosensitivity in optical fibers. Initially, optical fibers that were fabricated with high germanium dopant levels or under reduced oxidizing conditions were proven to be highly photosensitive. Recently, hydrogen loading (hydrogenation), flame brushing, and boron codoping have been used for enhancing the photosensitivity of germanosilica fibers. In addition to the above techniques, exposure with 193nm ArF excimer laser radiation proved to be an alternative method for inscribing strong Bragg gratings in fibers without the need of H_2 loading. This method may be thought as a photosensitive enhancement technique to the usual 240 - 250nm band irradiation for inscribing Bragg gratings in germanosilica fibers [9].

Inscribing Bragg gratings in optical fibers is a formidable task. The requirement of a submicron periodic pattern makes the stability a severe constraint on the techniques able to write Bragg gratings in optical fibers. To date, there are only a few externally written fabrication techniques, namely, interferometric technique, phase mask technique, and point-by-point technique [10]. Among the three genres, phase mask technique is most maturely evolved, which becomes widely used in the industry, and secures comparatively stable yield.

Phase mask inscription employs a diffractive optical element (phase mask) to spatially modulate the UV writing beam. Phase masks may be formed holographically or by electron-beam lithography. Holographically induced phase masks have no stitch error. However, complicated patterns can be written into the electron beams fabricated masks (quadratic chirps, Moire patterns, etc.). The phase mask grating has a one-dimension

surface-relief structure fabricated in a high-quality fused silica flat transparent to the UV writing beam. The profile of the periodic gratings is chosen such that when an UV beam is incident on the phase mask, the zero-order diffracted beam is suppressed to less than a few percent (typically, less than 5%) of the transmitted power. In addition, the diffracted plus and minus first orders are maximized, each containing, typically, more than 35% of the transmitted power. A near-field fringe pattern is produced by the interference of the plus and minus first-order diffracted beams. The period of the fringes is one-half that of the mask. The interference pattern photo-imprints a refractive index modulation in the core of a photosensitive optical fiber placed in contact with or in close proximity immediately behind the phase mask. Refer to Figure 2.2 for the schematic of the phase mask inscription technique.

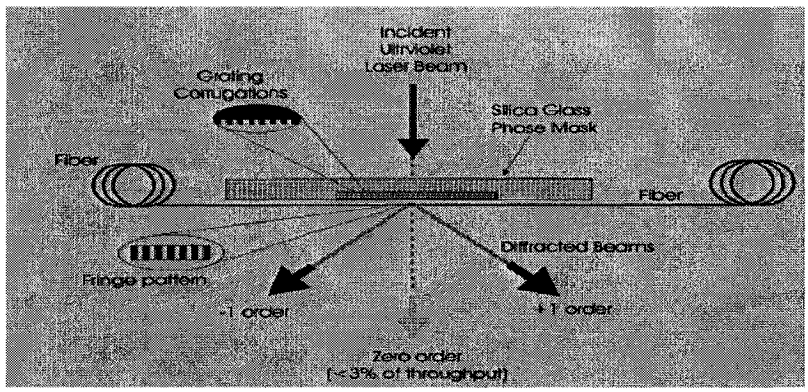

Figure 2.2 Phase Mask Inscription Technique

KrF excimer lasers are the most common UV sources used to fabricate Bragg gratings with a phase mask. A cylindrical lens may be used to focus the fringe pattern along the fiber core.

2.1.3 FBG's Sensing Nature

As depicted previously, FBG's grating central wavelength λ_B is controllable in terms of the magnitude of average refractive index n_{eff}, as well as grating's optical period Λ. However, these two factors have been proven to be ambient sensible. According to the literature, due to the photoelastic and thermal-optic natures, FBG fiber's average refractive index and optical period are alterable upon in-fiber strain and ambient temperature [11]. Hence one may easily deduce that FBG fiber's grating wavelength is tunable in terms of in-fiber strain and ambient temperature changes. In short, a strain and temperature sensor is achievable.

Assuming an isothermal condition, FBG's grating central wavelength shift upon strain and temperature changes can be expressed as [11]

$$\Delta\lambda_B = 2\left(\Lambda\frac{\partial n_{eff}}{\partial l} + n_{eff}\frac{\partial\Lambda}{\partial l}\right)\Delta l + 2\left(\Lambda\frac{\partial n_{eff}}{\partial T} + n_{eff}\frac{\partial\Lambda}{\partial T}\right)\Delta T \tag{2.3}$$

where the first term represents the strain effect on FBG fiber, this corresponds to a change in grating spacing and strain-optic induced change in average refractive index. The second term represents the thermal effect on FBG fiber, similar to that in strain component, temperature drifts also comprehensively affect grating spacing and magnitude of refractive index.

(1) Strain Sensitivity

Regarding the strain effect in equation (2.3), l is the gauge length of a FBG strain sensor. Given that the path-integrated longitudinal strain is $\varepsilon_z = \Delta l / l$, and [12]

$$\Delta\left[\frac{1}{(n_{eff})^2}\right] = -\frac{2\Delta n_{eff}}{(n_{eff})^3} \tag{2.4}$$

And assuming $\frac{\partial \Lambda}{\partial l} = \frac{\Lambda}{l}$, one can rewrite the strain term in equation (2.3) as

$$\begin{aligned} \Delta\lambda_B &= 2\left(\Lambda\frac{\partial n_{eff}}{\partial l} + n_{eff}\frac{\partial \Lambda}{\partial l}\right)\Delta l \\ &= 2\Lambda\left\{-\frac{(n_{eff})^3}{2}\Delta\left[\frac{1}{(n_{eff})^2}\right]\right\} + 2n_{eff}\varepsilon_z l\frac{\partial \Lambda}{\partial l} \end{aligned} \tag{2.5}$$

Strain-optic theory predicts that changes in the optical indicatrix tensor, $\Delta\left[\frac{1}{(n_{eff})^2}\right]_i$, is resulted from applied stress to the material, which can be given in terms of strain by

$$\Delta\left[\frac{1}{(n_{eff})^2}\right]_i = \beta_{ij}\varepsilon_j \qquad \begin{matrix} i = 2,3 \\ j = 1,2,3 \end{matrix} \tag{2.6}$$

where ε_j is the block-reduced strain tensor in the fiber, β_{ij} is the contracted strain-optic tensor of the FBG fiber with coefficient p_{ij} (Pockel's coefficient), where the subscripts i and j refer to the coordinate axis of the optical fiber, as defined in Figure 2.3.

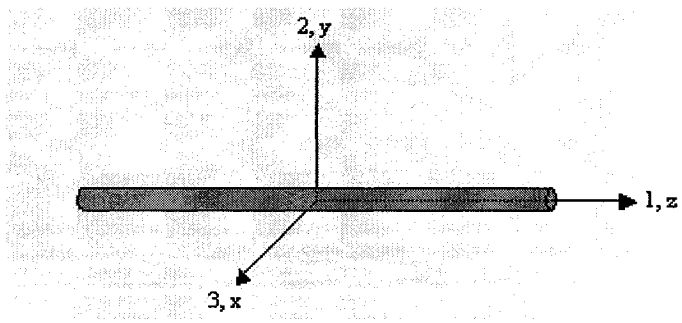

Figure 2.3 Coordinate Axes of FBG Fiber

For an optically anisotropic (i.e. birefringence) and elastically isotropic material, i.e. the optical fiber, block-reduced strain tensor ε_j can be expressed as

$$\varepsilon_j = \begin{pmatrix} \varepsilon_1 & -\varepsilon_2\mu_1 & -\varepsilon_3\mu_1 \\ -\varepsilon_1\mu_2 & \varepsilon_2 & -\varepsilon_3\mu_2 \\ -\varepsilon_1\mu_3 & -\varepsilon_2\mu_3 & \varepsilon_3 \end{pmatrix} \tag{2.7}$$

However, if we consider that only longitudinal stress is applied along fiber's axis z, where direction z coincides with direction 1 in the coordinate, and assume zero additional lateral stress (which is valid in case of bare FBG fiber), strain tensor ε_j is further reduced as

$$\varepsilon_j = \begin{pmatrix} 1 \\ -\mu_2 \\ -\mu_3 \end{pmatrix} \varepsilon_z \tag{2.8}$$

where μ_2 and μ_3 are poisson's ratios of optical fiber along two radial directions 2 and 3, respectively. In equation (2.6), the contracted orthotropic strain-optic tensor is given by

$$\beta_{ij} = \begin{pmatrix} p_{11} & p_{12} & p_{13} \\ p_{12} & p_{22} & p_{23} \\ p_{13} & p_{23} & p_{33} \end{pmatrix} \tag{2.9}$$

Then substitute the expressions of ε_j and β_{ij} into equation (2.6) and (2.5), the longitudinal strain sensitivity can thus be determined and is expressed in terms of an effective photoelastic constant p_{ei} so that

$$\left(\frac{\Delta\lambda_B}{\lambda_B}\right)_i = (1 - p_{ei})\varepsilon_z \quad i = 2,3 \tag{2.10}$$

where p_{ei} is defined as

$$p_{ei} = \frac{(n_{eff})^2}{2}[p_{1i} - \mu_i(p_{i3} + p_{2i})] \tag{2.11}$$

For a low birefringent FBG fiber, the strain-optical tensor is approximately isotropic, so that $p_{11} = p_{22} = p_{33}$, $p_{12} = p_{13} = p_{23}$, and $\mu_2 = \mu_3 = \mu$ due to optical fiber's elastically isotropic nature. In this case effective photoelastic constant p_{ei} can be degenerated, so that $p_{e2} = p_{e3}$, and equation (2.10) and (2.11) are reduced to

$$\frac{\Delta\lambda_B}{\lambda_B} = (1 - p_e)\varepsilon_z \tag{2.12}$$

and

$$p_e = \frac{n_{eff}^2}{2}[p_{12} - \mu(p_{11} + p_{12})] \tag{2.13}$$

Even though physical parameters of optical fibers from different manufacturers have tiny variation, it is reported generally for a FBG grating inscribed in typical germano-silicate optical fiber, one can obtain strain sensitivity at 1550nm wavelength range as [11] [13] [14]

$$\Delta\lambda_B \approx 1.2 \times 10^{-3}\varepsilon_z \tag{2.14}$$

where axial strain ε_z is in με, and grating wavelength shift $\Delta\lambda_B$ is in nm. Therefore, one can expect about 1.2 pm grating wavelength increase as a result of applying 1με axial strain to FBG fiber.

Nevertheless, whenever additional radial stress is applied to FBG fiber, above discussed photoelastic feature will be varied, since the strain tensor ε_j defined in equation (2.7) can no longer be simply transformed to equation (2.8). This topic will be further discussed in following chapters.

(2) Thermal Sensitivity

According to equation (2.3), the thermal effect component of a FBG grating can be transformed to

$$\Delta\lambda_B = 2\left(\Lambda\frac{\partial n_{eff}}{\partial T} + n_{eff}\frac{\partial\Lambda}{\partial T}\right)\Delta T \qquad (2.15)$$

$$= \lambda_B(\alpha+\zeta)\Delta T$$

where $\alpha = (1/\Lambda)(\partial\Lambda/\partial T)$ is the thermal expansion coefficient for the fiber (approximately 0.55×10^{-6} for silica); and quantity $\zeta = (1/n)(\partial n/\partial T)$ represents the thermo-optic coefficient in the linear domain, which approximately equals to 8.6×10^{-6} for germania-doped silica fiber. Hence the expected temperature sensitivity of a FBG fiber at 1550nm is approximately 13.7pm/°C [11].

Due to dual sensitive feature, in case FBG fiber is used as strain sensor, thermal induction must be counted and properly offset when interpret sensor's responses.

2.2 Fiber Reinforced Composite Materials

Fiber reinforced polymer matrix composite materials hitherto used predominantly from aerospace to household appliances, in widespread industrial applications. These advanced composites combine reinforcement (e.g. glass, graphite, or Kevlar fibers, etc.) with matrix (e.g. epoxy, polyimide, or bismaleimide, etc.), which present combined features of high stiffness, high strength, and low weight. These significant advantages determine fiber reinforced composite materials being the unique replacement for metals [15]. Another exclusive benefit of fiber reinforced composite materials is, they are the prime candidates to integrate fiber optic sensors.

Before any discussion, concerning materials can proceed, it is necessary to present idealized conceptual or mathematical model of the material. Further, if these models are to have value, they must be appropriate for the problem at hand. In current discussion, it is assumed that material's microstructural scale is small compared to the response-of-interest scales. So that it is precise enough to smear-out or average the microstructure and assume that the material can be represented as a "continuum".

Within the context of a continuum, there are two characteristics of importance. These describe the direction or orientation effects on material properties and the uniformity of properties from location to location in a material. With respect to orientation, there are two extremes [16]:

(1) **Isotropic Materials**: material properties are invariant with regard to orientation. Thus the properties will not change if they are measured with respect to different coordinate systems. There is infinity of material symmetry planes.

(2) **Anisotropic Materials**: These are the converse of isotropic materials; that is, the material properties are different in all directions. There are no planes of material symmetry.

In a similar manner, there are two extremes when concerning spatial uniformity:

(1) **Homogeneous Materials**: the properties are the same from location to location.

(2) **Heterogeneous Materials**: the properties vary from location to location. Any material that is not homogeneous is heterogeneous.

It is clear from definitions above that all materials are anisotropic and heterogeneous if they are examined at a fine-enough scale. Therefore this material characterization is meaningful only if adopted at a macroscopic scale within the context

of a continuum representation, thus for intended purpose material properties must be satisfactorily defined by averaged behavior of individual constituents.

2.2.1 Lamina

A layer or a ply of composite material is called "lamina". Understanding of composite lamina is the fundamental for further discussions on composite structures, and therefore a complete description is given.

A composite lamina is a thin layer of material composed of reinforcing fibers surrounded by matrix. The fibers provide strength and stiffness, and matrix binds reinforcing fibers together and provides protection from hostile environment. In this work, lamina under investigation is consisted of graphite fibers as reinforcing element and epoxy resin as surrounding matrix. The thickness of one graphite/epoxy lamina layer is about 125μm, and designed sample's in-plane size is 200mm ×40mm.

It is clear that lamina has relatively large microscale: the reinforcement diameter is relatively large compared to the thickness of laminae, and fibers are definitely not microscopic compared to lamina thickness. However for most applications, it has been found appropriate to assume that the reinforcing and matrix phases are smeared and to model a lamina as a continuum. Caution should be exercised if fracture or other small-scale phenomena are important, in these cases such an assumption may not be true. The ratio of fiber to matrix is assumed the same from location to location, therefore the lamina is taken to be homogeneous.

Lamina is the building block of the laminated composite structure. A typical lamina with unidirectional reinforcement is illustrated in Figure 2.4; a lamina for a woven fabric would have sets of fibers at right angles to each other. In this diagram, particular

attention should be paid to the coordinate system denoted by (1,2,3), which are referred to as "principle material coordinates", or as simplified, "material coordinates". For unidirectionally reinforced laminae, convention dictates that 1-axis being oriented coincidently with the fiber direction, and 2-axis being perpendicular to 1-axis in the plane of the lamina, and 3-axis being normal to 1-2 plane. The 1-2 plane lies at the geometric middle surface of the lamia. For the case of woven laminae 1- and 2- axes will be aligned with the fibers if they are orthogonal, whereas 3-axis is always normal to the lamina plane. The (x, y, z) coordinate system is termed "structural axes". Choice of structural axes orientation is arbitrary but usually results from consideration of the geometry of the specimen under study. For a rectangular plate the structural axes would be normally chosen parallel to the edges of the plate. Angle θ measures the rotation of 1-axis relative to x-axis and is defined positive in a counterclockwise direction. 3-axis and z-axis are always coincident and rotations always occur about this axis.

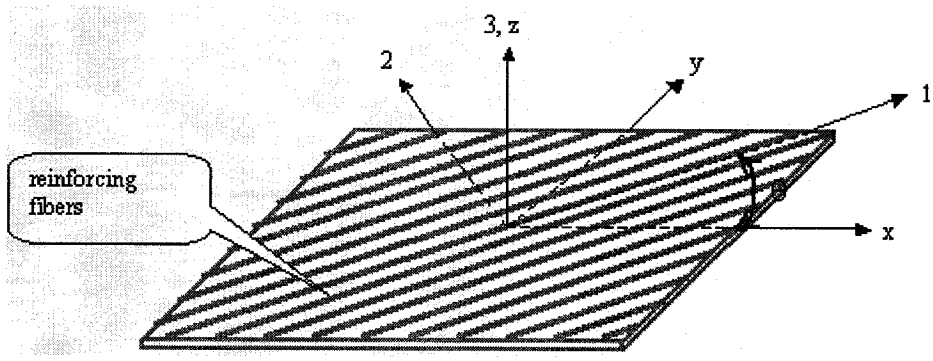

Figure 2.4 Composite Lamina Coordinates

Apparently, a fiber-reinforced composite lamina is not isotropic since the material properties are orientation dependent; the material stiffness will be different in the fiber direction (1-axis) than in the matrix direction (2-axis). It must be accepted, however, this

structure mechanically does exhibit some directional symmetry. There are three such symmetry planes: planes parallel to the 1-2, 2-3, and 1-3 planes. Material with such symmetries are said to be orthotropic.

2.2.2 Laminate

A group of laminae combined to form a structural entity is called "laminate". The objective of laminated theory is to calculate the combined structural properties; laminate properties are "average" properties of the included lamina, in which various theories have been introduced to determine the "average". One of the promising approaches can be adopted from the straightforward extension of classical plate theory for isotropic and homogeneous plates to laminated plates. The goal of this all plate theory is to reduce a three-dimensional problem to a two-dimensional problem, thereby simplifying calculations. For the case of composite plates, it results essentially in a "rule of mixtures", by which laminae properties are combined to obtain laminate properties.

A plate is a structure with two parallel surfaces or planes referred to as the faces of the plate. The plane midway between the faces is called the "middle plane" or "middle surface" of the plate. Structural coordinates (x, y, z) are adopted by way that (x, y) lying in the middle plane and z being normal to that plane. Displacements of a point (x, y, z) are denoted $\bar{u}(x, y, z)$, $\bar{v}(x, y, z)$, $\bar{w}(x, y, z)$, respectively. Furthermore, displacements of the middle plane (x,y,0) are denoted as $u(x, y)$, $v(x, y)$, and $w(x, y)$.

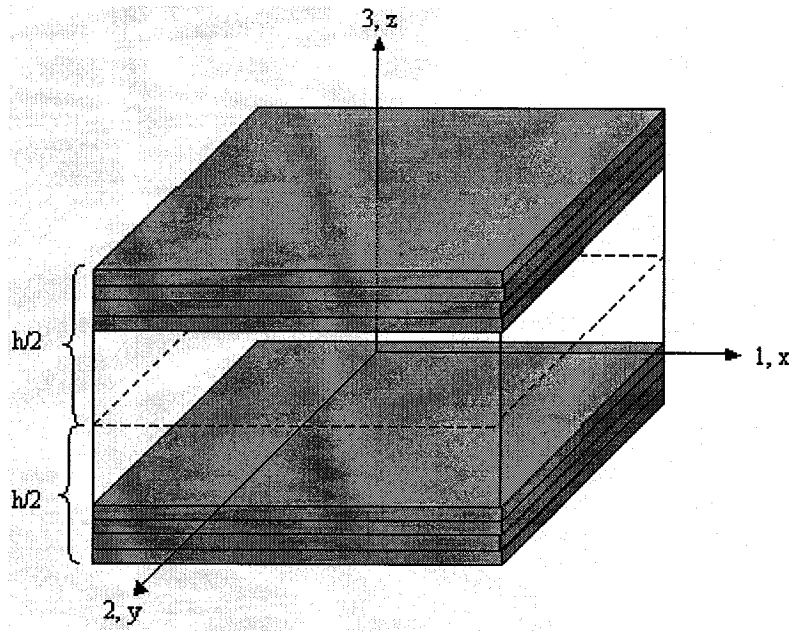

Figure 2.5 Laminate Composite

The essential assumptions of this theory include [16]:

(1) The plate is thin. That is, the thickness h is small compared to other physical dimensions.

(2) The displacements $\bar{u}, \bar{v}, \bar{w}$ are small compared to the plate thickness.

(3) The in-plane strains $\varepsilon_x, \varepsilon_y, \gamma_{xy}$ are small compared to unity.

(4) The transverse normal strain ε_z and the transverse shear strain γ_{xz}, γ_{yz} are negligible.

The development of classical plate theory stems from the foregoing assumptions. The linear strain-displacement relations are:

$$\varepsilon_x = \frac{\partial \bar{u}}{\partial x} \qquad \varepsilon_y = \frac{\partial \bar{v}}{\partial y} \qquad \varepsilon_z = \frac{\partial \bar{w}}{\partial z}$$

$$\gamma_{xy} = \frac{\partial \bar{u}}{\partial y} + \frac{\partial \bar{v}}{\partial x} \qquad \gamma_{xz} = \frac{\partial \bar{u}}{\partial z} + \frac{\partial \bar{w}}{\partial x} \qquad \gamma_{yz} = \frac{\partial \bar{v}}{\partial z} + \frac{\partial \bar{w}}{\partial y} \tag{2.16}$$

where ε_x, ε_y, and ε_z are laminate's strain components along three structural axes x, y, and z, respectively; while γ_{xy}, γ_{xz}, and γ_{yz} are corresponding engineering shear strains with subject to individual's subscript denote. Equation (2.16) combined with assumption (4) implies that

$$\varepsilon_z = \frac{\partial \bar{w}}{\partial z} = 0 \tag{2.17}$$

From which it follows that $\bar{w}(x,y,z)$ is independent of z, therefore $\bar{w}$ is equivalent to middle-surface displacement, or

$$\bar{w}(x,y,z) = \bar{w}(x,y,0) = w(x,y) \tag{2.18}$$

Assumption (4) also implies that

$$\gamma_{xz} = \frac{\partial \bar{u}}{\partial z} + \frac{\partial \bar{w}}{\partial x} = 0 \tag{2.19}$$

Noting $\bar{w} = w$, and rearranging yields

$$\frac{\partial \bar{u}}{\partial z} = -\frac{\partial w}{\partial x} \tag{2.20}$$

Since w is independent of z, both sides of equation (2.20) can be integrated with respect to z to yield

$$\bar{u}(x,y,z) = g(x,y) - z\frac{\partial w}{\partial x} \tag{2.21}$$

where $g(x,y)$ is a factor of integration that is independent of z. If $z = 0$ is substituted in to equation (2.21), it may be seen that $g(x,y) = u(x,y)$, which then gives

$$\bar{u}(x,y,z) = u(x,y) - z\frac{\partial w}{\partial x} \tag{2.22}$$

Therefore in a similar manner, one can deduct

$$\bar{v}(x,y,z) = v(x,y) - z\frac{\partial w}{\partial y} \tag{2.23}$$

Using above results, it is now possible to write the strain -displacement relations in terms of the middle – surface displacements. That is

$$\varepsilon_x = \frac{\partial u}{\partial x} - z\frac{\partial^2 w}{\partial x^2}$$

$$\varepsilon_y = \frac{\partial v}{\partial y} - z\frac{\partial^2 w}{\partial y^2} \tag{2.24}$$

$$\gamma_{xy} = \frac{\partial u}{\partial y} + \frac{\partial v}{\partial x} - 2z\frac{\partial^2 w}{\partial x \partial y}$$

which may be expressed as

$$\varepsilon_x = \varepsilon_x^0 + z\kappa_x$$

$$\varepsilon_y = \varepsilon_y^0 + z\kappa_y \tag{2.25}$$

$$\gamma_{xy} = \gamma_{xy}^0 + z\kappa_{xy}$$

where $\varepsilon_x^0, \varepsilon_y^0$, and γ_{xy}^0 are referred to as middle – surface strains, and κ_x, κ_y, and κ_{xy} as the middle – surface curvatures. Up to now, the three dimensional issue of composite laminates is concisely generalized into investigate only the middle surface of the laminate, which will be conditionally sufficient to characterize a mechanical response of the structure upon extended plate theory. Consequently, certain sensor networking topology integrated in the middle surface can factually quantify structural responses.

Particular precaution must be paid in the fact that, "principle" and "structural" coordinate systems utilized in laminate introduction do not coincide those employed in the rest of the work. Coordinate systems used in this section comply with conventional

notations in composite community, while the other coordinate system facilitates the study on cylindrical optical fiber.

Although FBG grating features photoelasticity to all dimensions, in order to simplify the discussion, it is approximated that the curvature of laminate specimens under study always remains unchanged in all evaluated ranges.

2.3 Fiber Optic Smart Structure

The revolutions in fiber optic telecommunications and optoelectronic industries have enabled the evolvement of fiber optic sensors, which offer a series of advantages over conventional electrical sensors. This evolvement, in association with the advances in composite material technology, has opened a new field of fiber optic smart structures, which offers mechanical and structural engineers the possibility of incorporating fiber optic nervous mechanisms into their designs. Implementation of this objective requires a nervous system capable of sensing changes in the structure while being part of the structure itself.

Basic functionalities of such a system are [17]:

(1) Sense environmental conditions in or around the structure;

(2) Convey information back to an optical and/or electronic signal processor;

(3) Perform an action as a result of the information sensed.

According to above highlighted tasks, modeling of a practical fiber optic smart structure based on two elite techniques - FBG sensor and fiber reinforced composite, is illustrated in Figure 2.6.

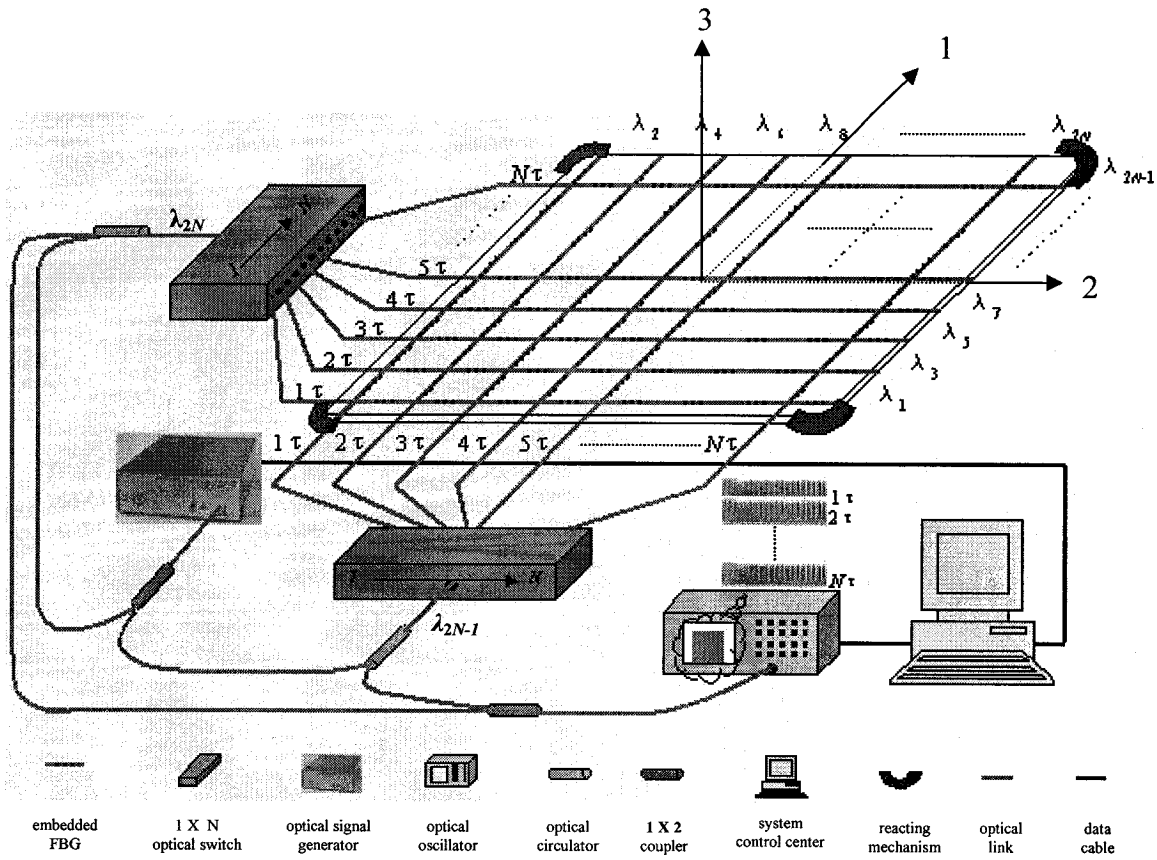

Figure 2.6 Schematic of A Practical Fiber Optic Smart Structure

Due to the orthotropic nature of fiber reinforced composites, FBG fiber network are woven longitudinally and latitudinally in the material (i.e. along 1 – and 2- directions), so that any randomly orientated in-plane strain can be analytically dissolved to two principle directions, consequently monitored and quantified by FBG sensors. FBG gratings are inscribed in series along every deployed optical fiber, among which each grating is assigned with its specific central wavelength. Or in other words, batch of grating wavelengths are preliminarily defined and designated to corresponding gratings in the array during FBG manufacturing. Different schemes may be applied in grating wavelength designation. However, upon the scheme, odd numbered central wavelengths are dispensed to FBG fibers along 1 – direction, while even numbered central

wavelengths are dispensed to those along 2 – direction. Hence a $N \times N$ quasi-distributed sensing network is built.

Two ways can be used to integrate sensing network with the structure under investigation: surface mount and embedment. For most cases, sensors embedded in the host material can be better protected from external attack thus their lifetime is secured; but surface mount may avoid sensors' sensitivity from host's internal stress disturbance, if this stress is not the desired measurand.

According to the scheme, broadband light is generated from an optical signal generator and split by a 1×2 50/50 optical coupler, so that two light branches are equally launched into two groups of FBG fibers (i.e. longitudinal deployed and latitudinal deployed fibers) at two adjacent edges of the composite structure, respectively. An $1 \times N$ optical switch is added before each fiber group to interrogate every FBG fiber in turn arrayed in one of the two principle directions.

In order to reduce the complexity of optical path and instruments involved, reflections from grating arrays are monitored at the same end of optical fibers where light is injected, therefore a three port optical circulator is inserted between 1×2 coupler and each of the $1 \times N$ switch, so that input and reflected output signals are bifurcated.

All FBG reflections finally converge in an optical oscillator from the two orthogonal groups via a reversed 1×2 coupler. In order to facilitate the identification of individual FBG tip in entire network, besides WDM (wavelength division multiplex) mechanism among the gratings along a specific FBG fiber and odd/even grating wavelength numbering between two fiber groups along orthogonal orientations, TDM (time division multiplex) mechanism is also utilized to address individual FBG fiber. In a

certain orientation group, if one defines $1 \times N$ optical switch remaining connection with individual FBG fiber for steady time τ, which should satisfy optical signal to perform at least one turnaround trip from the switch to the farthest grating in the series and then the last grating reflection coming back to the switch. Therefore optical switch spends $N\tau$ to implement a scan for N parallel arrayed FBG fibers in the group, and each FBG fiber is allotted a dedicated time slot to be interrogated, hence all gratings in the group are addressed with no coincidence. Upon the prototype, FBG reflection series from *Nth* fiber (i.e. *Nth* longitude or latitude) in the parallel array are interrogated in time slot from $(N-1)\tau$ to $N\tau$. With proper optical switch and route arrangement, FBG reflection series on both *Nth* fibers in longitudinal and latitudinal groups reach optical detector simultaneously, or the odd/even grating wavelength sequence is recovered in time slot from $(N-1)\tau$ to $N\tau$. Refer to Figure 2.7, one may get better understanding on TDM/WDM allotment of the sensor network.

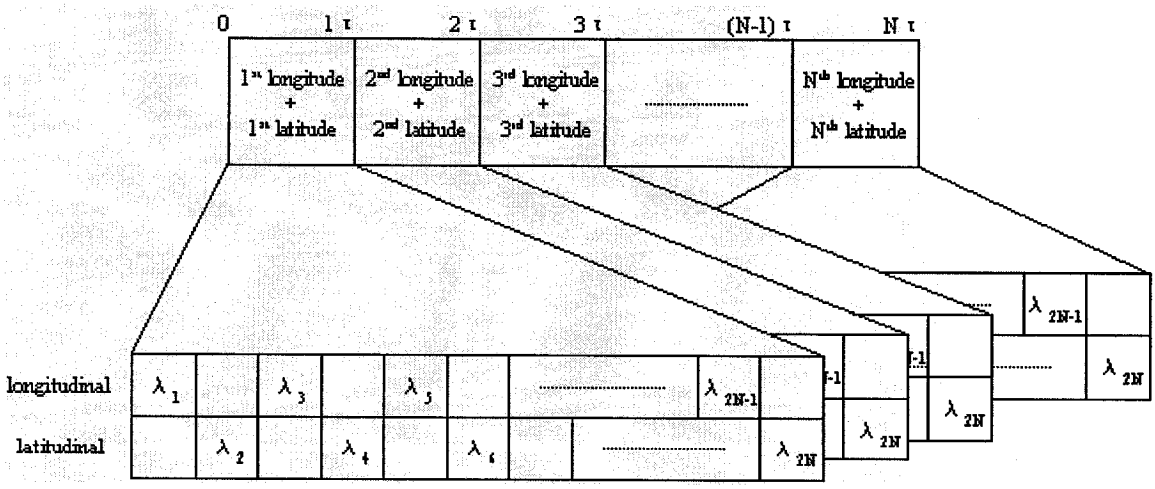

Figure 2.7 TDM Arrangement of Sensor Network

Scan rate τ of the optical oscillator secures synchronization so that one scan corresponds to one time slot of sensor network's TDM mechanism, thus the responses of sensor tip series on dedicated FBG fiber. Inductively N scans of the oscillator carry out a monitoring across $N \times N$ area of the composite structure.

Scan results are conveyed from optical oscillator to system control center for further analysis. Actuation commands are consequently generated upon abnormal responses from sensor network. Electrical commands are transmitted from control center to optical signal generator, to be modulated as optical signal, and sent together with broadband sensing signals. Far ends of some distributed FBG fibers are linked to specific reaction mechanisms. Whenever the mechanisms receive optical actuation commands, corresponding reactions are fulfilled to make the structure adapt ambient changes.

Although a primary fiber optic smart structure based on FBG sensor and fiber reinforced composite technologies is modeled, and all components involved are commercially available, crucial concerns still need to be determined before a practical system is designed and fabricated, some of them include:

(1) Sensitivity and measurement range of FBG sensors;

(2) Survivability of FBG fiber network in both composite structure fabrication and application;

(3) Alterability of FBG sensor's performance after integration in the structure;

(4) Interrogation technique to be applied, so that either dynamic or static ambient changes are precisely indicated.

No matter how complicated topology the sensor network is, complete study on a unit cell of the entire network (i.e. two orthogonally adjacent FBG sensors integrated in the structure) is the starting point to extend the discussion in larger scales.

CHAPTER III

EXPERIMENT

Nowadays, demand of higher-performance and more sophisticated composite materials rapidly grows in the industry, which greatly accelerates researches on smart structures. Hence it becomes essential to find more reliable and integratable sensors. FBG sensors offer the utmost to satisfy these requests. However, there are still challenges that remain unsolved in all aspects.

The principle a FBG fiber can be used as an embedded strain gauge is based on the presumptions that embedded fiber's axial strain equals to that of the host along with the same direction; and the effect of external radial stress applied to the optical fiber is negligible [18]. Then the grating wavelength shift will properly reflect the strain in host along with the sensor.

However, the actually situation is that, whenever embedded in the material, optical fiber is regarded as foreign entity to the host structure, which always alters the stress field in optical fiber [19]. Several Researches have proven from mechanical point of view, the inclusion dose cause local structural discontinuity hence stress field perturbation [20][21][22]. As a result, transversely FBG fiber has to bear extra stress caused by structural perturbation, which is initially not supposed to be counted in the measurement. Once FBG sensors are used as embedded strain gages, these additional effects can be regarded as noises additive to the desired measurand, so that interpretation of sensing responses may be disturbed. Thus the following two concerns need to be resolved when considering embedded FBG strain gage's applicability:

(1) Whether embedded sensors can always survive throughout the desired measurement range, when the sensors experience more complicated stress field?

(2) Whether the transverse effects induced deterioration is truly negligible?

This chapter reports the entire experiment on an orthogonal FBG sensor array embedded in Graphite/Epoxy composite laminate. Whereafter, experimental results are reviewed and analyzed. Through the discussion, above questions can be solved, and the feasibility of proposed "fiber optic smart structure" is determined.

The experiment was performed in three successive steps:

(1) **Photoelasticity of Bare FBG Fiber**. Through this step, bare FBG grating's photoelastic behavior can be characterized, which is regarded as the fundamental to determine FBG sensor's applicable range, as well as to evaluate the erroneous deviation after embedment.

(2) **Fabrication of FBG Array Embedded Composite Structure**. During this step, sensor array layout was optimized, so that the integration would induce minimum perturbation to both the host and sensors. Afterward, Graphite/Epoxy laminate specimens were designed and fabricated, in which FBG arrays were embedded subject to the optimal layout pattern. Further, gratings' optical characteristic variations due to fabrication induced residual effects were observed and analyzed.

(3) **Investigation and Calibration of Embedded FBG Strain Gage Array**. In this step, tensile loads were applied to specimens, simultaneously optical responses of embedded sensors were monitored. Referring to geometrically coincident resistance strain gage arrays, FBG strain gages are calibrated, and their erroneous deviations are quantified.

In order to maintain experimental consistency, as well as to facilitate further discussion upon test data, all bare optical fibers involved in grating production were Corning® SMF-28™ fiber, therefore all optical fiber parameters quoted in this work come from Corning published specification [23]. As well, all FBG gratings employed in the experiment were inscribed at Bragg Photonics Inc.

3.1 Step 1

Photoelasticity of Bare FBG Fiber

Although theoretical photoelasticity of FBG grating has been depicted in last chapter, practical behaviors may vary among different manufactures. In order to obtain precise fundamental for further discussion, characterization on certain bare FBG fibers becomes necessary. Meanwhile, FBG fiber's tensile strength also needs to be verified, so that sensor's measurable extreme is counted.

3.1.1 Experiment Design

(1) Mechanical Prediction

According to Hooke's law, for a glass fiber (i.e. linearly elastic material):

$$S = E \cdot \varepsilon \tag{3.1}$$

where S is the axial stress (tension or compression), $\varepsilon = \Delta l / l$ is the longitudinal deformation (elongation or curtailment), and E is the elastic modulus. Since the elastic modulus for core and cladding sectors of an optical fiber is 72900 N/mm^2, with force-bearing cross sectional areas of 0.0123mm^2 [24] [25]:

(1) A strain of 2000με (i.e. 0.2%) requires tensile load of 1.79 N (183 g), which causes a piece of 500mm optical fiber to be extended with 1mm;

(2) While a strain of 5000με (i.e. 0.5%) requires tensile load of 4.48N (458g), which causes a piece of 500mm optical fiber to be extended with 2.5mm.

Moreover, according to manufacturer's specification, tensile strength of the FBG fiber is greater than 100kpsi [26]. Upon

$$F_t = S_t \times A \tag{3.2}$$

where S_t is the specified tensile strength of FBG fiber, which is greater than 689.49N/mm^2 (1kpsi $\simeq$ 6.8948N/mm^2); A is the cross sectional area of the fiber, which is approximately 0.0123mm^2; and F_t is the load along fiber when it reaches mechanical maximum. Therefore when tensile strength is reached, the tensile load applied will be greater than 8.48N (or 865g), which causes approximately 9458με, or 0.95% strain of the FBG fiber. This characteristic is crucial to be verified since the outcome determines FBG gauge's applicable range, as well as to gain knowledge on FBG fiber's behavior at extreme point.

(2) Photoelastic Prediction

According to the discussion in last chapter, theoretically FBG's strain sensitivity at 1550nm is about 1.2pm grating wavelength increase as a result of applying 1με axial strain (which is equivalent to 8.97×10^{-4} N or 9.15×10^{-2} g tensile load) to the fiber. Therefore FBG sensor's strain response follows as:

$$\Delta\lambda_B = 1.2\times10^{-3}\varepsilon_z \tag{3.3}$$

where ε_z is FBG fiber's axial strain in με, $\Delta\lambda_B$ is grating's central wavelength shift in nm. If relating the central wavelength shift with load instead of strain, equation (3.3) can be transformed to:

$$\Delta\lambda_B = 1.31\times10^{-2} F_z \tag{3.4}$$

where F_z is the applied tensile load in gram. Therefore in case the temperature effect is hypothetically excluded, one can expect:

(1) Approximately 2.4nm grating wavelength shift with an axial strain of 2000με, if 1.79N (183g) tensile load is applied on the FBG fiber;

(2) Approximately 6.0nm grating wavelength shift with an axial strain of 5000με, if 4.48N (458g) tensile load is applied on the FBG fiber;

(3) Approximately 11.3nm grating wavelength shift when FBG fiber reaches its presumed minimum tensile strength, i.e.100kpsi or 9458με.

(3) Measurement Arrangement

The measurements on bare FBG fiber were performed in steps as below:

(1) Strain reached 2000με (0.2%) with load up to 185g (1.81N);

(2) Strain reached 5000με (0.5%) with load up to 485g (4.75N);

(3) Strain reached mechanical failure (tensile strength).

Throughout the three phases, FBG fiber's grating wavelength shift was observed, and its axial elongation was recorded. Eventually the test results were compared with theoretical expectation, measurement uncertainty is discussed, and conclusion is drawn accordingly.

During the experiment, mechanical contribution of optical fiber's coating was neglected since the core and cladding sector (the inner 125μm diameter area) bears more than 98% of the entire load, due to the low elastic modulus of the coating materials [23][24].

(4) Regression Analysis

According to above discussion, a linear relationship between FBG fiber's axial strain and its grating wavelength shift is expected, i.e.

$$\lambda_B = a \cdot \varepsilon_z + \lambda_0 \tag{3.5}$$

where a mathematically expresses the slope of the linear curve, or physically defines FBG sensor's axial strain sensitivity. After a set of test data is collected, linear least-square statistics is deployed to explore the experimental value of a, and then to compare with the theory.

Upon engineering statistics [27], to calculate slope and intercept of a linear function $y = a \cdot x + b$, following approximations can be used:

$$a = \frac{N\sum_{i=1}^{N} x_i y_i - (\sum_{i=1}^{N} x_i)(\sum_{i=1}^{N} y_i)}{N\sum_{i=1}^{N} x_i^2 - (\sum_{i=1}^{N} x_i)^2} \tag{3.6}$$

$$b = \frac{\sum_{i=1}^{N} y_i - a\sum_{i=1}^{N} x_i}{N} \tag{3.7}$$

In our discussion, since FBG's initial grating wavelength is dedicated (i.e. λ_0 when strain is zero), this means no matter how the test result is scattered, final regressed curve has to be obliged to pass through the initial point, or in another word, the curve's intercept is certain. Therefore $b = \lambda_0$, hence the question is simplified to find only the slope a, which can be obtained from the following equation [28]:

$$a = \frac{\sum_{i=2}^{N} \varepsilon_{zi} \Delta\lambda_i}{\sum_{i=2}^{N} \varepsilon_{zi}^2} \tag{3.8}$$

where ε_{zi} is the axial strain in με at each step, $\Delta\lambda_i$ is the corresponding grating wavelength shift in nm.

(5) The Setup

The experiment was performed on a piece of 500mm bare optical fiber with 25mm stripped section in the middle, in which 14mm was written with Bragg grating. The stripped section was not recoated after FBG inscription. Optical fiber's top end was mounted on a material structural test frame with glue, and the fiber's bottom end was glued through a load supporting plate, which was also used to drive a displacement transducer, so that optical fiber's elongation was read out. The standard weights (10g of each) were put on the load supporting plate, which caused weighable load to the optical fiber under test.

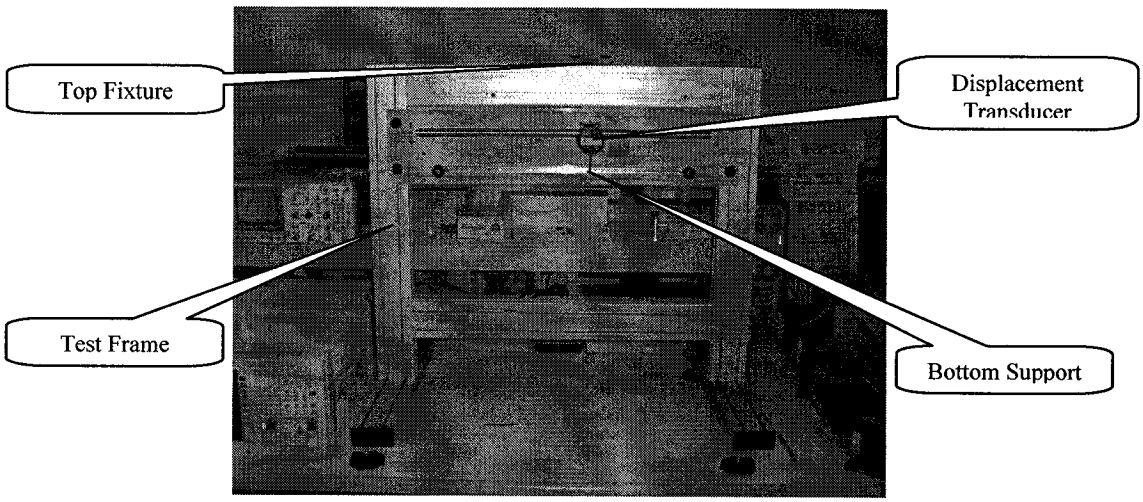

Figure 3.1 Material Structural Test Bed

There are two ways to read FBG's grating wavelength behavior with broadband LED source and OSA (Optical Spectrum Analyzer) in hand:

(1) Transmission notch readout. Refer to Figure 3.2 (a), one end of the optical fiber links to the light source, the other end of the optical fiber connects to OSA, so that the transmission spectrum is shown on OSA (e.g.. Figure 3.3 (a)).

(2) Reflection spike readout. Refer to Figure 3.2 (b), a three-port optical circulator is deployed in the setup. Port 2 of the circulator connects the FBG fiber, while port 1 and port 3 connect to light source and OSA, respectively. Hence FBG's reflection spectrum is displayed on OSA (e.g. Figure 3.3 (b)).

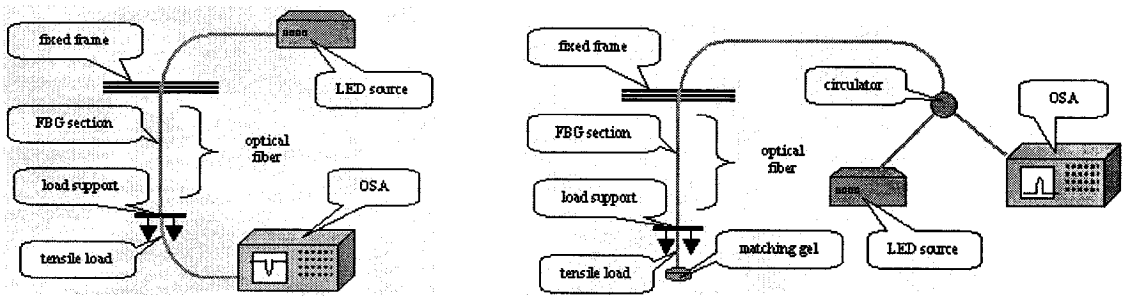

(a) Transmission Notch (b) Reflection Spike

Figure 3.2 Schematic of Test Setups for Experiment Step 1

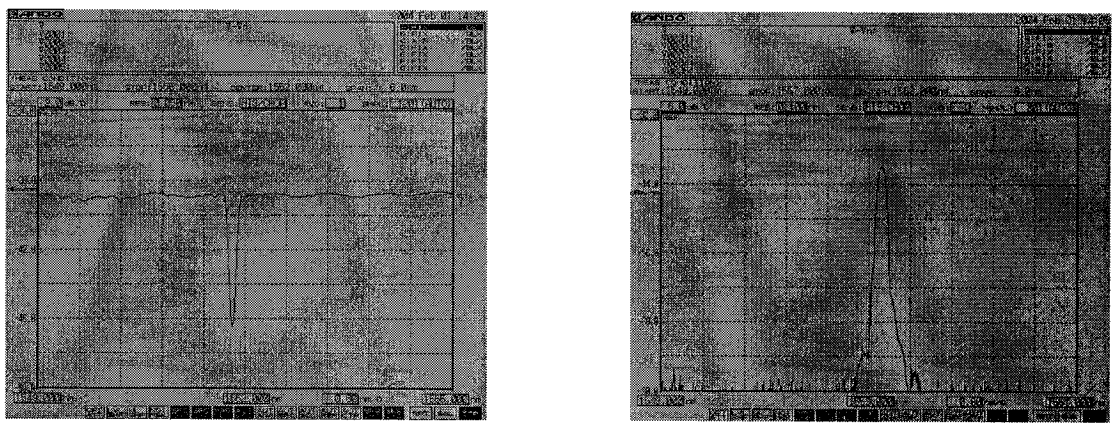

(a) Transmission Notch (b) Reflection Spike

Figure 3.3 Result Samples of Two Optical Schemes

(6) Material List

Below is the list of facilities used in the measurement.

	OSA	light source	weighbridge	structural test frame	displacement transducer
Model Number	AQ6319	AQ6319	Mettler II	STR1	ID-S1012M
Serial Number	20382604	20362804	625280	V3512/35	15570
Manufacturer	Ando	Ando	Mettler Instrument AG	TQ Education &Training Ltd.	Mitutoyo Corp.
Resolution	0.01 ~ 0.5nm	< −10dBm	0.01mg		0.01mm
Sensitivity	< ±10pm (1520~1580nm)		< 0.005g		< 0.005mm

	thermometer	ruler	weight	glue	hardener	optical circulator
Model Number	HH11	STR4		LePage12 resin epoxy	LePage12 hardener	PICT-1550-S
Serial Number		V5433/8		3EC1114D	3EC1114D	00TE0259
Manufacturer	OMEGA Engineering Inc.	TQ Education &Training Ltd.	Minarik Corp.	Henkel	Henkel	Oyokoden Lab Co. Ltd.
Resolution	0.1°C	1mm	10g			
Sensitivity	0.1°C	0.5mm	1g			

Table 3.1 Facilities Used in Experiment Step 1

3.1.2 The Results

a. 2000με (0.2% Elongation)

According to Hooke's law in equation (3.1), axially 2000με (i.e. 0.2% elongation) requires 1.79 N (183 g) load, which causes a piece of 500mm optical fiber to be extended with 1mm. Meanwhile, upon equations (3.3) and (3.4), one can expect 2.4nm grating wavelength shift, in case the temperature effect is hypothetically excluded.

In the experiment, load incremental step from 0 g to 185g is 20g, therefore 10 values were collected for a regular increase, and 19 values for a turn-around progress. In this measurement, the 1st optical scheme was deployed (refer to Figure 3.2 (a)).

(1) Mechanical Behavior

Upon experimental results, elastic modulus of the FBG fiber under investigation is

$$E = \frac{\sum_{i=2}^{N} \varepsilon_{zi} S_i}{\sum_{i=2}^{N} \varepsilon_{zi}^2} = 73900 N / mm^2 \tag{3.9}$$

From Figure 3.4, it can be seen that the experimental results fairly match the theoretical expectations. The small deviation is resulted from:

(1) Optical fiber' coating shares a small part of the load, which equivalently enlarges optical fiber's effective force-bearing cross sectional area;

(2) Uncertainty of displacement transducer's reading;

(3) Deviation of the standard weights.

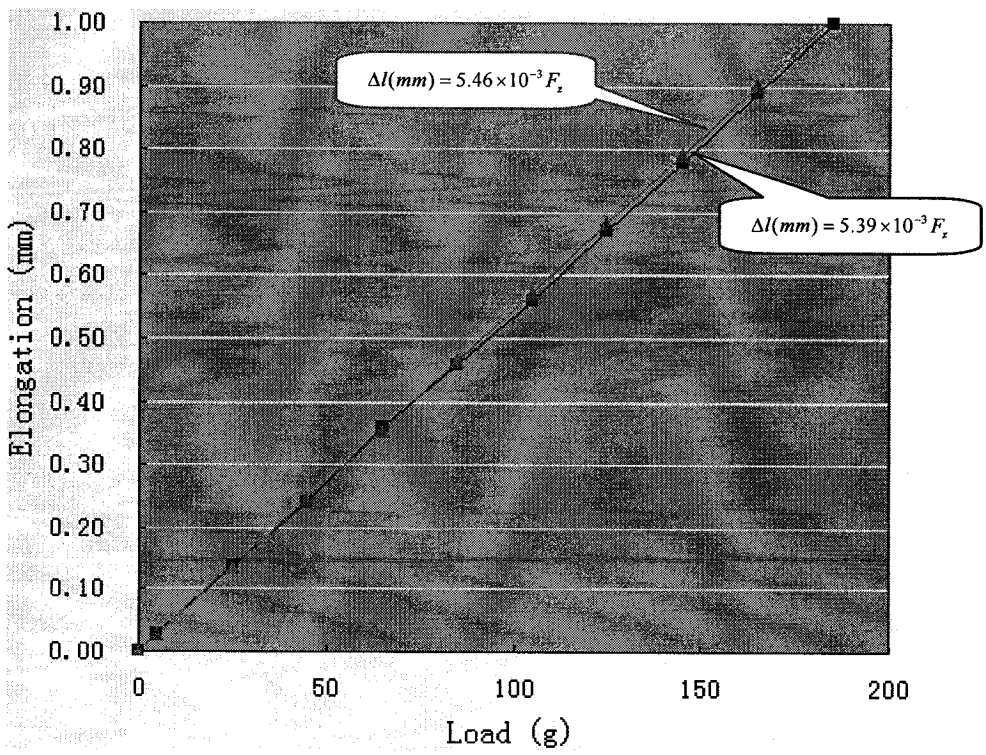

(a) Load - Elongation

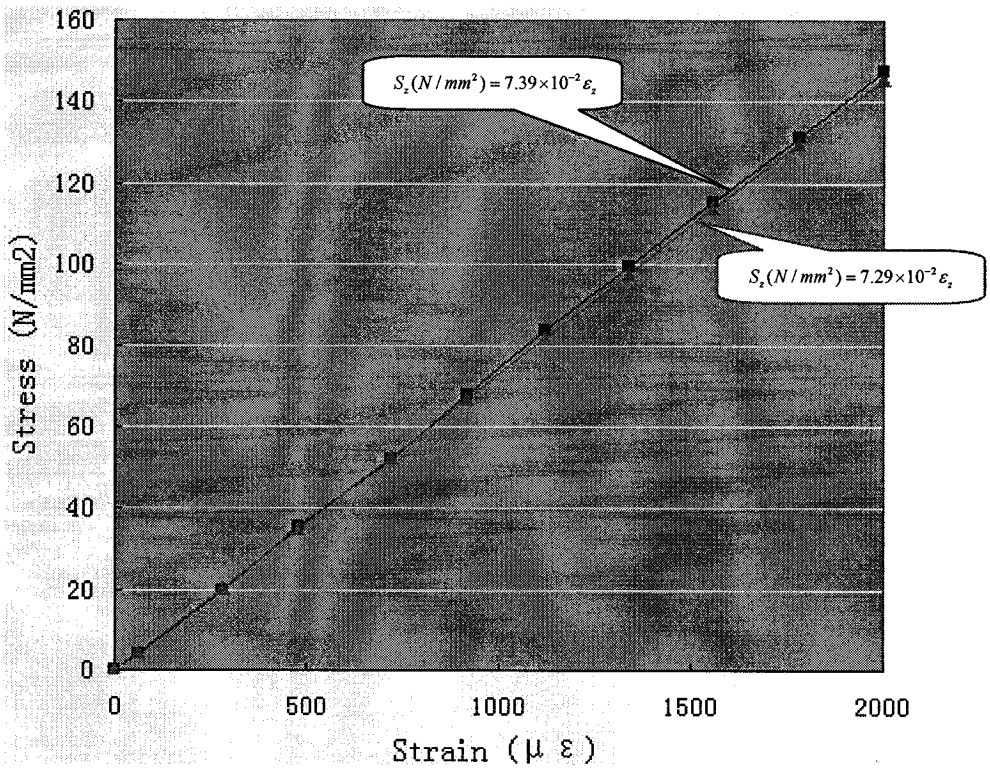

Figure 3.4 Bare FBG Fiber' s Mechanical Behavior For 2000μ ε Measurement

(2) Photoelastic Behavior

According to the experiment, FBG grating's regressed strain sensitivity is 1.22pm/με. From Figure 3.5, it shows the experimental results fairly match the theoretical expectation. Potential errors are mainly caused by:

(1) Temperature fluctuation during the measurement (between 21.0°C to 21.5°C);

(2) OSA's uncertainty;

(3) Optical fiber' coating shares a small part of the load;

(4) Error induced in optical fiber length measurement;

(5) Displacement transducer's uncertainty;

(6) Deviation of the standard weights;

(7) Deviation of grating's strain sensitivity at different wavelengths.

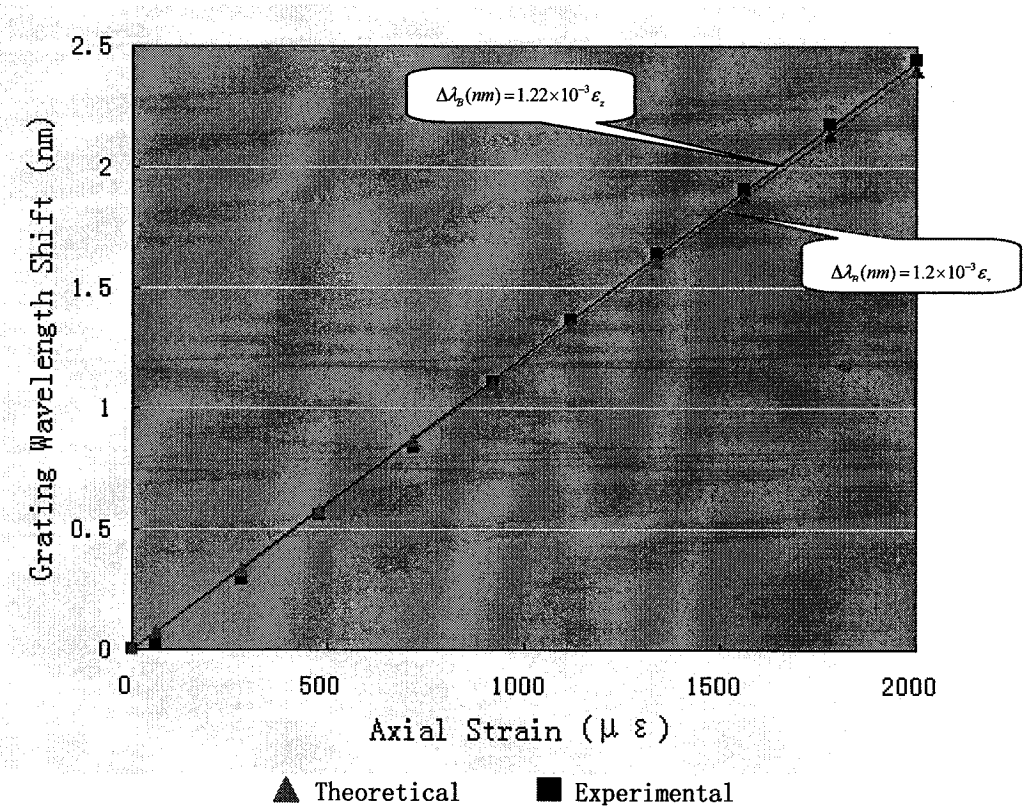

Figure 3.5 Bare FBG Grating' s Photoelastic Behavior For 2000μ ε Measurement

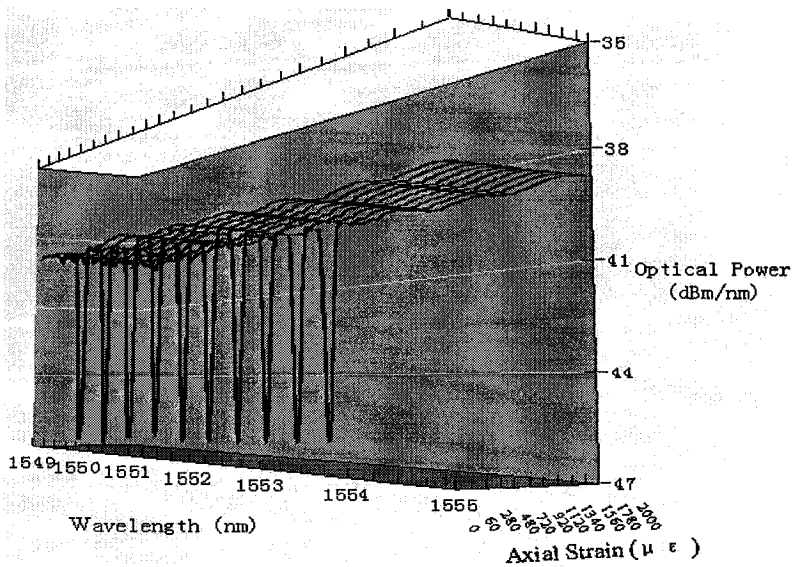

Figure 3.6 Transmission Notch Evolvement

b. 5000με (0.5% Elongation)

According to Hooke's law in equation (3.1), axially 5000με (i.e. 0.5% elongation) requires 4.48 N (458 g) load, which causes a piece of 500mm optical fiber to extend 2.5mm. Meanwhile, according to equations (3.3) and (3.4), one can expect 6.0nm grating wavelength shift, in case the temperature effect is neglected.

In the experiment, load incremental step from 0 g to 485g was 40g, therefore 13 values for a regular increase were collected, and 25 values for a turn-around progress. In this measurement, the 2nd optical scheme was utilized (refer to Figure 3.2 (b)).

(1) Mechanical Behavior

In the measurement of 5000με, since the bottom load supporting plate was not stable enough to precisely drive the displacement transducer after load exceeding 300g, hence optical fiber's elongation values were not recorded. It is supposed that the FBG fiber's mechanical performance followed the same linear elastic progress as what have been obtained in 2000με measurement (i.e. 73900N/mm^2 elastic modulus), and corresponding strain values were calculated accordingly.

(2) Photoelastic Behavior

According to the experiment, FBG grating's regressed strain sensitivity is 1.24pm/με Figure 3.7 shows the experimental results fairly matching the theoretical expectation. Causes of potential errors in 5000με measurement are same as in 2000με measurement

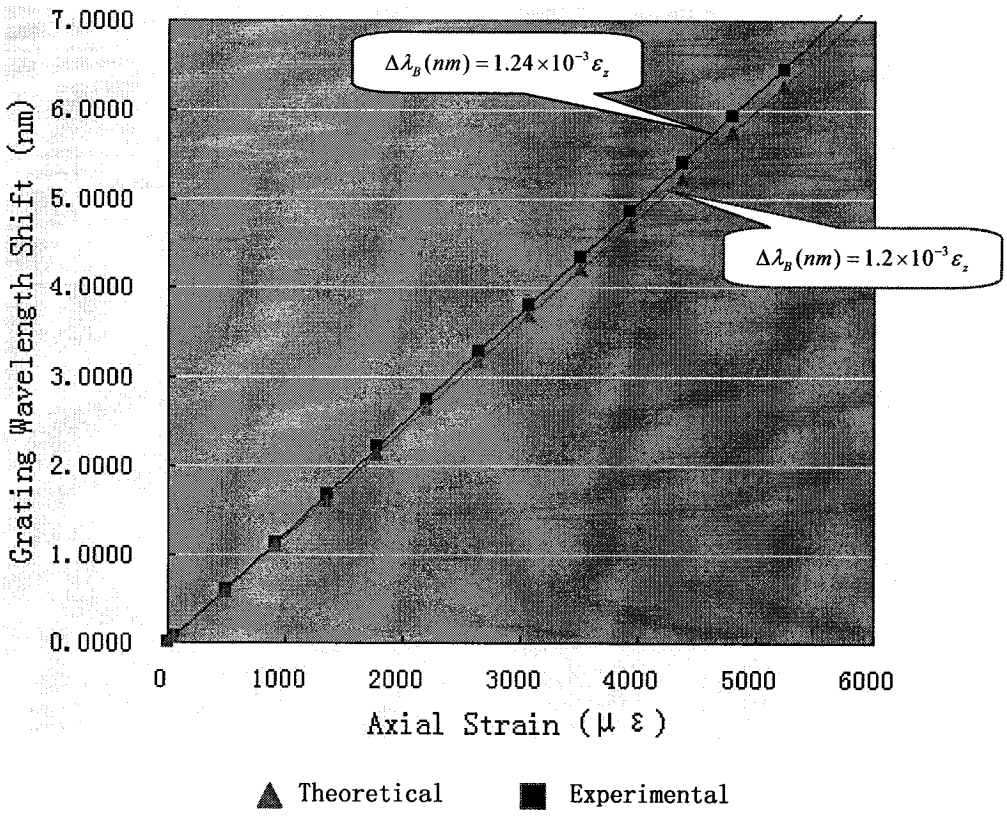

Figure 3.7 Bare FBG Grating' s Photoelastic Behavior For 5000μ ε Measurement

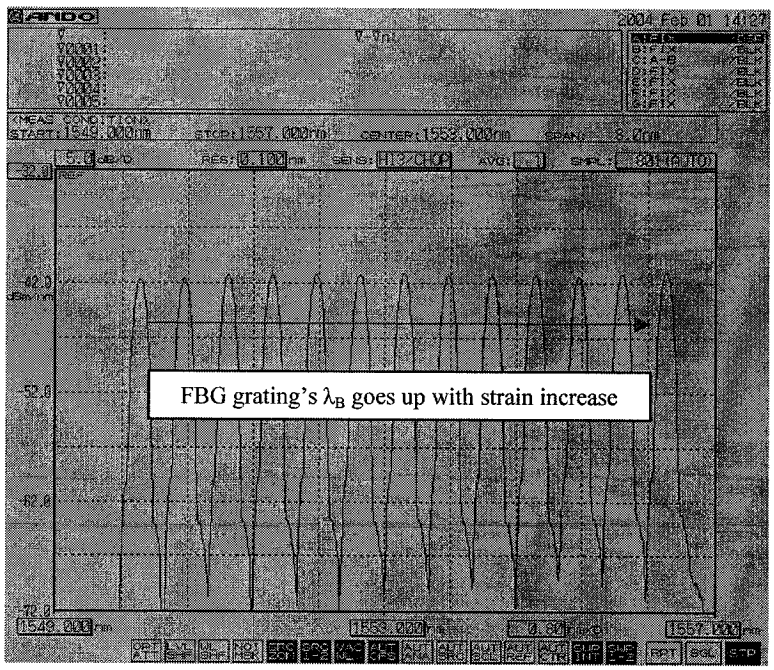

Figure 3.8 Reflection Spike Evolvement

c. Tensile Strength (Mechanical Failure)

Based on equation (3.2), when optical fiber reaches its tensile strength, minimum axial load required is approximately 8.48N (865g), which equals to 9458με, or 0.95% elongation of the fiber.

According to the reference [11], even though significant variation exists, statistically an UV-irradiated optical fiber becomes mechanically weaker, because external (surface) and internal (on molecular scale) defects are induced in grating inscription process. However, it has been proven difficult to arrive at conclusive data for measuring the mechanical degradation of UV-exposed optical fibers (i.e. FBG fiber in comparison with normal optical fiber in our consideration). Hereby in the experiment, loading progress was divided into two phases:

(1) Added load to 485g (4.75N), i.e. about 5000με;

(2) From that point, gradually added load with a step of 20g (0.2N), while monitoring FBG's spectrum response at each step.

According to test results, before 625g (6.13N), FBG fiber's grating wavelength shift strictly followed the rule, which has been proven by previous experiments (i.e. approximately $1.22 \square 1.24 \times 10^{-3} nm/\mu\varepsilon$).

Then when load was added one more step (i.e. to 645g, or 6.32N), the fiber broke in the FBG section, consequently the original grating pattern was damaged. Since only partial of the FBG grating left and still connected to OSA, one can observe a reflection spectrum as in Figure 3.9, showing the level of background noise rises up significantly after grating is broken.

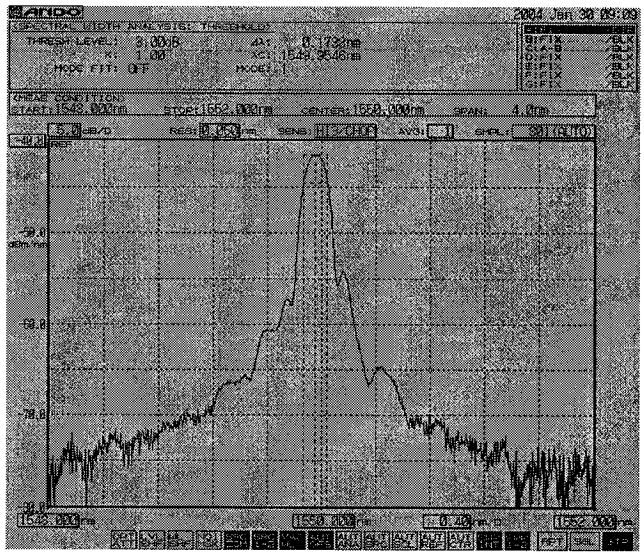

Figure 3.9 Optical Spectrum Behavior When FBG Grating in Fracture

From above tensile strength measurement, one can draw the conclusion that:

(1) Since the fiber broke in FBG section, it is assumed in-fiber grating inscription degrades optical fiber's tensile strength, hence mechanical parameters specified for common optical fiber are not suitable for FBG fibers;

(2) Testified tensile strength of the FBG fibers from certain manufacturer is less than its specified value, therefore a modified tensile strength of approximately 72kpsi (498N/mm^2) or equivalently extreme strain of 6700με will be applied in further experimental prediction.

(3) The wavelength behavior of FBG grating in fracture was observed, which is variform from the normal state since the original FBG apodization is disturbed. Therefore when one observes a spectrum apparently different from its normal shape during the measurement, it maybe the sign of damage experienced by FBG sensor.

3.1.3 Experimental Uncertainty

Due to the limitation of experimental conditions, as well as the uncertainty of the instruments involved in the measurement, substantial errors are induced in the conclusion. Major errors are induced by: (1) optical fiber's coating induces error since it bears a small part of the load; (2) OSA's uncertainty; (3) Temperature fluctuation effect; (4) deviation of the standard weights; (5) Uncertainty induced by displacement transducer; and (6) optical fiber length error. Below is a quantification of the effective errors with subject to all these elements. However, inscription induced elastic modulus variation in fiber's grating section and additional deviation of FBG grating's strain sensitivity at different wavelengths are not considered.

	Fiber Coating* (1)	OSA Accuracy (2)	Temperature Fluctuate (3)	Weights' Deviation* (4)	Displacement Transducer Accuracy (5)	Fiber Length* (6)
Effective Error in pm	+42.7, +106.8	±10.0	±6.9	±48.0, ±120.0	±12	±24, ±60
Effective Error in με	-35.6, -89.0	±8.3	±5.7	±40.0, ±100.0	±10	±20, ±50

Note: Values before comma are for 2000 μ ε, and values after comma are for 5000 μ ε.

Table 3.2 Uncertainties Induced by Individual Causes in Experiment Step 1

(1) In the experiment, the FBG section along the optical fiber was stripped for approximately 25mm, i.e. without outer coating on the FBG section, all other part of the optical fiber was coated with Acrylate polymers. According to the elastic moduli of optical fiber's silica sector and polymer coating sector, as well as their respective cross section areas, coating of the optical fiber under test shared approximately 1.8% of the total load. This means in the experiment, the total fiber's elongation was 1.8% less than what had been expected for a fiber without coating, or in another word, FBG's central wavelength shift was over-calculated by 1.8%.

(2) According to the operation manual, Optical Spectrum Analyzer AQ-6319 has an accuracy of ±10pm if the scan is in range of 1520nm to 1580nm with specified resolution setting in the experiment [29], which equals to ±8.3με for FBG fiber.

(3) During entire measurement, a thermometer simultaneously monitored environmental temperature. The fluctuation ranged around ±0.5°C during the test session for both 2000με and 5000με measurements. Due to the thermal-optic behavior of FBG gratings, which has been depicted by equation (2.15) in last chapter, the expected temperature sensitivity of a FBG fiber at 1550nm is approximately 13.7pm/°C, or [9]:

$$\Delta\lambda_B = 13.7\times10^{-3}\Delta T \tag{3.10}$$

Consequently one can work out that ±0.5°C temperature change will induce approximately ±6.9pm central wavelength deviation, which equals to ±5.7με.

(4) Statistical measurement has been done with big amount of standard weights being used in the experiment. +2% error is an effective presumption to cover loading drift for both experiments, which equals to central wavelength uncertainty of maximum ±48pm (±40με) for 2000με measurement and ±120pm (±100με) for 5000με measurement respectively.

(5) There was no particular value specified for the displacement transducer's accuracy. However, since the transducer's resolution is 0.01mm, it is assumed the uncertainty of 0.005mm would be sufficient, which induces equivalently ±10με, or ±12pm error in measurements.

(6) Although the total optical fiber length under strain load was designed as 500mm, due to ruler and operation depended errors, ±5mm uncertainty needs to be counted, which

induced ±20με and ±50με (or equivalently ±24nm and ±60nm) deviations for 2000με and 5000με measurements, respectively.

Eventually with the theory of Root – Mean – Square errors, synthetic uncertainty is calculated through:

$$\delta_{total} = \sqrt{\sum_{i=1}^{5} \delta_i^2} \tag{3.11}$$

Hence there is maximum $+46.92\mu\varepsilon / -58.90\mu\varepsilon$ ($+70.67pm / -56.32pm$) uncertainty at 2000με, and $+112.70\mu\varepsilon / -143.60\mu\varepsilon$ ($+172.33pm / -135.25pm$) uncertainty at 5000με.

Another uncertainty worth to be noticed is, practically bare FBG fiber's grating wavelength shift dose not simply follow a linear relationship with axial strain, since along with strain changing, counted grating wavelength λ_B varies, hence induces FBG's strain sensitivity being altered.

Upon equation (2.12), for a simplest consideration, if λ_B is regarded as FBG's initial grating wavelength, whenever λ_B is varied, magnitude of grating wavelength shift $\Delta\lambda_B$ per unit strain will be subsequently altered, hence FBG's strain sensitivity being diverted. Further, optical fiber's refractive index n_{eff} is also a function of wavelength [30]. However, these effects are imperceptible in the measurement range, therefore to some extent, FBG sensor can still be regarded possessing linear axial strain-optic characteristics.

3.2 Step 2

Fabrication of FBG Array Embedded Composite Structure

Development of systems for real time health monitoring of composite structures is a continuing goal with application in both fabrication and in-service periods. Much of the

sensor research is aimed at developing sensing schemes that would ultimately behave as the structures' internal nervous system. This so-called nervous system would provide both point sensing and integrated structural sensing to assess internal and external effects on the structure. Actuators are also being developed to allow these structures to adapt certain external stimuli [31]. However, integrating fiber optic sensors into composite structure is the basis toward truly creating a smart structure.

Even though little study has been done on this topic, optical fiber embedment technique is of the essence for further applications of a fiber optic sensors, not only because the optical fiber is such a hair-like tiny and fragile thing to be handled, but also a proper way to integrate the fiber optic sensor into the desired structure is crucial to influence the accuracy of measurement as well as sensors' life time. Moreover, appropriate integration can tremendously minimize mechanical degradation of the host structure. Several aspects are involved in this topic, including:

(1) Mechanical mismatch between optical fiber and host material and consequent effects;

(2) Optimal size of the embedded optical fibers;

(3) Different choices of optical fiber coating and corresponding effects;

(4) Location and orientation of fiber optical sensor layout;

(5) Protection at optical fiber ingress/egress;

(6) Disturbance to the host structure.

3.2.1 The Materials

In this work, NCT-301 graphite/epoxy prepreg was selected to fabricate composite laminate. The manufacturer of the prepreg was Newport Adhesives and Composites Inc.

NCT-301 is a general purpose, long out-time, toughened and modified epoxy prepreg designed for the preparation of laminates. General physical characteristics are as below [32]:

Unitape Fiber Weight Range	65 to 300 gm/m² (specified nominal ± 5gm/m²)
Resin Content Range	27 to 55% (specified nominal ± 3%)
Width	Up to 39 inches (1 Meter)
Resin Content	30 to 55% (per specification)
Color	Clear to slightly opaque
Volatile Content	Less than 1.0%
Resin Flow	18% to 30% (varies with product resin content)
Roll Size	60 linear years standard
Gel Time	4-8 minutes at 275°F

Table 3.3 Physical Characteristics of NCT-301 Prepreg

The following mechanical properties are average values obtained with NCT-301 reinforcing fibers. All values are based on a 30-minute cure at 285° F with 50psi, and normalized at a 60% fiber volume [32].

Property	33 Million MOD Graphite	Kevlar	S-Glass	E-Glass
Flex STR - R/T	227ksi	96ksi	237ksi	193ksi
Flex STR - 160F	207ksi			
Flex STR - 200F	162ksi			
Flex MOD- R/T	18.1Msi	10Msi	8.1Msi	6.5Msi
Flex MOD- 160°F	16.5Msi			
Flex MOD- 200°F	12.9Msi			
Short Beam Shear - R/T	14.3ksi	9.5ksi	12.5ksi	12.5ksi
Short Beam Shear - 160°F	13.0ksi			
Short Beam Shear - 200°F	10.2ksi			
Tensile STR - R/T	320ksi		230ksi	
Tensile MOD - R/T	19.0Msi		8.2Msi	
Compressive STR - R/T	169ksi		150ksi	
Compressive MOD - R/T	19.2Msi		7.1Msi	

Table 3.4 Mechanical Properties of NCT-301 Prepreg

In the experiment, reinforcing fiber applied in the composite was graphite (i.e. described in the first column of above table), the detailed module number of the composite prepreg was NCT-301 TR50 G125 36'', resin content is 34±2%.

3.2.2 Specimens Design

In the experiment, two orthogonally geometrized composite specimens were fabricated and investigated. However, designated layup sequences of the two specimens both followed $(0_8 90_4)s$, where "0" represents ply's graphite fiber orientation being along with 0 direction (e.g. the first specimen's structural direction in this case), and subscript "8" represents 8 layers of such oriented plies are adjacently piled up; while "90" represents ply's graphite fiber orientation being along with 90 direction (i.e. perpendicular to 0 direction, or orthogonal to first specimen's structural direction in this case), and subscript "4" represents 4 layers of such oriented plies are adjacently piled up; subscript "s" out of the parenthesis represents the layup is symmetric about the mid-plane of the entire stacking. Therefore, there were totally 24 layers of plies stacked in specimens' thickness, in which 16 layers were oriented in "0" direction, and other 8 layers were oriented in "90" direction. Such a layup structure is so-called "cross-ply". Thus it is expected the specimens would present strong orthotropic characteristics.

Refer to Figure 3.10, for the first specimen, designed plate size was $200mm \times 40mm$ along its structural orientation; while for the second specimen, its designed plate size was $40mm \times 200mm$, i.e. geometrically orthogonal to the first specimen. Since the thickness of prepreg tape is approximately 125μm [32], there were totally 24 plies in the stack, hence total thickness of specimens was approximately $125\mu m \times 24 = 3000\mu m = 3mm$.

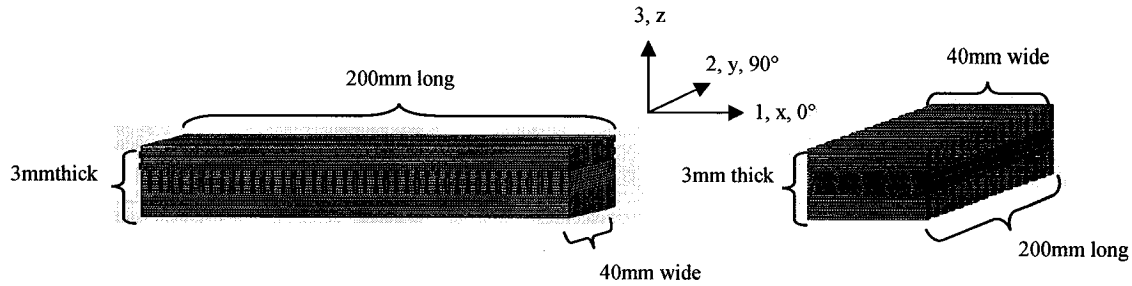

(a) Specimen I (b) Specimen II

Figure 3.10 Schematic of The Specimens

3.2.3 Sensor Array Layout Optimization

Due to orthotropic mechanical characteristics of Graphite/Epoxy composite laminates, two separate FBG sensors were orthogonally embedded along two principle axes in each specimen (specimens' structural coordinates coincide with principle coordinates in this case). When strain was applied along one of the axes, longitudinal and transverse responses of the specimen were simultaneously monitored, hence structure's orthotropic properties are determined. Further, any randomly oriented strain applied to the structure will be analytically reduced along the two sensors. Hence as discussed in chapter 2, a unit cell of entire FBG sensor network is studied.

(1) Plane Location

There are reports that strain transfer from host to embedded optical fiber will be degraded if stress field is axially varied [33]. Figure 3.11 shows the situation under consideration. Where embedded optical fiber sensor is modeled as an infinitely long axisymmetric system: optical fiber has radius r_f and surrounding material has radius R; both materials are considered isotropic. At $r = R$ an axially varied strain field exists, i.e. $\in_z^m (R,z)$. Consequently in-fiber strain field transferred from host can be expressed as $\in_z^f (z)$.

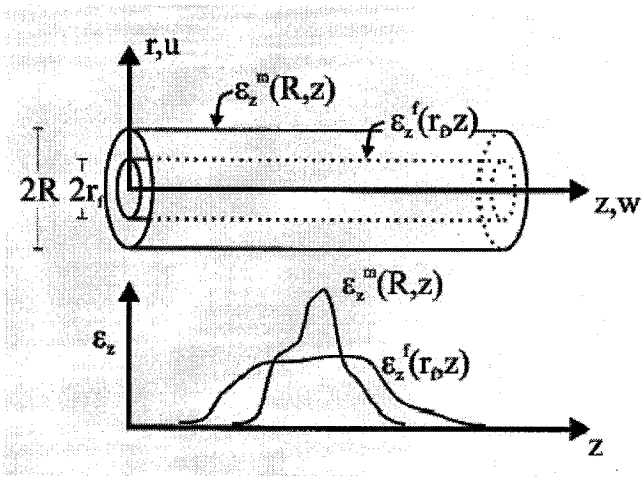

Figure 3.11 Strain Transfer From Host to Fiber Sensor

Solved by Fourier decomposition, ambient strain field can be transformed from z-domain to k- domain function, i.e.:

$$\in_z^m (R,k) = \int_{-\infty}^{+\infty} \in_z^m (R,z) \exp(-2\pi ikz) dz \tag{3.12}$$

$$\in_z^f (k) = \int_{-\infty}^{+\infty} \in_z^f (z) \exp(-2\pi ikz) dz \tag{3.13}$$

k also indicates the extent of axial strain field gradient along z direction, (i.e. when k increases, strain field gradient will also increase). With verbose mathematic deduction upon the boundary condition, strain field transfer function of the system, with respect to k, can be inferred as:

$$H(k) = \frac{\in_z^f (k)}{\in_z^m (R,k)} = \frac{1}{(2\pi k r_f / n)^2 + 1} \tag{3.14}$$

where n is the shear-lag parameter, which encapsulates the effects of both geometry and relative stiffness of the elements in the system. From equation (3.14), one can make deduction that: as with k increase, indicating shorter-spatial-period of strain field distribution along z-axis, transfer gets progressively weaker; or in another extreme, a constant strain field $\in_z^m (R,z) = c$ (i.e. when k = 0) will be perfectly transferred.

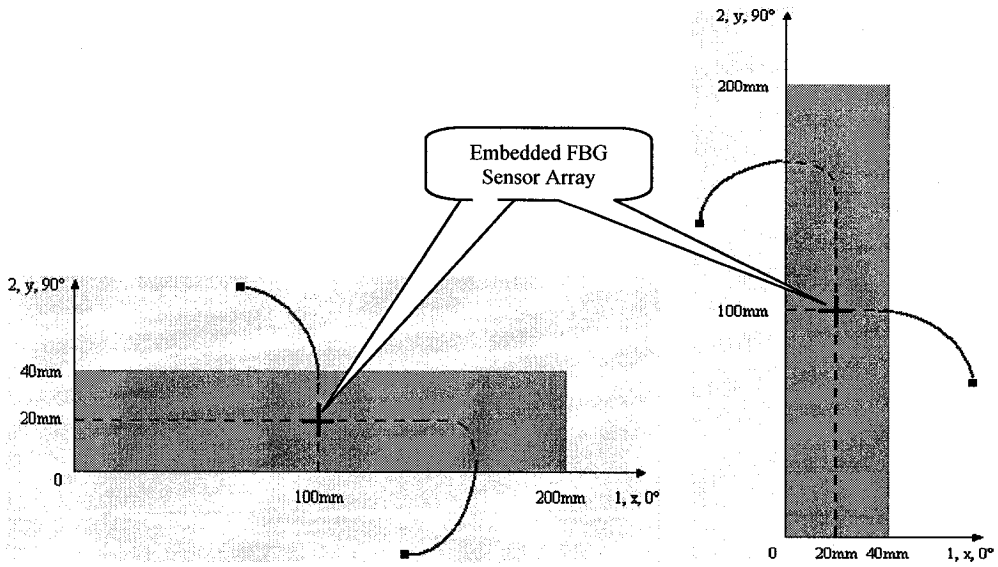

(a) Specimen I (b) Specimen II

Figure 3.12 FBG Sensors Location Top View

Upon above discussion, in order to obtain the most legible module for further evaluation, comparatively constant axial strain field becomes essential in the investigation. Following the same criterion as resistance strain gauges, although FBG sensor features approximately 14mm gage length, geometric center of the specimen is likely the place where secures the best expected strain transfer from host structure to the embedded sensors. FBG array plane location top views are illustrated as in Figure 3.12.

(2) Resin-Rich Pocket Suppression

For the purpose of simultaneously measuring strains along longitudinal and transverse directions, an orthogonal FBG array was embedded in each specimen, in which the two FBG sensors were deployed parallel and perpendicular to tensile load (and specimen's structural) direction, respectively. Hence two further concerns arise, which may seriously influence sensors' performances, as well as alter host structure's mechanical properties:

(1) Should FBG fibers be deployed parallel or perpendicular to the neighboring reinforcing fibers?

(2) Where should the FBG fibers be better placed in the layup sequence?

One must recognize that optical fibers are foreign entities to the host structure therefore always alter the stress field in vicinity of the embedded sensors. This inescapable truth of continuum mechanics is a result of the structural discontinuity introduced by optical fiber, and occurs irrespective of the small size of the fiber [19].

Many of the concerns about the obtrusiveness have focused on interlaminar lenticular resin-rich pocket, which forms when optical fibers are buried in laminated composite, since this resin pocket acts as an interlaminar discontinuity and poses potential reliability hazard to both sensor and host structure under static, cyclic, or shock loads [34]. By means of finite element analysis (FEA), it has been proven that the larger the resin-pocket, the more concentrated the stress field experienced by embedded optical fiber, the better opportunity a hazardous mechanism is locally incurred, and the more noise is induced to desired sensing response [35]. Then the first concern is interpreted as: What layout scheme could best minimize resin-rich pocket around FBG fiber, hence reduce the harmful effects to both host and sensors.

According to the literature, it is reported that resin pocket becomes smaller as the angle between optical fiber and adjacent reinforcing fibers decreases [36]. Upon this conclusion, discontinuity (resin pocket) in the structure will be minimum when FBG fiber is deployed parallel to neighboring reinforcing fibers, and maximum when FBG fiber is perpendicular to neighboring reinforcing fibers.

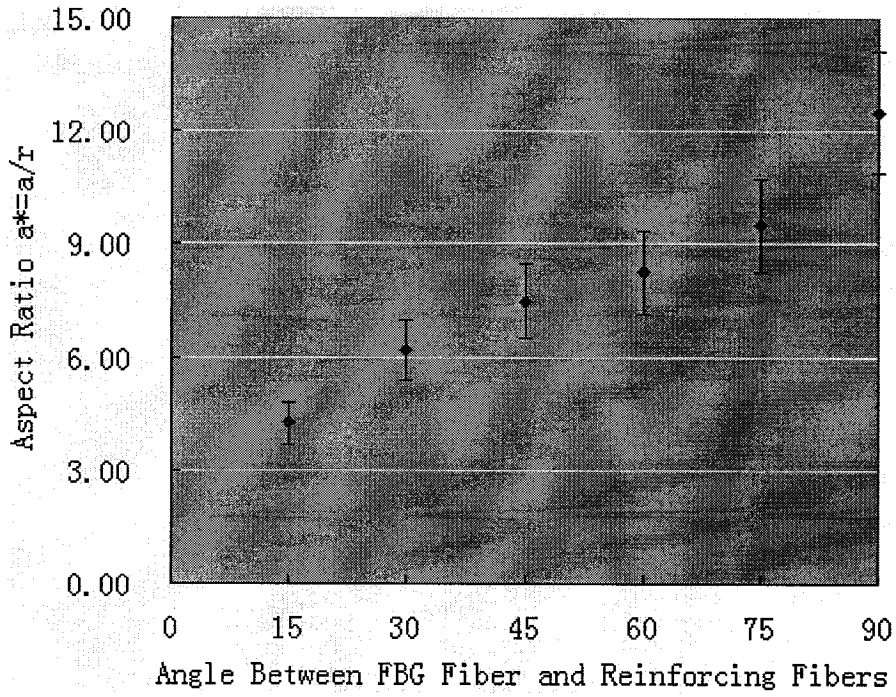

Figure 3.13 Experimental And Analytical Results of Resin-Pocket Geometry [36]

In the experiment, an unidirectional reinforced pre-specimen was fabricated with ordinary optical fibers embedded parallel and perpendicular to the reinforcing fibers, i.e. the two extreme cases for the relative orientation between optical fiber and reinforcing fibers. The pre-specimen was cut in stripes along and perpendicular to its reinforcing fiber direction, hence resin-rich pockets were exposed in the edges of the stripes. Afterward, these stripes were observed under SEM (Scanning Electron Microscope), and shapes of resin-rich pockets were photographed for the two extreme cases.

Upon observation, it is proven that when optical fiber is buried perpendicular to neighboring reinforcing fibers, a prolate and remarkable resin-rich pocket is generated around optical fiber, which apparently induces severe structural discontinuity, hence damages both host and FBG sensor's performances. On the other hand, there is almost no resin-rich pocket observed when optical fiber is embedded along with neighboring

reinforcing fibers, therefore structure is optimized, hence induces the least disturbance to continuum mechanics.

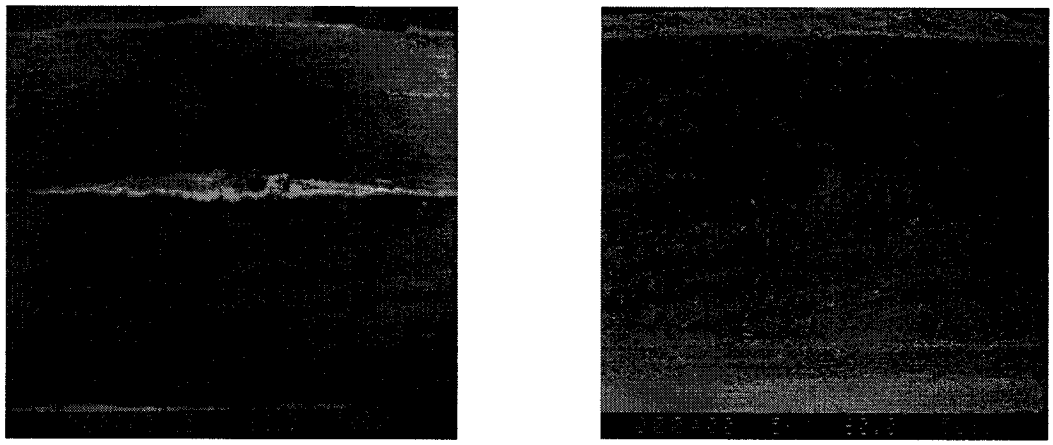

(a) (b)

Figure 3.14 Morphology of Resin-Pockets

(a) Optical fiber is buried perpendicular to neighboring reinforcing fibers

(b) Optical fiber is buried parallel to neighboring reinforcing fibers

(3) Layup Location

According to the literature, it has been observed that the closer the embedded optical fiber to the outer layer or the interface between two cross-plied layers, the more deformation induced to inner and outer structure of the host, thus leads to more serious stress field perturbation in the continuum, and adds more noise to FBG's optical response [19]. It has been modeled that when deployed parallel to neighboring reinforcing fibers, if optical fiber is embedded four layers away from laminate's surface or the interface between two cross-plied layers, induced structural deformation will be sufficiently suppressed. Therefore, the second concern about FBG fiber's embedment location is effectively answered, which considers where the optimal place is for FBG sensors among laminate's stack.

According to above discussions, it was determined the FBG array embedded laminate specimens followed this layup sequence: $(0_4F_00_4904_4F_{90}90_40_8)$, i.e. FBG fibers were always parallel to neighboring reinforcing fibers, in which sensors along 0 direction were deployed between the fourth and fifth layers, and sensors along 90 direction were deployed in the mid-plane of the laminate (i.e. between the twelfth and thirteenth layers). The anatomic diagram of the two specimens is shown in Figure 3.15.

From Figure 3.15, it can be seen that FBG sensors with shorter grating wavelength were always oriented parallel to tensile load direction (i.e. along with specimens' structural direction), while FBG sensors with longer grating wavelength were always oriented perpendicular to tensile load direction (i.e. perpendicular to specimens' structural direction).

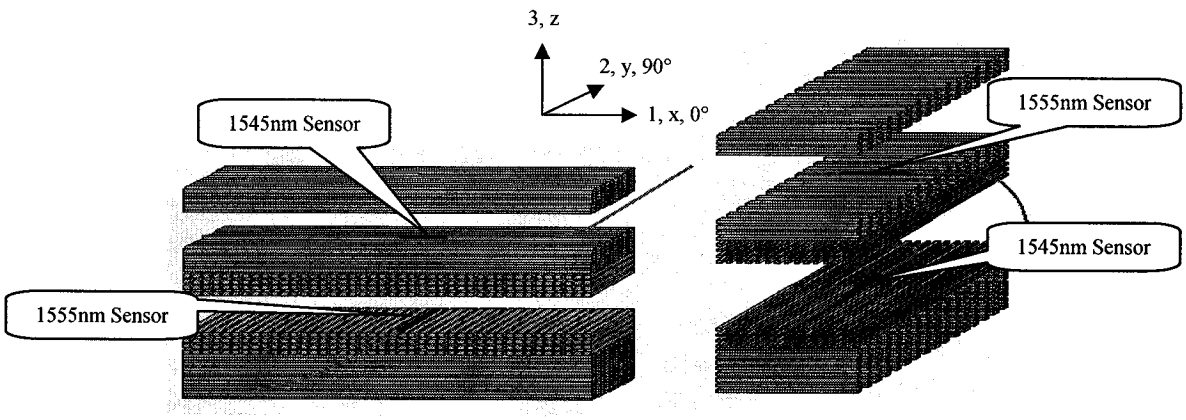

(a) Specimen I (b) Specimen II

Figure 3.15 Schematics of FBG Array Layout

(3) FBG Fiber Coating

Up to now, in order to obtain optimal sensing capability, as well as to minimize disturbance to host structure, two further issues need to be justified in FBG sensor design:

(1) How to minimize transverse stress field perturbation in vicinity of the embedded optical fibers, and

(2) How to maximize longitudinal strain transference from host to FBG sensors.

It is believed one of the solutions to optimize the interaction between optical fibers and surrounding host is to choose the proper type of optical fiber's coating, and to determine optical fiber's diameter [19].

In vicinity of an embedded FBG fiber, stress field concentration previously discussed can be tailored by sensor designers through judicious use of optical fiber's coatings [37], thereby coating in the analysis provides an additional freedom in design process. There are two types of optical fiber coatings commercially available: Acrylate coating and Polyimide coating. Figure 3.16 illustrates the cross sectional status of the two coatings. Outer diameter of acrylate coated fiber is approximately 245μm, well polyimide coated fiber is approximately 155μm. According to the literature, it has been proven that, the smaller the optical fiber's diameter, the less transverse stress field concentration occurring in vicinity, therefore polyimide is nominated to coat embedded FBG fibers. Not only, polyimide performs better adhesiveness than acrylate in high temperature, this benefit secures the formation of superior viscid bonding between optical fiber and surrounding host through composite curing process.

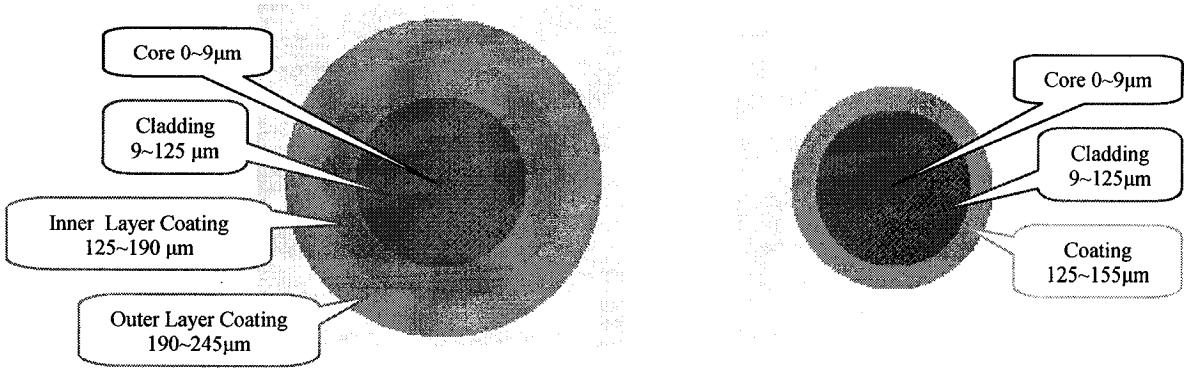

(a) Acrylate Coated (b)Polyimide Coated

Figure 3.16 Cross Sections of Different Coated Optical Fibers

In the experiment, cross sectional status of different coated optical fibers were also observed with the pre-specimen. Acrylate coated fibers were deployed interleaved with polyimide coated fibers in the specimen, the spatial interval between two neighboring optical fibers was about 20mm in parallel. Two extreme layout schemes - parallel and perpendicular to neighboring reinforcing fibers, were both deployed and observed.

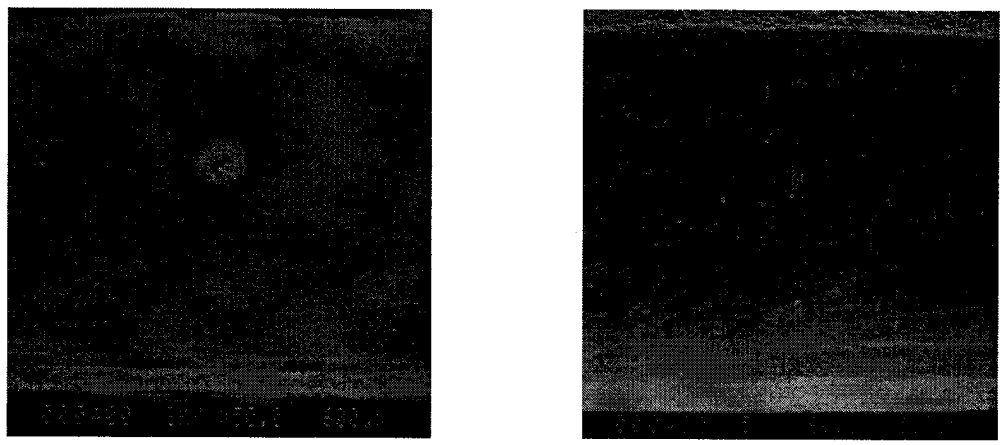

(a) Acrylate Coated (b) Polyimide Coated

Figure 3.17 Embedded Optical Fibers' Cross Sectional Status

Upon Figure 3.17, it is proven that when both buried parallel to the neighboring reinforcing fibers, polyimide coated optical fiber has smaller cross sectional geometry than Acrylate coated optical fiber, thus induces less structural discontinuity. Meanwhile, it is also proven Polyimide coating possesses better viscosity than Acrylate coating after composite curing process, during which high temperature is applied. After the pre-specimen was fabricated, detachments in surrounding resin-rich pocket were observed with Acrylate coated optical fibers, when they were deployed perpendicular to the neighboring reinforcing fibers. However, Polyimide Coated fibers always presented being glued well.

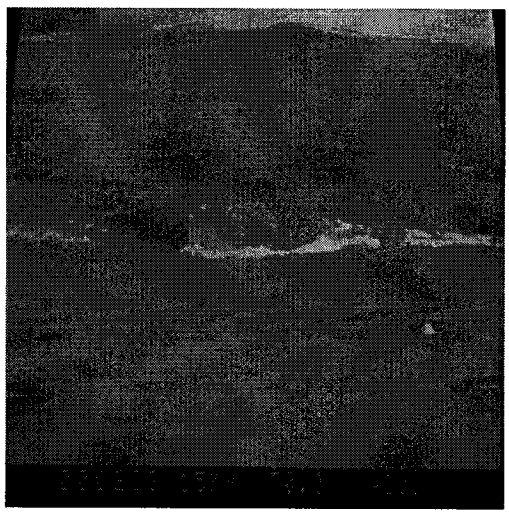

Figure 3.18 Detachment In Surround Resin-Rich Pocket with Acrylate Coating

3.2.4 Fabrication Process

In the experiment, optical fiber embedded composite specimens' fabrication progress was created by mechanical engineering department, and conducted cooperatively by author and the mechanical engineering student, with facilities in mechanical engineering department. Major steps involved in the progress include:

(1) **Prepreg Layup**. Graphite-epoxy prepreg was cut into certain number of desired patterns. After cleaning the surface, all these patterned plies are laid up following specific sequence (i.e. $(0_8 90_4)_s$ in this case).

(2) **FBG Fiber Deployment**. Simultaneously during plies laid up, FBG fibers were deployed between appropriate layers and along desired orientations. The rest of the optical fibers exposed out of specimens were protected with 0.9mm Teflon buffers, which are able to withstand high temperature up to 500°C, so that optical fibers' ingress/egress was protected.

(3) **Molding**. After being laid up, air bubbles were preliminarily eliminated by ironing prepreg stacks. Refer to Figure 3.19, raw ply stacks were sealed in a fabrication mold.

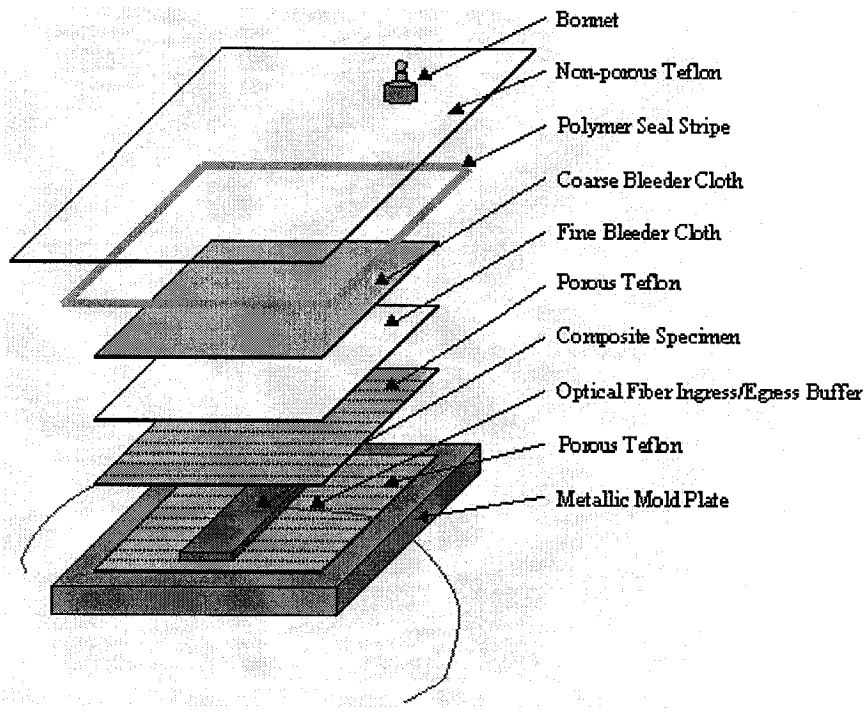

Figure 3.19 FBG Fiber Embedded Composite Laminate Fabrication Mold

(4) **Curing**. After raw samples being molded, sealed mold was put in an autoclave chamber for desired curing process. The mold was vacuumed in the autoclave to

remove remaining air and volatile gas generated during polymerization of the matrix. Epoxy matrix is a thermoset plastic material. After curing process, thermoset matrix dose not soften upon further heating because the polymerization reaction is irreversible. The matrix passes through various phases, from viscous to viscoplastic, to viscoelastic, and finally to elastic, when curing process ends. Permanent bonds exist afterwards between matrix and fibers and between adjacent laminae. Matrix will no longer melt when a high temperature is applied [38].

Entire autoclave curing cycle is depicted in Figure 3.20. Generally, the curing cycle of Graphite/Epoxy composite consists of three stages: In stage I, temperature in the chamber is increased to an intermediate temperature (105°C) and held for 15 minutes to decrease the viscosity of resin, meanwhile air pressure is risen up to 60psi in the chamber; In stage II, temperature is increased to final cure temperature (145°C) and held for 45 minutes, while air pressure is kept with 60psi; In the final stage (stage III), composite is naturally cooled down to room temperature and air pressure is released to normal.

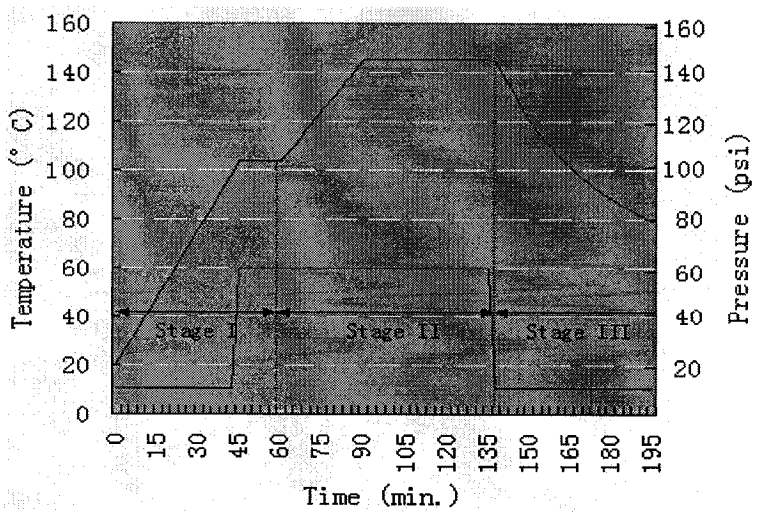

Figure 3.20 The Curing Cycle

(5) **Trimming**. After curing process, specimens were removed from autoclave chamber and taken from the mold. Specimens' edges can be trimmed by diamond saw. Special care must be taken when trimming the edges where optical fibers are ingress/egress. Final status of the specimens is as in Figure 3.21.

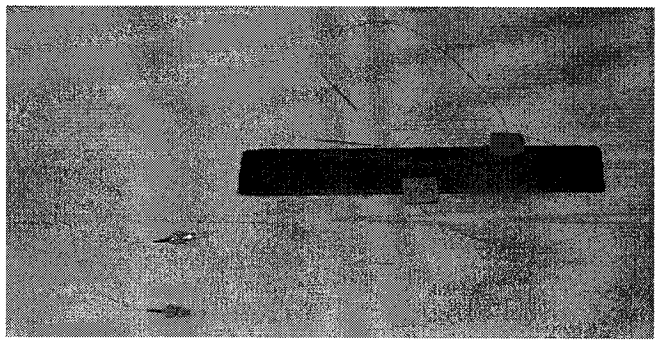

Figure 3.21 Final Status of The Specimens

Below is the detailed information regarding major facilities involved in FBG fiber layout observation and composite specimen fabrication.

	Autoclave System	Scan Electron Microscope (SEM)
Model Number	C0102.6	S-520
Serial Number	3241	108130
Manufacturer	Mecano Soudure Drummond Ltée	Hitachi

Table 3.5 Facilities Involved in Experiment Step 2

3.2.5 The Outcome

There were two FBG sensors embedded in each specimen, which were deployed orthogonal to each other. After fabrication, all sensors were physically survived, changes of their optical characteristics were tracked before and after embedment.

		Central Wavelength (nm)		Reflectivity (dB)	
		Before	After	Before	After
Specimen I	**1545nm Sensor**	1544.5747	1544.5740	~30.00	~20.00
	1555nm Sensor	1554.5735	1554.4695	~30.00	~15.00
Specimen II	**1545nm Sensor**	1544.5032	1544.3233	~25.00	~20.00
	1555nm Sensor	1554.6308	1554.6709	~25.00	~20.00

Note: Environmental temperature fluctuates within 0.5 C during the measurement.

Table 3.6 FBG Gratings' Optical Characteristics Before and After Curing

(1) Grating Wavelength Shift

Due to thermal expansion mismatch between optical fiber and surrounding materials, it is expected FBG sensors' grating wavelengths will be shifted after curing, which is resulted from residual thermal stress along and transverse to buried optical fibers. Some researches have observed that embedded FBG sensors' grating wavelengths became shortened by the end of the curing cycle [39]. It is believed this phenomenon is resulted from the thermal evolvement of surrounding resin matrix during curing progress. Refer to Figure 3.22 [32], when ambient temperature in autoclave chamber rises up to about 105°C, resin's viscosity reaches its minimum point so that it crams through the plies. At this stage, FBG fiber is comparatively free from bonding with resin matrix. With temperature continuing to rise, resin's viscosity increases rapidly because molecular cross-links are generated. Then passing through gel point, resin's viscosity still rises up until the highest temperature of curing cycle (i.e. 145°C in the experiment), where embedded FBG fibers experience the strongest bonding with host resin [40]. During the last stage, autoclave chamber cools down naturally, while resin matrix shrinks along with the cooling progress without viscous degradation, which causes encompassed FBG fibers being contracted in all directions due to the strong bonding and the fact that optical

fiber's thermal expansion coefficient being smaller than resin by approximately 10^2 (thermal expansion coefficient of resin epoxy is $(6\pm1)\times10^{-5}$, while the coefficient of optical fiber is 5.5×10^{-7}). Eventually FBG fibers' axial compressive strain leads to negative grating wavelength shift after embedment. Upon experimental results, one may find that grating wavelengths shortened for majority FBG sensors after embedment, thus theoretical expectation is proven.

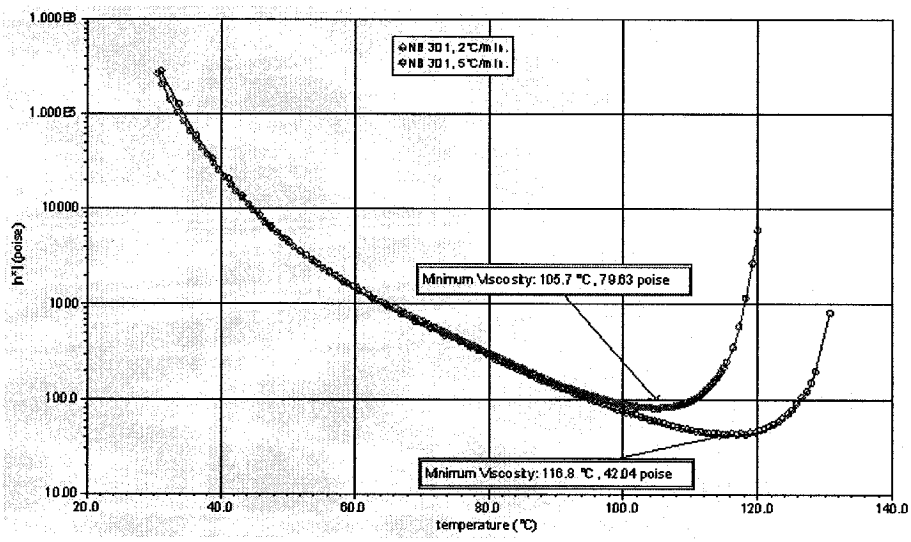

Figure 3.22 Viscosity vs. Heat Rate for NCT-301 Resin Epoxy [32]

(2) Reflectivity

From Table 3.6, one may be aware of that FBG gratings' reflectivity was apparently decreased after curing process. This degradation is mainly caused by the thermal decay of FBG grating mechanism.

As discussed in last chapter, FBG grating formation involves laser-induced excitation of Ge-doped SiO_2's outer electrons into a meta-stable band. As a result, grating will decay over time at elevated temperature. It has been observed that a slow decay follows rapid initial decay through a decay mechanism, in which carrier initially excited

during FBG generation are trapped into broad distributed energy trap states (this is consistent with the amorphous nature of silica). Rate of thermal depopulation was an activated function of trap depth, which depends on different types of optical fibers (e.g. hydro- and non-hydrogenated optical fibers) [41].

Due to equation [30]

$$R = (\frac{n_1 - n_2}{n_1 + n_2})^2$$

$$= (\frac{\Delta n}{n_1 + n_2})^2 \qquad (3.15)$$

where R is the reflectivity of the interface between two transparent media, n_1 and n_2 are the refractive indices of the two media respectively, thermally induced grating decay results in decrease of Δn, consequently causes degradation of FBG's reflectivity.

In order to obtain consistent reflectivity after curing cycle, pre-annealing on FBG fiber is required.

3.3 Step 3

Investigation and Calibration of Embedded FBG Strain Gage Array

Although FBG sensors survived throughout composite fabrication, it can be concluded from previous observation that natural host structure is perturbed due to the foreign entity – FBG fiber, thus complex transverse stress field is interactively induced between host material and embedded optical fiber. Consequently, sensor's optical and mechanical behaviors may deviate from its bare status as has been obtained in the first experimental step, therefore recalibration becomes necessary so that embedded FBG sensor can factually reflect the strain of the host structure. Furthermore, as have been

proposed at the beginning of this chapter, two suspicions need to be answered whenever FBG sensor is desired to be an embedded strain gage:

(1) May embedded FBG sensor fail before reaching desired measurement range, so that render the sensor useless for further transduction task?

(2) To what extent the interpretation of embedded FBG sensor's optical behavior is altered due to additional radial stress when host specimen is under tensile stress? Or in the other word, how does embedded FBG strain gage's sensitivity deviate from its bare fiber state?

In following discussions, it is tried to reveal the solutions through theoretical analysis and experimental observation, so that feasibility of "fiber optic smart structure" can be eventually evaluated.

3.3.1 Theoretical Prediction

(1) Failure

Since the size of possible surface flaws on optical fiber is in range of nanometer, which are mainly caused during manufacturing, this means in order to produce brittle fracture, stress level in range of gigapascal is needed. Moreover, since FBG fiber's layout orientation was chosen always parallel to neighboring reinforcing fibers, which utmost prevent embedded FBG fibers from further appreciable flaws. It is hence reasonable to suppose that fracture will not be a common phenomenon for embedded sensors.

(2) Sensitivity and Accuracy Deviation

Besides thermal effects, embedded FBG strain gage's interpretation issue is manifested in additional radial strain sensitivity. In more revealing form, optical

retardation in any interferometry based fiber optic sensor (e.g. grating wavelength shift of FBG sensor) can be expressed in terms of strain field dependent optical path length [42]:

$$\Delta\phi = \frac{2\pi}{\lambda}\iint\left[\left(1+\varepsilon_z^f\right)n\left(\varepsilon_i^f\right)\right]d\varepsilon - \phi_0 \tag{3.16}$$

where λ is the wavelength of launching light, n is the effective refractive index of optical fiber, ε_i^f is the strain tensor depicting strain field existing in the fiber, and ε_z^f is the normal strain component tangent along the axis of the sensor fiber. Apparently optical retardation no longer relates only to axial strain, instead, the issue is extended to three dimensions.

Upon equation (2.12) and (2.13), consider axial stress is applied exclusively, FBG sensor's grating wavelength shift follows:

$$\begin{aligned}\frac{\Delta\lambda_B}{\lambda_B} &= \left\{1-\frac{n_{eff}^2}{2}\left[p_{12}-\mu\left(p_{11}+p_{12}\right)\right]\right\}\varepsilon_z \\ &= \varepsilon_z - \frac{n_{eff}^2}{2}\left[p_{11}\left(-\mu\right)\varepsilon_z + p_{12}\left(1-\mu\right)\varepsilon_z\right]\end{aligned} \tag{3.17}$$

Nevertheless, after integrated in the structure, three dimensional stress field is locally induced, resulting the sensor in non-negligible response to extra radial strains. Referring to the simplified model in Figure 3.23, addition to axial strain, FBG strain gage embedded in host material is also subject to a plane – strain radial compression, which can be always analytically reduced into two orthogonal tensor components along axes x and y (transverse compression is not necessarily circumferentially uniform for most cases).

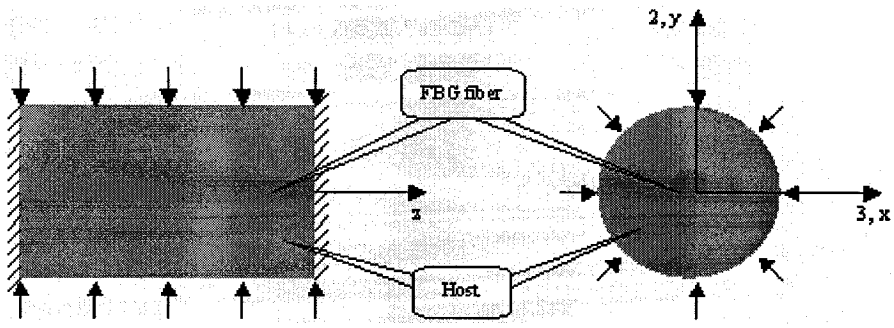

Figure 3.23 Embedded FBG Strain Gage Under Plane-Strain Radial Compression

Refer to the deduction in Appendix, under three dimensional stress field, FBG's grating wavelength shift becomes [43]

$$\frac{\Delta\lambda_{B,x}}{\lambda_B} = \varepsilon_z - \frac{n_{eff}^2}{2}\left[p_{11}\varepsilon_x + p_{12}\left(\varepsilon_y + \varepsilon_z\right)\right] \tag{3.18}$$

$$\frac{\Delta\lambda_{B,y}}{\lambda_B} = \varepsilon_z - \frac{n_{eff}^2}{2}\left[p_{11}\varepsilon_y + p_{12}\left(\varepsilon_x + \varepsilon_z\right)\right] \tag{3.19}$$

where $\Delta\lambda_{B,x}$ and $\Delta\lambda_{B,y}$ are FBG's grating wavelength shifts in x and y polarizations respectively; ε_x, ε_y and ε_z are the three principle strain tensor components in the core of FBG fiber. Therefore, two hypotheses are given based on above discussion:

(1) If embedded FBG strain gage is subject to radial compression only, but is prevented from any axial normal expansion, one could still expect grating wavelength shift of the gage. This is because although no change in length, according to equation (3.16), FBG fiber's effective refractive index is a function of in-fiber strain field, period. Putatively if, for example, sensor is considered to contain axial strain information only, there will be error arising in measurand interpretation.

(2) If radial compression is remarkably non-uniform along x and y directions, FBG's grating wavelength shifts will be perceptibly apart between x and y polarization

states of entire optical response. Hence one may observe reflection spike or transmission notch split due to the induced birefringence.

Acting as "referential" tensors, extra radial strain induces deviation to FBG sensor's intrinsic axial strain-optic behavior, hence alters embedded strain gage's measurement. Beyond pivotal recalibration, sensor designers still need to obtain the knowledge about: to what extent embedded strain gage's performance has been deviated, or in the other word, whether desired axial measurand could be possibly overwhelmed in erroneous noise?

3.3.2 Experiment Design

(1) The Setup

In the experiment, Universal Test Machine (UTM) was used to apply static load to each specimen. Refer to Figure 3.24, UTM machine is a hydraulic system, which can be used either automatically or manually. Through balancing "load" and "unload" controls, static load can be achieved at desired levels. Three load ranges can be performed by this system: ~1.2K pounds (5.3KN), ~12K pounds (53.3KN), and 60K pounds (266.7KN). In order to compromise between accuracy and convenience, 12K pound range was applied. Refer to Figure 3.26, composite specimens were vertically griped between upper and lower heads in UTM's frame. Firstly, kept open the load valve until the reading on load meter approached desired value, then gradually closed load valve simultaneously opened unload valve, so that load eventually stopped at the level. At this moment, readings of surface mounted resistance strain gage array and embedded FBG strain gage array were recorded by strain indicator and OSA, respectively.

Afterward, gradually reopened load valve and closed unload valve to reach the next desired load value.

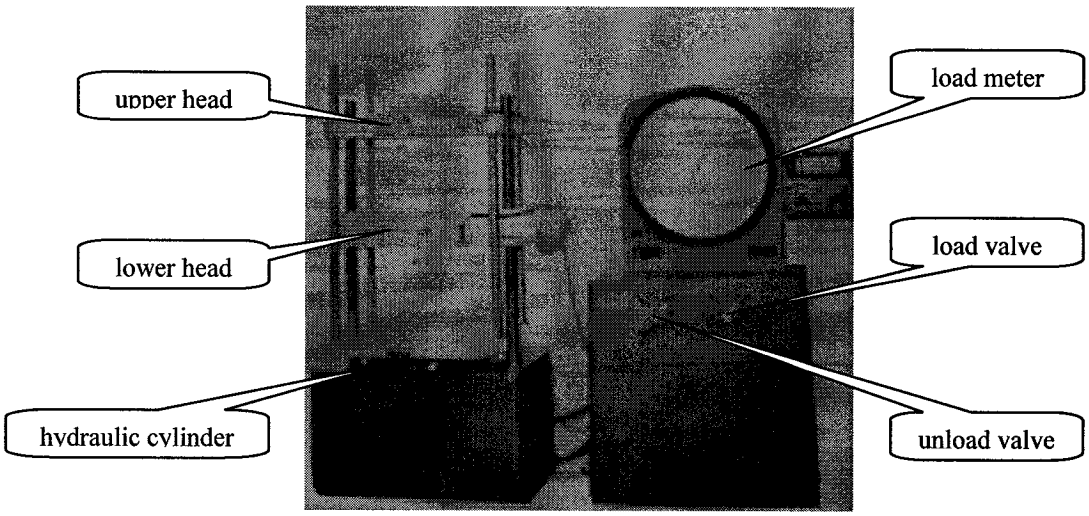

Figure 3.24 Universal Testing Machine [44]

Two identical resistance strain gages were orthogonally mounted on both sides of each specimen separately (i.e. one gage was mounted on one side of the specimen parallel to load and structural orientation; while the other gage was mounted on the other side of the specimen perpendicular to load and structural orientation). Geometric locations of two resistance gages coincided with those of embedded FBG gages in the specimen. A multi-channel strain readout system was connected to surface mounted gages, hence strain values were read and logged. Surface mounted resistance gages were used to recalibrate FBG gages, as well as to evaluate the applicability and erroneous deviation of embedded FBG strain gage network.

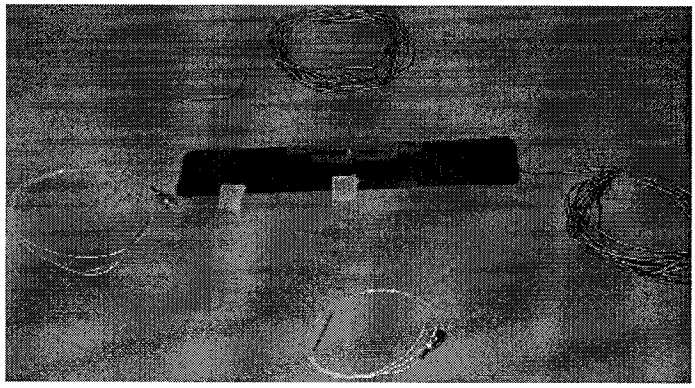

Figure 3.25 Both FBG Gage Array And Resistance Gage Array Were Deployed

Since two embedded FBG sensors need to be monitored simultaneously, a 50/50 1×2 optical coupler was added in light path, so that broadband light was equally split into two orthogonal FBG gages. Meanwhile, reflections from the two were recombined and transmitted to OSA's detector. In order to obtain reflection spikes to facilitate further analysis, a three port optical circulator was deployed between OSA and optical coupler. Connection of the circulator followed the same criterion as the 2^{nd} optical scheme introduced in the first experimental step (refer to Figure 3.2 (b)).

Similarly as in the first experimental step, OSA's internal broadband LED source was used, and FBG sensors' grating wavelength shifts were monitored by OSA.

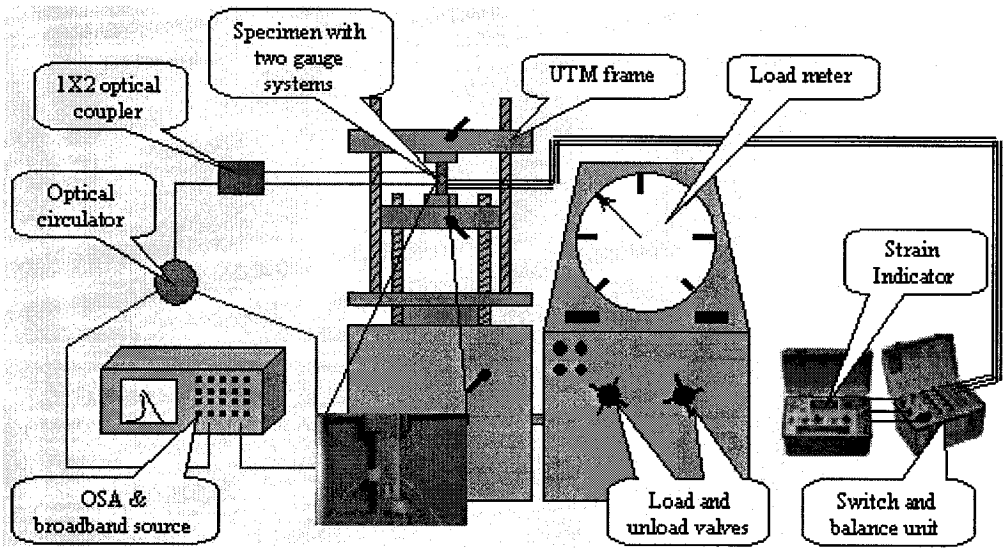

Figure 3.26 Schematic of Test Setup for Experiment Step 3

(2) Measurement Arrangement

During experiment, specimens were desired to withstand more than 2000με tensile strain along their long edge directions. For the simplest presumption, suppose no delamination occurring in dedicated measurement range, and regard the cross-plied structure with linear elastic properties along two in-plane principle directions.

Considering a linearly elastic composite structure, its effective elastic modulus in terms of the compositive force-bearing cross section is expressed as

$$E_{tot} = \sum_{i=1}^{N} E_i \frac{A_i}{A_{tot}} \tag{3.20}$$

where E_{tot} is the synthetic elastic modulus of the structure, E_i is individual elastic modulus of each element, A_{tot} is total load-bearing cross sectional area, and A_i is load-bearing cross sectional area of each element.

According to the technical data published by prepreg manufacture, for a 10 plies unidirectional structure, its elastic moduli are 18.55Msi and 039Msi in reinforcing fiber

(0 direction) and matrix (90 direction) directions, respectively [32]. Regarding the two specimens under study, since each specimen's total load-bearing cross sectional area is approximately 120mm^2, and neglect fabrication induced mechanical degradation:

(1) For specimen I, 2/3 of its load-bearing cross section features 0° direction elastic modulus, while the rest of 1/3 features 90° direction elastic modulus. Hence its effective modulus is approximately 12.83Msi, so that 21KN (~4.7K pound) tensile load is required to achieve 2000με longitudinal strain.

(2) For specimen II, 1/3 of its load-bearing cross section features 0° direction elastic modulus, while the rest of 2/3 features 90° direction elastic modulus. Hence its effective modulus is approximately 7.11Msi, so that 12KN (~2.7K pound) tensile load is required to achieve 2000με longitudinal strain.

However, due to mechanical uncertainty induced by laminate fabrication, as well as specimens' non-linear elastic property, recordation progress needs to be tactfully adjusted during the measurement.

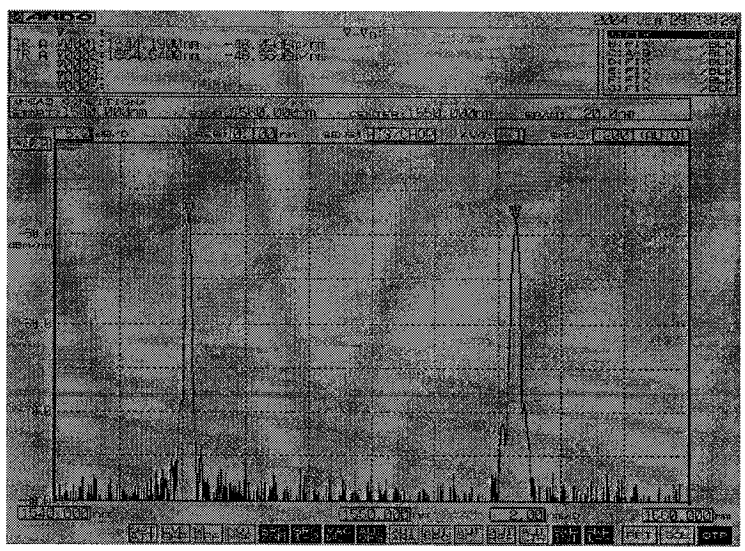

Figure 3.27 Two Reflectance Spikes Acquisitioned in A Single Scan

Regarding the orthogonal FBG strain gage array in each specimen, in order to facilitate interrogation, two reflection spikes (around 1545nm and 1555nm for the two sensors respectively) will be acquisitioned in a single scan by OSA.

(3) Material List

Below is the list of equipments used in measurement.

	OSA	light source	UTM system	resistance strain gage
Model Number	AQ6319	AQ6319		CEA-06-250UW-350
Serial Number	20382604	20362804		132022-3247 / 3254
Manufacturer	Ando	Ando	Tinius Olsen	Measurements Group Inc.
Resolution	0.01 ~ 0.5nm	< −10dBm	10lb	0.01με
Sensitivity	< ±10pm (1520~1580nm)			

	strain indicator	switch & balance unit	1 X 2 optical coupler	optical circulator	thermometer
Model Number	P-3500	S8-1	22-10331-50-33810	PICT-1550-S	CT485RS
Serial Number	0148691	008011	H14115	00TE0259	024983P
Manufacturer	Vishay Measurement Group	Vishay Measurement Group	Gould Fiber Optics	Oyokoden Lab Co. Ltd.	Omega Engineering Inc.
Resolution	1με				0.1°C
Sensitivity	0.5με				0.1°C

Table 3.7 Instruments Used in Experiment Step 3

3.3.3 The Results

(1) Composite Structure's Mechanical Properties

It must be noticed that the determination of composite structure's mechanical properties is not a topic in this work, since all discussions are exclusively restricted in the study of embedded FBG sensor network. However, some brief structural parameters have to be obtained for purposes of FBG gages recalibration and further discussion.

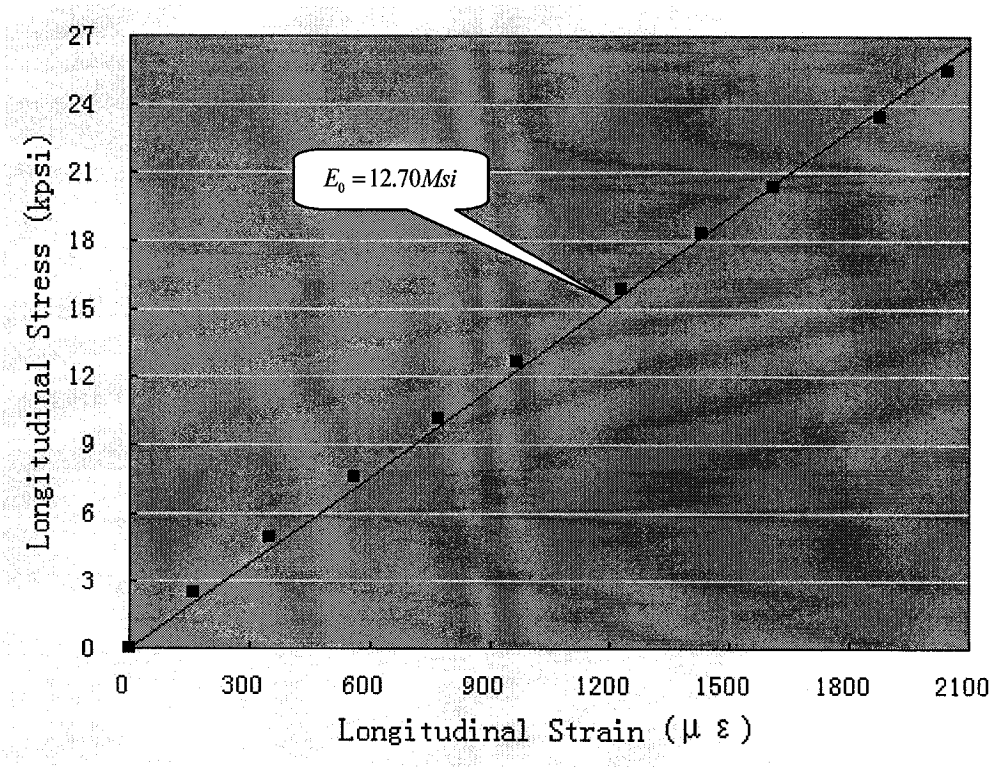

(a) Strain - Stress For Specimen I

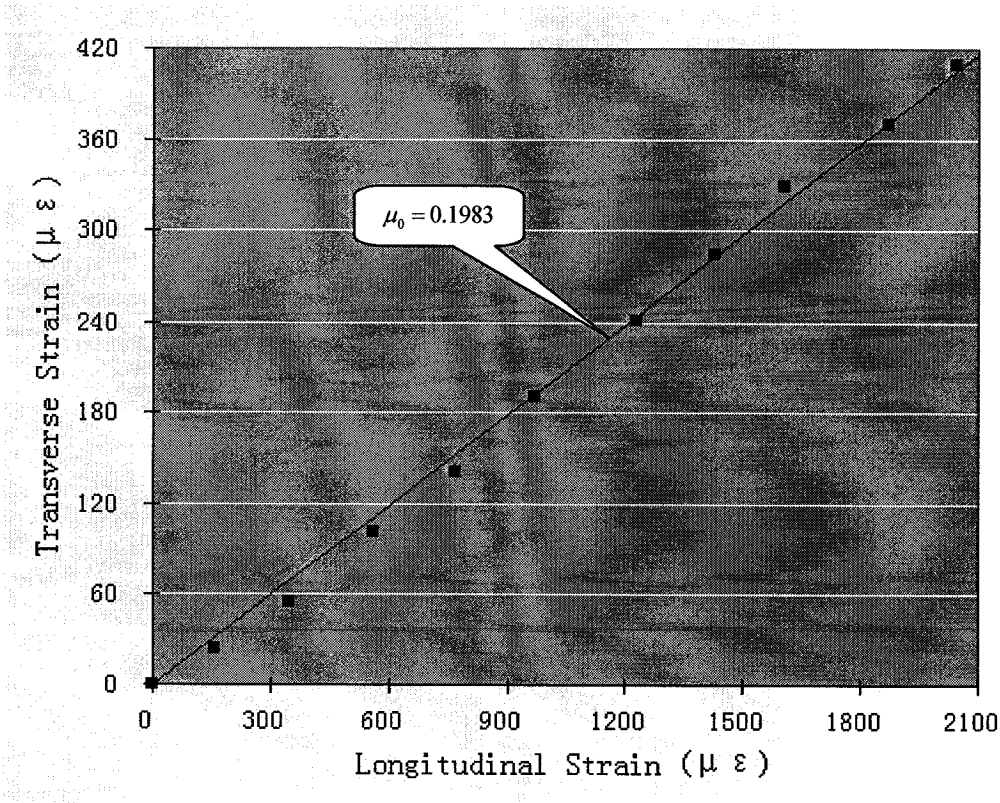

(b) Longitudinal - Transverse Strains For Specimen I

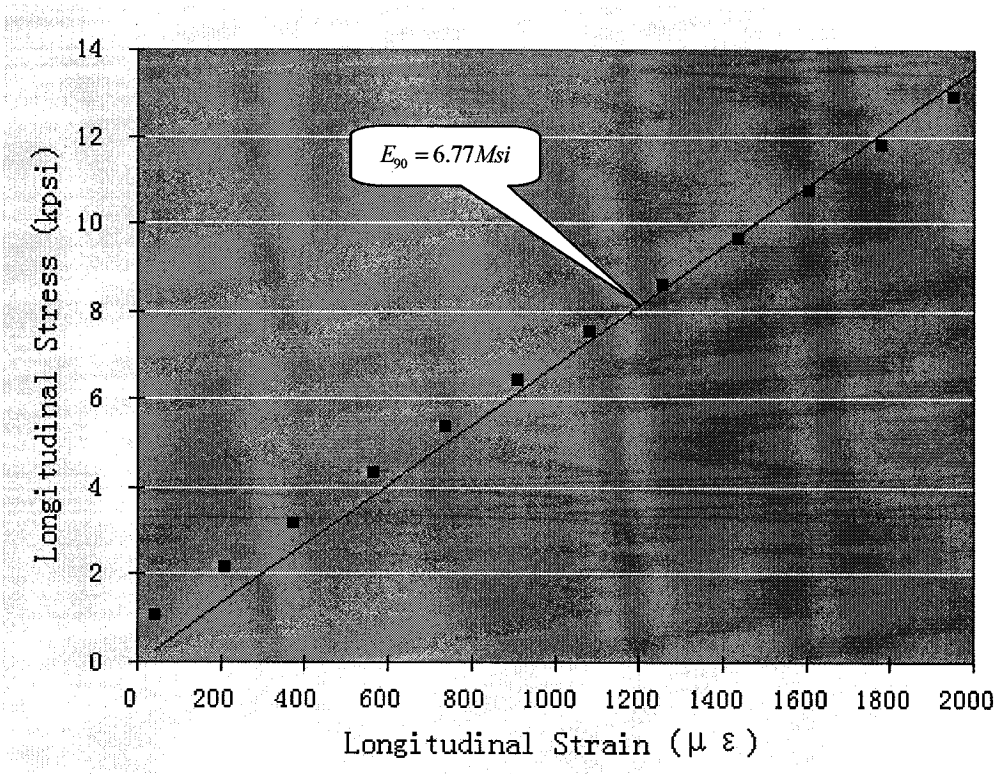

(c) Strain - Stress For Specimen II

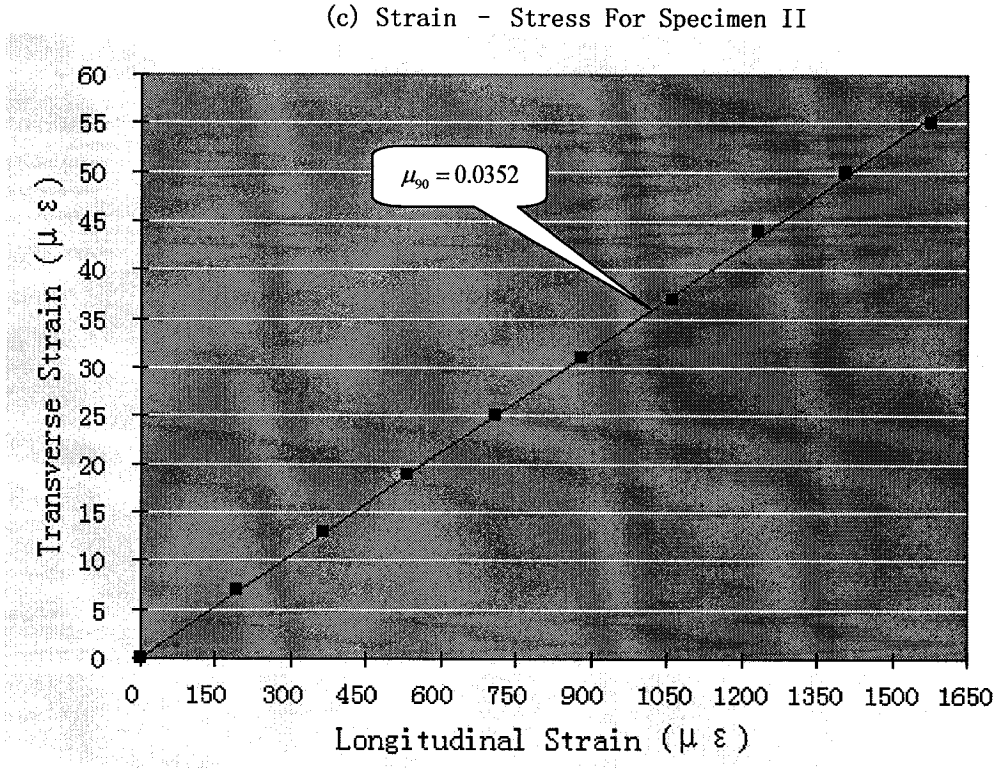

(d) Longitudinal - Transverse Strains For Specimen II

Figure 3.28 Specimens' Mechanical Behaviors

Figure 3.28 illustrates the mechanical behaviors of the two specimens during the measurement. For a linear approximation, upon Hooke's Law, as well as the criterion of Poisson's ratio:

$$\mu = \frac{\varepsilon(\mu\varepsilon)_{transverse}}{\varepsilon(\mu\varepsilon)_{lomgitudinal}} \tag{3.21}$$

where $\varepsilon_{longitudinal}$ and $\varepsilon_{transverse}$ represent structure's strain along and perpendicular to loading, respectively. One can work out for the cross-ply structure under investigation:

(1) Along 0 direction (the direction that reinforcing fibers of 16 plies are oriented), elastic modulus is approximately 12.70Msi;

(2) Along 90 direction (the direction that reinforcing fibers of 8 plies are oriented), elastic modulus is approximately 6.77Msi;

(3) Between the two in-plane principle directions of the structure, major Poisson's ratio is 0.1983, and minor Poisson's ratio is 0.0352.

(2) Embedded FBG Strain Gage's Optical Behaviors and Recalibrations

Figure 3.29 illustrates embedded FBG sensors' photoelastic behaviors when tensile stress was applied to specimens. Upon test data, one can conclude that all sensors survived and functioned well during the measurement. Although obvious deviations occurred in sensors' photoelastic responses, induced deterioration is not crucial to deny their applicability as embedded strain gages. Therefore, feasibility of designed "fiber optic smart structure" is primarily proven.

Further, recurring to surface mounted resistance strain gages, the FBG gages oriented in strain direction can be recalibrated as:

(1) In specimen I, for the FBG gage oriented in loading direction (i.e. 0 direction of the composite structure), its strain sensitivity was deviated to $\Delta\lambda_B = 1.26\times10^{-3}\varepsilon_z$;

(2) In specimen II, for the FBG gage oriented in loading direction (i.e. 90 direction of the composite structure), its strain sensitivity was deviated to $\Delta\lambda_B = 1.12\times10^{-3}\varepsilon_z$;

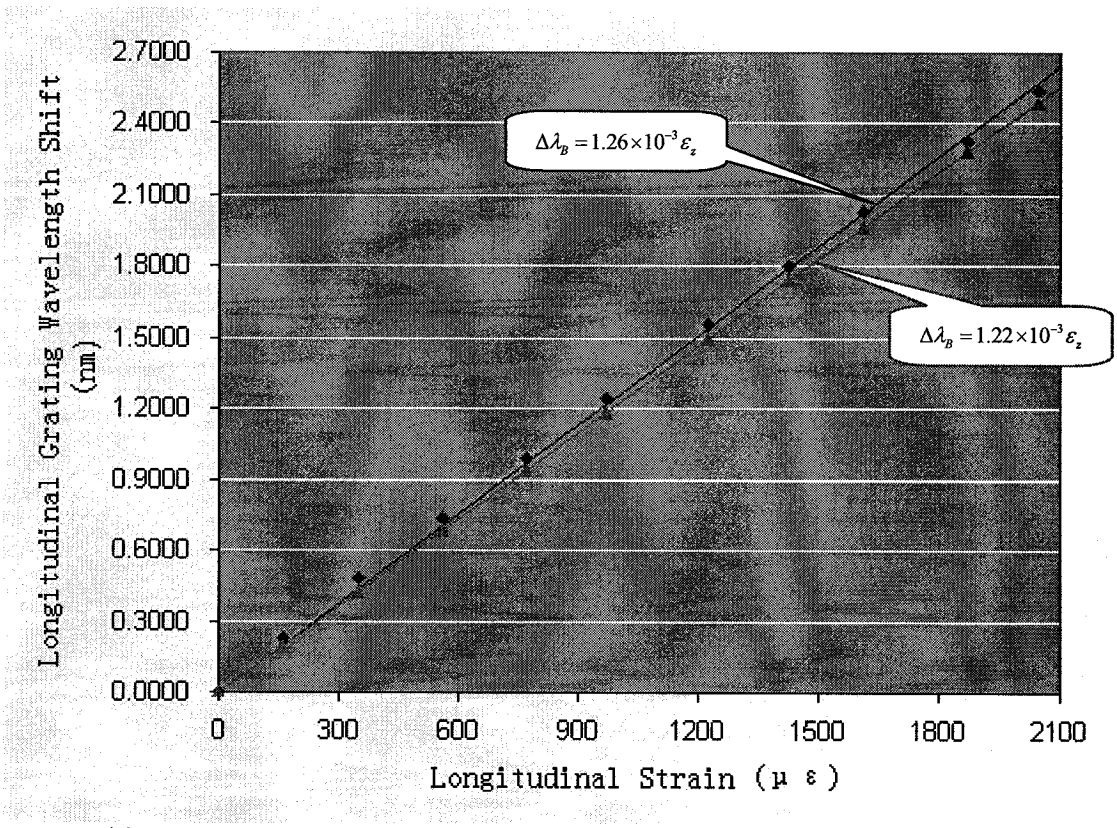

(a) FBG Sensor Along Loading Direction In Specimen I (i.e. 0 Direction)

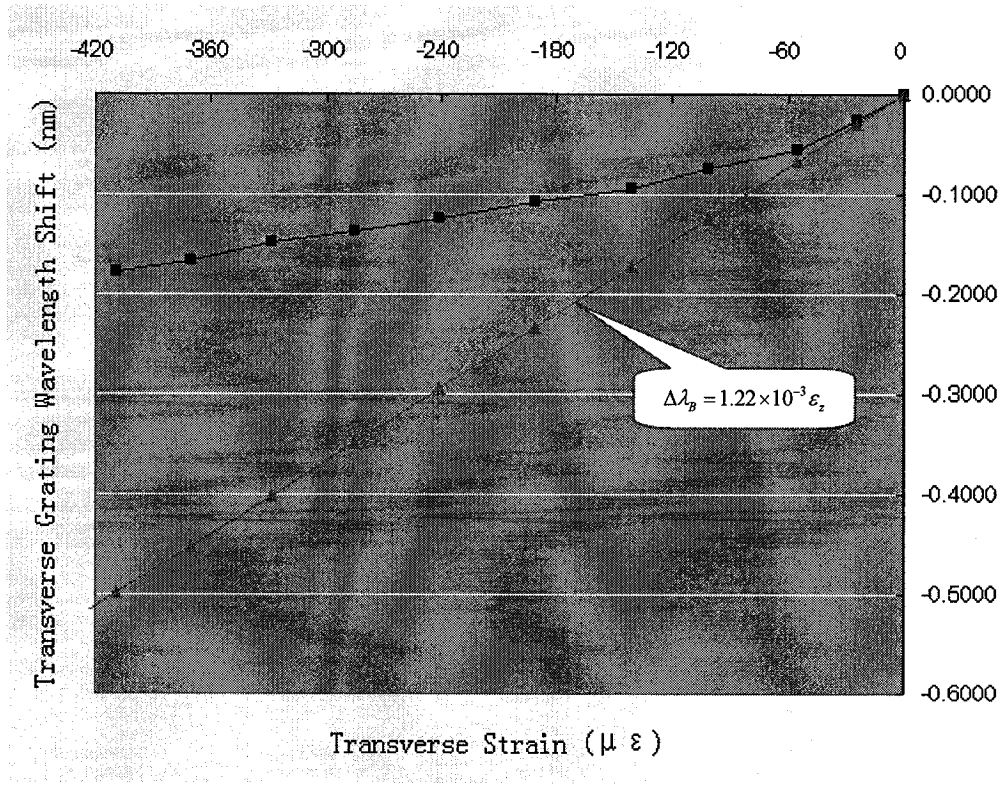

(b) FBG Sensor Perpendicular to Loading Direction In Specimen I (i.e. 0 Direction)

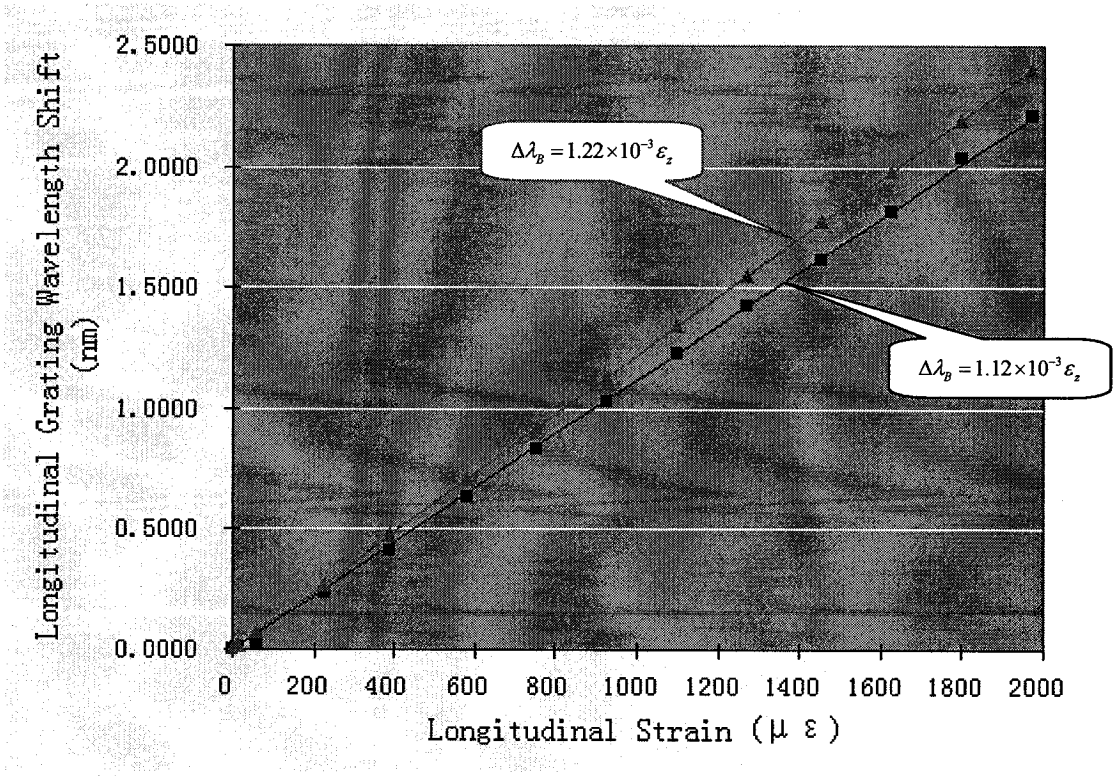

(c) FBG Sensor Along Loading Direction In Specimen II (i.e. 90 Direction)

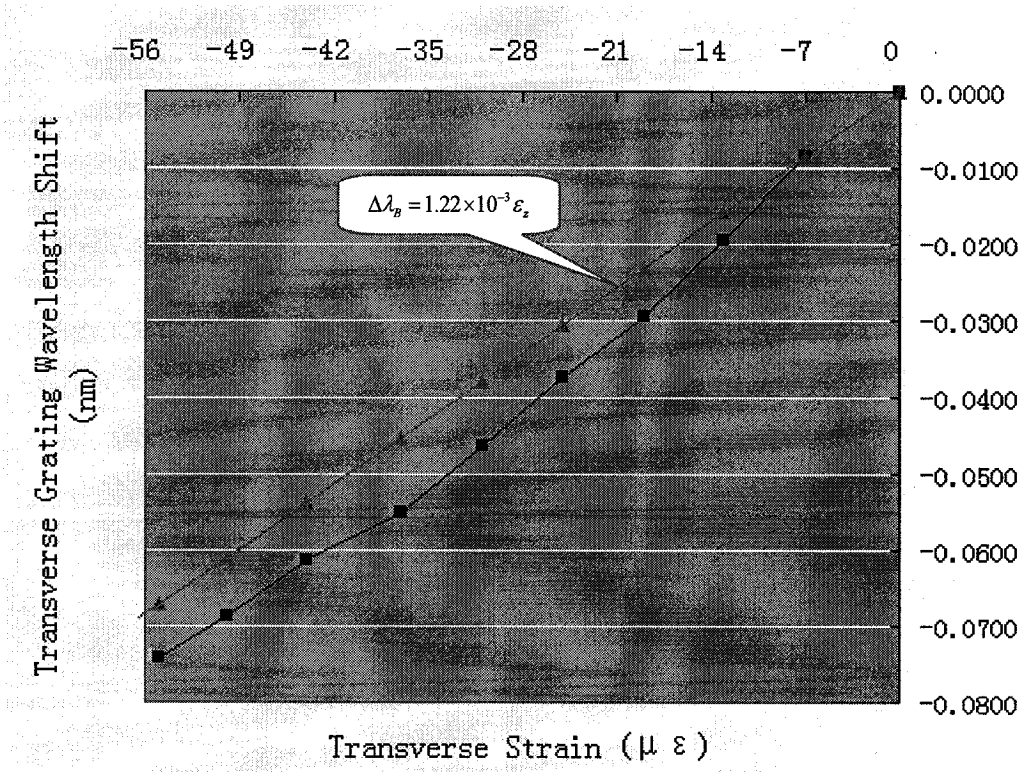

(d) FBG Sensor Perpendicular to Loading Direction In Specimen II (i.e. 0 Direction)

Figure 3.29 Embedded FBG Sensors' Photoelastic Behaviors

However, as Figure 3.29 shows, whenever FBG sensors orient perpendicular to stress, their strain-optics present somewhat unreadable manner (refer to Figure 3.29 (b) and (d)). This phenomenon will be further discussed in following section.

In addition, no grating wavelength peak split was observed in experiment, this means FBG gage's radial stress field was not that seriously non-uniform during measurement.

During the measurement, environment temperature variation was always limited within $\pm$0.5°C, which may equivalently induce $\pm$6.9pm grating wavelength uncertainty on test data.

3.3.4 Result Analysis

(1) Influence of Host Structure's Mechanical Property to Integrated FBG Sensor's Photoelastic Deviation

Consider an embedded FBG sensor, when strain is applied in host structure along the sensor, grating's photoelasticity should be able to factually reflect this ambient change. However, due to the nature of a mechanical entity, shear strain concurs in the structure perpendicular to loading and embedded sensor. Theoretically if mechanical mismatch exists between FBG fiber and surrounding material, sensor will experience additional radial stress besides axial measurand. According to equations (3.18) and (3.19), extra radial strain induces grating's axial strain-optic behavior being deviated from its bare state. Not only, one can theoretically deduce that when tensile load is applied along embedded fiber, if host structure initiated radial contraction strain is greater than FBG fiber's instinctive reaction, sensor's axial strain-optic behavior may have positive deviation apart from its bare fiber state; while if host structure initiated radial contraction strain is smaller than FBG fiber's instinctive reaction, and assume a perfect structural integrity along the fiber, sensor's axial strain-optic behavior may have negative deviation apart from its bare fiber state. Moreover, the more the mechanical mismatch between the two entities, the more the deviation occurs.

The most evident parameter to quantify the mechanical mismatch is structure's synthetic local Poisson's ratio in embedded FBG sensor's radial direction. Upon the strain-optic behavior of the FBG sensor deployed parallel with tensile load in each specimen (refer to Figure 3.29 (a) and (c)), and if assume no detachment happened between host matrix and embedded sensor in entire measurement, one may infer that:

(1) If host structure's synthetic local poisson's ratio is greater than embedded FBG fiber's intrinsic poisson's ratio in sensor's radial direction, then grating will perform positive strain-optic deviation comparing to its bare fiber state due to the induced radial compression;

(2) If host structure's synthetic local poisson's ratio is smaller than embedded FBG fiber's intrinsic poisson's ratio in sensor's radial direction, then grating will perform negative strain-optic deviation comparing to its bare fiber state due to the induced radial tension;

(2) Extent of Radial Stress Field Effect on Integrated FBG Strain Gage

It is possible to follow resistance strain gage concept to interpret the erroneous deviation due to grating's radial strain sensitivity, if temperature effect is neglected. Deriving from equations (3.18) to (3.19), synthetic behavior of an embedded FBG sensor can be generalized as [45]

$$\delta = \frac{\Delta\lambda_B}{\lambda_B} = F_z\varepsilon_z^f + F_{tx}\varepsilon_x^f + F_{ty}\varepsilon_y^f \tag{3.22}$$

where δ is the normalized grating wavelength shift; F_z is sensor's axial strain sensitivity in z direction; F_{tx} is sensor's radial strain sensitivity in x direction; and F_{ty} is sensor's radial strain sensitivity in y direction. For convenience, all sensitivities are normalized by F_z, so that equation (3.22) is transformed as

$$\delta = F_z\left(\varepsilon_z^f + K_{tx}\varepsilon_x^f + K_{ty}\varepsilon_y^f\right) \tag{3.23}$$

where K_{tx} and K_{ty} are the two normalized radial strain sensitivity factors. If one premises an "ideal" FBG strain gage, which is assumed (or more precisely, "desired") to respond

to axial strain only. It is possible to define the normalized grating wavelength shift of the "ideal" FBG strain gage as

$$\delta' = F\varepsilon_z^f \tag{3.24}$$

where superscript prime indicates an ideal gage and F is its ideal axial strain sensitivity. One may notice that this formula is equivalent to the representation of bare FBG grating. Deviations due to additional radial strains can then be quantified simply by finding the margin between actual and ideal behaviors

$$\eta = \frac{\delta - \delta'}{\delta'} \times 100\% = \left[\left(\frac{F_z}{F} - 1 \right) + \frac{F_z}{F} K_{tx} \frac{\varepsilon_x^f}{\varepsilon_z^f} + \frac{F_z}{F} K_{ty} \frac{\varepsilon_y^f}{\varepsilon_z^f} \right] \times 100\% \tag{3.25}$$

This expression reveals that FBG strain gage's deviation is a function of:

(1) Difference between actual and ideal axial sensitivity, which is believed to be induced by axial mismatch (or residual effects) between host and embedded members;

(2) Radial strain sensitivity factors, which are resulted from instinctive photoelasticity of FBG grating;

(3) Ratios $\frac{\varepsilon_x^f}{\varepsilon_z^f}$ and $\frac{\varepsilon_y^f}{\varepsilon_z^f}$, which indicate the extent of undesired radial stress during measurement.

Bringing discussed scenario into experimental result analysis, a surface mounted resistance strain gage array is geometrically superposed embedded FBG strain gage array. When specimens are pulled, considering the gages oriented along with the loading, readings from resistance strain gages are used to recalibrate corresponding FBG gages, thereby performances of actual embedded FBG strain gages are profiled. Deducting practical "axial strain – grating wavelength shift" relation by that of "ideal" bare FBG

grating (which has been obtained in the first experiment step), one can quantitatively determine the degree of the deviation.

Upon test results presented in Figure 3.29 (a) and (c), and follow the criterion discussed above, one may work out that for dedicated cross-ply structure:

(1) When tensile stress is applied along 0 direction, axial strain-optic deviation of the embedded FBG strain gage deployed coincident with the load will be:

$$\begin{aligned}\eta &= \frac{\delta - \delta'}{\delta'} \times 100\% \\ &= \frac{1.26\times10^{-3} - 1.22\times10^{-3}}{1.22\times10^{-3}} \times 100\% \\ &\approx 3.3\%\end{aligned} \tag{3.26}$$

(2) When tensile stress is applied along 90 direction, axial strain-optic deviation of the embedded FBG strain gage deployed coincident with the load will be:

$$\begin{aligned}\eta &= \frac{\delta - \delta'}{\delta'} \times 100\% \\ &= \frac{1.12\times10^{-3} - 1.22\times10^{-3}}{1.22\times10^{-3}} \times 100\% \\ &\approx -8.2\%\end{aligned} \tag{3.27}$$

Upon Figure 3.29 (a) and (c), one may illusively conclude that FBG strain gage's sensitivity is enhanced or degraded after embedment. In fact, sensor's instincts are never changed, superficial up and down of gage's strain sensitivity is induced by additional radial stresses field. This discovery also reveals the complexity in embedded FBG strain gage's interpretation.

Nevertheless, in case FBG is used as embedded strain gage, only strain tensor tangent to fiber axis is desired, while radial tensors act as noise interfering the measurand. Recurring to the concept of normal detector, only if signal is always obtrusive to noise, FBG strain gage is said to be practical, otherwise signal will be overwhelmed in noise, so

that strain gage becomes useless, or in the other word, the embedded FBG sensor would be rather used as pressure gage than strain gage upon recalibration, in which radial measurand becomes dominant. However, this work proves the feasibility of FBG strain gage network integrated in arbitrary composite structure.

Based on the discussion, precept of Signal-to-Noise Ratio (SNR) in engineering applications can be also a means to evaluate embedded FBG strain gage's usability. Hence according to test data, one can calculate SNR of individual FBG strain gage as:

(1) For the FBG strain gage oriented in 0 direction, when tensile stress is applied to the structure in the same direction, its axial – radial SNR is:

$$\begin{aligned} SNR &= 10\log\left(\left|\frac{\delta'}{\delta-\delta'}\right|\right) \\ &= 10\log\left(\left|\frac{1.22\times10^{-3}}{1.26\times10^{-3}-1.22\times10^{-3}}\right|\right) \\ &= 14.8dB \end{aligned} \tag{3.28}$$

(2) For the orthogonal one oriented in 90 direction, when tensile stress is applied to the structure in the same direction, its axial – radial SNR is:

$$\begin{aligned} SNR &= 10\log\left(\left|\frac{\delta'}{\delta-\delta'}\right|\right) \\ &= 10\log\left(\left|\frac{1.22\times10^{-3}}{1.12\times10^{-3}-1.22\times10^{-3}}\right|\right) \\ &= 10.9dB \end{aligned} \tag{3.29}$$

However, expected reflection spike split was not apparently observed in the experiment, which indicates the fact that vicinal stress field were not significantly differed along embedded fiber's circumference.

(3) FBG Sensor's Photoelastic Behavior Under Axial Compressive Strain

Figure 3.29 (b) and (d) illustrate the axial strain-optic behaviors of transversely embedded FBG strain gages in specimen I and II respectively. Unlike their longitudinal partners, these gages experienced axial compression, and presented dissimilar behaviors.

When axial compressive strain was comparatively small, sensor's strain-optic response still followed the regulation as under axial tension (refer to Figure 3.29 (d)). However, when compressive strain continued to increase, grating's strain sensitivity became remarkably degraded from the state when it was under axial tensile strain (refer to Figure 3.29 (b)).

Therefore upon observation, one may conclude that FBG sensor is not a precise gage to measure axial compression.

(4) Experimental Uncertainty

Although after using Universal Test Machine, uncertainty in characterization and recalibration of embedded FBG strain gages was significantly suppressed, there were still errors induced in measurement. Besides OSA accuracy and environmental temperature fluctuation, which were same as in bare FBG fiber measurement, UTM system's drifting was also one of the major elements inducing experimental uncertainty.

Drifting of UTM system was approximately $\pm$30pounds, which induced $\pm$12.2$\mu\varepsilon$ measurement uncertainty for specimen I when tensile stress was applied along 0 direction of the cross-ply structure, or equivalently $\pm$15.4pm for the corresponding FBG strain gage; and $\pm$23.8$\mu\varepsilon$ measurement uncertainty for specimen II when tensile stress was applied along 90 direction of the cross-ply structure, or equivalently $\pm$26.7pm for the corresponding FBG strain gage.

Meanwhile, although utmost effort has been made to coincide embedded FBG strain gages and surface mounted resistance strain gages during specimens' fabrications, man-made errors may still be induced in two corresponding gages' alignment, hence led to unneglectable uncertainties in the experimental results.

One more component need to be mentioned in considering experimental uncertainty is, due to the WDM (Wavelength Division Multiplexing) mechanism in sensor networking, initial grating wavelengths involved in FBG array have to be always different from 1550nm, which was the initial grating wavelength of the bare FBG fiber tested in the first experimental step, and used to determine erroneous deviations of embedded FBG strain gages. Upon previous discussion, sensor's strain-optic behavior relies also on initial grating wavelength, hence additional errors are induced in the discussion. However, to some extent (e.g. in the wavelength range from 1545nm to 1555nm), the deterioration is imperceptible.

CHAPTER IV

CONCLUSIONS AND SUGGESTIONS

Through the experiment, suspensions are effectively answered regarding FBG strain gages' applicability integrated in Graphite/Epoxy composite material, as well as the feasibility of realizing a " fiber optic smart structure", i.e.

(1) With appropriate treatment (e.g. follow the optimal layout criteria and the proper way of optical fiber ingress/egress, etc.), FBG sensors can always survive and function properly throughout composite fabrication and designated strain measurement. Further, optimized layout scheme of sensor array embedment can remarkably reduce the disturbance to both FBG's sensitivity and host structure's mechanical properties.

(2) Even though FBG fibers are deployed in conformity to optimal layout scheme, due to embedment induced local continuum perturbation, as well as host structure's natural transverse reaction when stress is applied to the entity along sensor's direction, apparent radial stress field is still induced surrounding embedded sensor, hence leads to erroneous deviation to FBG strain gage's performance, which may deteriorate gage's accuracy, and complicate measurand interpretation. However, to certain extent, embedded strain gages can be still usable upon proper recalibration, and these additional radial noise tensors are comparatively small in magnitude.

Moreover, one can draw conclusions for individual experimental step separately.

4.1 Conclusions For Step 1 – Photoelasticity of Bare FBG Fiber

(1) Due to the photoelastic nature, FBG sensor's grating wavelength shift is regressively linear along with its axial strain. Considering the bare FBG fibers used in the experiment, in the range of 1550nm, its strain sensitivity can be expressed as

$$\lambda_B \approx 1.2\times10^{-3}\varepsilon_z + \lambda_0 \quad (4.1)$$

where ε_z is the applied axial strain in με, λ_B is the shifted grating wavelength, and λ_0 is the initial grating wavelength when there is no strain applied. Therefore one can anticipate approximately 1.2pm grating wavelength increase as a result of axially applying 1 με strain to bare FBG fiber.

(2) During FBG inscription, physical micro-structure of the fiber is degraded, thus grating section is always mechanically weaker comparing to normal optical fibers, therefore tensile strength for normal optical fibers cannot be used to characterize FBG fibers. In order to justify FBG sensor's applicable range, a set of tensile strength verification is always demanded.

4.2 Conclusions For Step 2 - Fabrication of FBG Array Embedded Composite Structure

In the experiment, FBG sensor array embedded Graphite/Epoxy composite specimens were fabricated. Although experienced high pressure (up to 60psi) and high temperature (up to 145°C) curing cycle for more than two hours, embedded FBG sensors were still functional at the end of the fabrication process. Therefore embedded FBG sensor's survivability and potential applicability were proven upon proper treatment, including the determination of sensor's embedment location and orientation, choice of coating types, control of prepreg preparation and curing cycle, and the way of optical fiber ingress/egress protection.

(1) Before real fabrication, different sensor array layout schemes were carried out and outcomes were observed. According to the investigation, optimal layout criterion was proposed with minimized degradation to both host structure and FBG sensor's

performances, i.e. if possible, designers have to make the best to deploy FBG fiber's gauge length parallel to its neighboring reinforcing fibers; as well, FBG fibers have to be buried at least four layers away from the outer surface or the interface between cross-plies.

(2) Upon observation, Polyimide was proven to be the nominated coating material for embedded FBG sensors based on its enhanced high temperature tolerance, thus results in better bonding to neighboring resins after curing. Moreover, Polyimide coated FBG fibers characterize smaller diameter, consequently induce less mechanical perturbation to vicinal continuum.

(3) Due to thermal expansion mismatch between optical fiber and host material, residual stress was observed in terms of FBG sensor's grating wavelength shift after curing process, although magnitude of the shifting depends on the extent of mismatch (i.e. different thermal expansion coefficients of involved materials), the way of FBG fiber layout, and different fabrication process. This residual effect can be zeroed out in strain measurement.

(4) It was observed embedded FBG sensors' reflectivity was reduced after composite curing. This phenomenon is supposed to limit the deployment scale of potential sensing network, where large number of sensors is desired to multiplex in series along optical fiber, due to the fact that ambience encoded wavelength notches or spikes become weaker. In case one wants to keep the reflectivity unchanged or minimize the weakening after curing, pre-annealing on FBG fibers is required before embedment.

4.3 Conclusions For Step 3 - Investigation and Calibration of Embedded FBG Strain Gage Array

After embedment, FBG array's phtoelastic behaviors were monitored when strains were applied on specimens. Throughout desired measurement ranges, neither fraction nor debonding was observed, hence sensors are proven to be practical in embedment applications. Further,

(1) In the experiment, surface mounted resistance strain gages were used to characterize corresponding embedded FBG sensors, hence embedded FBG strain gages were recalibrated.

(2) Upon recalibrated behaviors, embedded FBG strain gages' erroneous deviations were quantitatively discussed. It is concluded that these deviations are induced by FBG grating's radial strain sensitivities to transverse stress field surrounding the fiber. Further, Signal-To-Noise Ratio (SNR) concept is introduced to evaluate the applicability of an embedded FBG strain gage. However, through the experiment, it is proven that under dedicated situations, embedded FBG strain gages are always usable upon proper recalibration, and additional radial noise tensors are comparatively small in magnitude.

(3) Investigations have also been made in relating host structure's mechanical properties and embedded FBG sensor's axial strain-optic deviation. It was discovered that host structure's transverse local Poisson's ratio presents qualitative effect on determining longitudinally deployed FBG sensor's axial strain-optic deviation.

(4) It was also discovered FBG sensor performs degraded photoelastic behavior under axial compressive strain.

Moreover, Experimental uncertainties were discussed for individual steps.

4.4 Suggestions for Further Works

(1) Dynamic Interrogation of Embedded FBG Sensor's Performance

Although after UTM (Universal Test Machine) system was utilized in the experiment, measurement uncertainties were effectively suppressed and embedded FBG sensor's characterization and recalibration became more reliable, limitations still exist due to the manually operated equipment.

It is believed the best solution is to establish a dynamic optical interrogation mechanism to cooperate with automatic material test facility, so that both sensor's photoelasticity and specimen's mechanical properties can be automatically obtained.

(2) Analytical Measurement of Randomly Oriented In-Plane Strain With Embedded Orthogonal FBG Strain Gage Array

According to the designed scheme of "fiber optic smart structure", orthogonal FBG sensor array are always deployed along two in-plane principle coordinates of the composite structure. In the experiment, performances of embedded FBG strain gage array were studied only when tensile stress was applied along one of the two FBG fibers' directions (i.e. one of host structure's two in-plane principle coordinates). However, in practice, material has to always experience randomly oriented in-plane stress, thus FBG array's responses under more complicated stress state need to be studied. And it can be expected further strain-optic deviation will occur for embedded sensors.

(3) Embedded FBG Sensor's Photoelastic Behavior Under Radial Pressure

Upon the three-dimensional photoelastic nature, FBG grating is a promising candidate to measure either axial strain, or radial pressure, or both. Whenever the sensor

is used as strain gage, radial responses will act as interferential components additional to desired axial measurand. Notwithstanding, attributes of signal and noise may sometimes be inverted, specially when the sensor is used as pressure gage.

In order to thoroughly understand and factually interpret FBG sensor's synthetic behavior, deeper study on grating's radial sensitivity is needed.

REFERENCES

[1] P.J. Henderson, D.J. Webb, D.A. Jackson, L. Zhang, I. Bennion, "Highly-Multiplexed Grating Sensors For Temperature-Referenced Quasi-Static Measurements of Strain in Concrete Bridges", Proc. SPIE, Vol. 3746, 320 – 323, 1999

[2] G.J. Tsamasphyros, G.N. Kenderakis, N.K. Furnarakis, Z.P. M. Riga, R. Chemama, R. Bartolo, "Selection of Optical Fiber Paths and Sensor Locations for Monitoring The Integrity of Composite Patching", Applied Composite Materials, 10: 331 – 338, 2003

[3] J.P. Dakin, M. Volanthen, "Distributed and Multiplexed Fiber Grating Sensors, Including Discussion of Problem Areas", IEICE Trans. Electron. E83 – C (3), 391 – 199, 2000

[4] K.T.V Grattan, B.T. Meggitt, "Optical Fiber Sensor Technology: Fundamentals", Kluwer Academic Publishers, 2000

[5] M. Zhang, C.C. Chan, D.N. Wang, J.M. Gong, W. Jin, M.S. Demokan, "Time division multiplexed strain sensing system by the use of dual-wavelength fiber Bragg gratings", Sensors and Actuators A, 100, 175 – 179, 2002

[6] B. Lee, "Review of The Present Status of Optical Fiber Sensors", Optical Fiber Technology, 9, 57 – 79, 2003

[7] K.O. Hill, Y. Fujii, D.C. Johnson, B.S. Kawasaki, "Photosensitivity in Optical Fiber Waveguides: Application to Reflection Filter Fabrication", Applied Physics Letters, 32, 647 – 649, 1978

[8] G. Meltz, W.W. Morey, W.H. Glenn, "Formation of Bragg Gratings in Optical Fibers by A Transverse Holographic Methos", Optics Letters, 14, 823 – 825, 1989

[9] A. Othonos, "Fiber Bragg Gratings", Review of Scientific Instruments, 68 (12), 4309 – 4341, December 1997

[10] R. Kashyap, "Photosensitive Optical Fibers: Devices and Applications", Optical Fiber Technology, 1, 17 – 34, 1994

[11] A. Otghonos, K. Kalli, "Fiber Bragg Gratings, Fundamentals and Applications in Telecommunications and Sensing", Artech House, 1999

[12] S.M. Melle, K. Liu, R.M. Measures, "Practical Fiber-Optic Bragg Grating Strain Gauge System", Applied Optics, Vol. 32, No. 19, 3601 – 3609, July 1993

[13] A.D. Kersey, M.A. Davis, H.J. Patrick, M. LeBlanc, K.P. Koo, C.G. Askins, M.A. Putnam, E.J. Friebele, "Fiber Grating Sensors", Journal of Lightwave Technology, Vol. 15, No. 8, August 1997

[14] R. Kashyap, J.M. Lopéz-Higuera, "Handbook of Optical Fiber Sensing Technology, Chapter 17: Fiber Grating Technology: Theory, Photosensitivity, Fabrication and Characterization", edited by J.M. Lopéz-Higuera, John Wiley & Sons, Ltd., 2002

[15] V. Karbhari, F. Seible, "Fiber Reinforced Composites – Advanced Materials for the Renewal of Civil Infrastructure", Applied Composite Materials, 7, 95 – 124, 2000

[16] J.S. Hansen, " Fiber Optical Smart Structures, Chapter 3: Introduction to Advanced Composite Materials", Edited by E. Udd, John Wiley & Sons Inc., 1994

[17] E. Udd, "Fiber Optic Smart Structures, Chapter 2: Fiber Optic Smart Structure Technology", Edited by E. Udd, John Wiley & Sons Inc., 1994

[18] L. Tang, X. Tao, C.L. Choy, "Effectiveness and optimization of fiber Bragg grating sensor as embedded strain sensor", Smart Materials and Structures, 8, 154 – 160, 1999

[19] J.S. Sirkis, A. Dasgupta, "Fiber Optic Smart Structures: Chapter 4, Optical Fiber/Composite Interaction Mechanics", Edited by E. Udd, John Wiley & Sons, Inc., 1994

[20] Y. Wan, "Analytical Micromechanics of Optical Fiber Sensors Embedded in Laminated Composites", M.S. Thesis, Mechanical Eng. Dept., University of Maryland College Park, MD, 1990

[21] R. Davidson, S.S.J. Roberts, "Do Embedded Sensor Systems Degrade Mechanical Performance of Host Composite?", ADPA/AIAA/ASME/SPIE conference on active mechanicals and adaptive structures – session 7, 1992

[22] Y. Okabe, N. Tanaka, N. Takeda, "Effect of fiber coating on crack detection in carbon fiber reinforced plastic composites using fiber Bragg grating sensors", Smart Materials and Structures, 11, 892 – 898, 2002

[23] "Corning® SMF-28e™ Photonic Fiber Product Information," Corning Incorporated, 2003

[24] G. Mahlke, P. Gössing, " Optical Fiber Cables, Fundamentals Cable Engineering Systems Planning", Siemens Aktiengesellschaft, 1993

[25] "The Importance of Fiber Geometry", Corning Fiber News & Views, Dec. 1999

[26] "Technical Specification for FBG Fibers", Bragg Photonics Inc., 2003

[27] M. Runger, "Applied Statistics and Probability for Engineers", 3rd edition, John Wiley & Sons, Inc., 2003

[28] J. Lawson, "Modern Statistics for Engineering and Quality Improvement, Chapter 10: Regression Analysis", Duxbury, 2000

[29] "AQ-6319 Optical Spectrum Analyzer Operation Manual", Ando Electric Co. Ltd., 2003

[30] S.O. Kasap, "Optoelectronics And Photonics: Principles And Practices", Prentice Hall, 2001

[31] W.B. Spillman Jr., Jeffery R. Lord, "Fiber Optic Smart Structures: Chapter 6, Methods of Fiber Optic Ingress/Egress for Smart Structures", Edited by E. Udd, John Wiley & Sons, Inc., 1994

[32] "NCT-301 Product Data Sheet", Newport Adhesive s and Composites, Inc., 2003

[33] G. Dick, M. LeBlanc, "Arbitrary Strain Transfer From A Host to An Embedded Fiber-Optic Sensor", Smart Materials and Structures, 9, 492 – 497, 2000

[34] R. Davidson, D.H.Bowen, S.S.J. Roberts, "Composite Materials Monitoring Through Embedded Fiber Optics", Int., J. Optoelectron. 5(5), 397 – 404, 1990

[35] A. Tay, D.A. Wilson, L. Wood, "Strain Analysis of Optical Fibers Embedded in Composite Materials Using Finite Element Modeling", Proc. SPIE – Int. Soc. Opt. Eng., 1170, 521 – 533, 1990

[36] A. Dasgupta, Y. Wan, J.S. Sirkis, " Prediction of Resin-Pocket Geometry for Stress Analysis of Optical Fibers Embedded in Laminated Composites", Smart Materials and Structures, Vol. 1, No. 3, pp. 101 – 107, 1992

[37] G.P. Carman, R.C. Averill, K.L. Reifsnider, J.L. Reddy, "Optimization of Coatings to Minimize Micromechanical Stress Concentrations in Composites", Journal of Composite Materials, 27(6), 589 – 613, 1993

[38] H.K. Kang, D.H. Kang, H.J. Bang, C.S. Hong, C.G. Kim , "Cure Monitoring of Composite Laminates Using Fiber Optic Sensors", Smart Materials and Structures, 11, 279 – 287, 2002

[39] V.M. Murukeshan, P.Y. Chan, L.S. Ong, L.K. Seah, "Cure Monitoring of Smart Composites Using Fiber Bragg Grating Based Embedded Sensors", Sensors and Actuators, 79, 153 – 161, 2000

[40] B. Zhang, D. Wang, S. Du, Y. Song, "An Investigation of A Fiber Optic Sensor In The Composite Cure Process", Smart Materials and Structures, 8, 515 – 518, 1999

[41] R.M. Atkins, V. Mizrahi, "Observations of Changes in UV Absorption Bands of Single Mode Germanosilicate Core optical Fibers on Writing and Thermal Erasing Refractive Index Gratings", Electronics Letters, Vol. 28, 1743 – 1744, 1992

[42] J.S. Sirkis, "A Unified Approach to Phase-Strain-Temperature Models For Smart Structure Interferometric Optical Fiber Sensors", Optical Engineering, 32(4), 752 – 773, 1993

[43] F. Bosia, P. Giaccari, J. Botsis, M. Facchini, H.G. Limberger, R.P. Salathé, "Characterization of The Response of Fiber Bragg Grating Sensors Subjected to A Two-Dimensional Strain Field", Smart Materials and Structures, 12, 925 – 934, 2003

[44] I. Granet, "Strength of Materials for Engineering Technology, 2nd Edition", Reston Publishing Company Inc., 1980

[45] J.W. Dally, W.F. Riley, "Experimental Stress Analysis", 3rd Edition, McGraw – Hill, 1991

[46] R. Gafsi, M.A. El-Sherif, "Analysis of Induced-Birefringence Effects on Fiber Bragg Gratings", Optical Fiber Technology, 6, 299 – 323, 2000

[47] J.F. Nye, "Physical Properties of Crystals", Chapter 13 and 14, Clarendon, Oxford

Publication Contributions:

[1] Y. Fan, M. Kahrizi, "An Optical MEMS Sensor System", CCECE 2003, Montreal

[2] Y. Fan, M. Kahrizi, "Applicability of An Optimized Fiber Optic Smart Structure", ICMENS 2004, Calgary (to be published)

APPENDIX

Birefringent Photoelasticity of Fiber Bragg Grating [46]

Refractive index changes induced by applied stress are called photoelastic phenomena. It is assumed at any cross section along its optical axis, FBG is an isotropic medium with low intrinsic birefringence. The core and the cladding of optical fiber are supposed to be the same with identical photoelastic and mechanical properties but different refractive indices. These hypotheses are valid for standard all-silica fibers. It is also assumed that manufacturing and grating writing operations do not affect the physical and mechanical properties of optical fiber.

The refractive index tensor of FBG fiber expressed in arbitary Cartesian coordinate is given by

$$[n]=\begin{bmatrix} n_{11} & n_{12} & n_{13} \\ n_{12} & n_{22} & n_{23} \\ n_{13} & n_{23} & n_{33} \end{bmatrix} \tag{5.1}$$

The impermeability tensor is given by

$$[B]=\begin{bmatrix} B_{11} & B_{12} & B_{13} \\ B_{12} & B_{22} & B_{23} \\ B_{13} & B_{23} & B_{33} \end{bmatrix}=\begin{bmatrix} \frac{1}{n_{11}^2} & \frac{1}{n_{12}^2} & \frac{1}{n_{13}^2} \\ \frac{1}{n_{12}^2} & \frac{1}{n_{22}^2} & \frac{1}{n_{23}^2} \\ \frac{1}{n_{13}^2} & \frac{1}{n_{23}^2} & \frac{1}{n_{33}^2} \end{bmatrix} \tag{5.2}$$

where

$$B_{ij}=\frac{1}{n_{ij}^2} \qquad (i,j=1,2,3)$$

The refractive index changes due to photoelastic effect and developed to the first order are given by

$$\Delta\left(\frac{1}{n_{ij}^2}\right)=\Delta\left(B_{ij}\right)=p_{ijkl}\varepsilon_{kl} \tag{5.3}$$

where p_{ijkl} is a fourth-rank tensor giving the photoelastic effect.

The photoelastic tensor for an isotropic material expressed in a Cartesian coordinate system (x,y,z) is

$$p_{mn}=\begin{bmatrix} p_{11} & p_{12} & p_{12} & 0 & 0 & 0 \\ p_{12} & p_{11} & p_{12} & 0 & 0 & 0 \\ p_{12} & p_{12} & p_{11} & 0 & 0 & 0 \\ 0 & 0 & 0 & \dfrac{(p_{11}-p_{12})}{2} & 0 & 0 \\ 0 & 0 & 0 & 0 & \dfrac{(p_{11}-p_{12})}{2} & 0 \\ 0 & 0 & 0 & 0 & 0 & \dfrac{(p_{11}-p_{12})}{2} \end{bmatrix} \tag{5.4}$$

The strain tensor ε_{kl} is a second-rank tensor given by

$$[\varepsilon]=\begin{bmatrix} \varepsilon_{11} & \varepsilon_{12} & \varepsilon_{13} \\ \varepsilon_{12} & \varepsilon_{22} & \varepsilon_{23} \\ \varepsilon_{13} & \varepsilon_{23} & \varepsilon_{33} \end{bmatrix} \tag{5.5}$$

Because photoelastic tensor is expressed as a 6×6 matrix, strain must be presented with 6×1 column vector. By using Nye's notation [47], equation (5.3) can be transformed to notation

$$\Delta\left(\frac{1}{n_m^2}\right)=\Delta\left(B_m\right)=p_{mn}\varepsilon_n \qquad (m,n=1,2,3,4,5,6) \tag{5.6}$$

Using these notations, refractive index and strain tensors become

$$[n]=\begin{bmatrix} n_1 & n_6 & n_5 \\ n_6 & n_2 & n_4 \\ n_5 & n_4 & n_3 \end{bmatrix} \tag{5.7}$$

and

$$[\varepsilon]=\begin{bmatrix} \varepsilon_1 & \frac{1}{2}\varepsilon_6 & \frac{1}{2}\varepsilon_5 \\ \frac{1}{2}\varepsilon_6 & \varepsilon_2 & \frac{1}{2}\varepsilon_4 \\ \frac{1}{2}\varepsilon_5 & \frac{1}{2}\varepsilon_4 & \varepsilon_3 \end{bmatrix} \tag{5.8}$$

Then equation (5.3) will be written as

$$\begin{bmatrix} \Delta\left(\frac{1}{n_1^2}\right) \\ \Delta\left(\frac{1}{n_2^2}\right) \\ \Delta\left(\frac{1}{n_3^2}\right) \\ \Delta\left(\frac{1}{n_4^2}\right) \\ \Delta\left(\frac{1}{n_5^2}\right) \\ \Delta\left(\frac{1}{n_6^2}\right) \end{bmatrix} = \begin{bmatrix} p_{11} & p_{12} & p_{12} & 0 & 0 & 0 \\ p_{12} & p_{11} & p_{12} & 0 & 0 & 0 \\ p_{12} & p_{12} & p_{11} & 0 & 0 & 0 \\ 0 & 0 & 0 & \frac{(p_{11}-p_{12})}{2} & 0 & 0 \\ 0 & 0 & 0 & 0 & \frac{(p_{11}-p_{12})}{2} & 0 \\ 0 & 0 & 0 & 0 & 0 & \frac{(p_{11}-p_{12})}{2} \end{bmatrix} \times \begin{bmatrix} \varepsilon_1 \\ \varepsilon_2 \\ \varepsilon_3 \\ \varepsilon_4 \\ \varepsilon_5 \\ \varepsilon_6 \end{bmatrix} \tag{5.9}$$

Then refractive index changes developed to the first order are

$$\begin{aligned} \Delta\left(\frac{1}{n_1^2}\right) &= -2\frac{\Delta n_1}{n_1^3} = p_{11}\varepsilon_1 + p_{12}(\varepsilon_2+\varepsilon_3) \\ \Delta\left(\frac{1}{n_2^2}\right) &= -2\frac{\Delta n_2}{n_2^3} = p_{11}\varepsilon_2 + p_{12}(\varepsilon_1+\varepsilon_3) \\ \Delta\left(\frac{1}{n_3^2}\right) &= -2\frac{\Delta n_3}{n_3^3} = p_{11}\varepsilon_3 + p_{12}(\varepsilon_1+\varepsilon_2) \\ \Delta\left(\frac{1}{n_4^2}\right) &= -2\frac{\Delta n_4}{n_4^3} = \frac{(p_{11}-p_{12})}{2}\varepsilon_4 \\ \Delta\left(\frac{1}{n_5^2}\right) &= -2\frac{\Delta n_5}{n_5^3} = \frac{(p_{11}-p_{12})}{2}\varepsilon_5 \end{aligned} \tag{5.10}$$

$$\Delta\left(\frac{1}{n_6^2}\right) = -2\frac{\Delta n_6}{n_6^3} = \frac{(p_{11}-p_{12})}{2}\varepsilon_6$$

The stress – strain relationship is given by

$$\begin{aligned}
\varepsilon_x &= \frac{1}{E}\left[S_x - \mu\left(S_y + S_z\right)\right] \\
\varepsilon_y &= \frac{1}{E}\left[S_y - \mu\left(S_x + S_z\right)\right] \\
\varepsilon_z &= \frac{1}{E}\left[S_z - \mu\left(S_x + S_y\right)\right] \\
\varepsilon_{yz} &= \frac{2(1+\mu)}{E}S_{yz} = S_{yz}G^{-1} \\
\varepsilon_{xz} &= \frac{2(1+\mu)}{E}S_{xz} = S_{xz}G^{-1} \\
\varepsilon_{xy} &= \frac{2(1+\mu)}{E}S_{xy} = S_{xy}G^{-1}
\end{aligned} \tag{5.11}$$

where E and μ are respectively the Young's modulus and Poisson's ratio of optic fiber; G is the rigidity and is given by $G = E/2(1+\mu)$; S_x, S_y and S_z are the stress components at point (x,y,z) in optical fiber along x, y and z directions respectively, and S_{xy}, S_{yz} and S_{xz} are respectively the shear stress components at point (x,y,z) in optic fiber along x, y and z directions. Similarly, ε_x, ε_y and ε_z are the strain components at point (x,y,z) in optical fiber along x, y and z directions respectively, and $\varepsilon_{xy}, \varepsilon_{yz}$ and ε_{xz} are respectively the shear strain components at point (x,y,z) in optic fiber along x, y and z directions. There it is preferred to use alphabetic representation rather than numeric indices.

By using stress – strain relationship, i.e. equation (5.11), refractive index changes are given as:

$$\Delta n_x(x,y,z) = -\frac{n_1^3}{2E}\left\{(p_{11}-2\mu p_{12})S_x(x,y,z)+\left[(1-\mu)p_{12}-\mu p_{11}\right]\left[S_y(x,y,z)+S_z(x,y,z)\right]\right\}$$

$$\Delta n_y(x,y,z) = -\frac{n_2^3}{2E}\left\{(p_{11}-2\mu p_{12})S_y(x,y,z)+\left[(1-\mu)p_{12}-\mu p_{11}\right]\left[S_x(x,y,z)+S_z(x,y,z)\right]\right\}$$

$$\Delta n_z(x,y,z) = -\frac{n_3^3}{2E}\left\{(p_{11}-2\mu p_{12})S_z(x,y,z)+\left[(1-\mu)p_{12}-\mu p_{11}\right]\left[S_x(x,y,z)+S_y(x,y,z)\right]\right\}$$

$$\Delta n_{yz}(x,y,z) = -\frac{n_4^3}{2E}(p_{11}-p_{12})(1+\mu)S_{yz}(x,y,z)$$

$$\Delta n_{xz}(x,y,z) = -\frac{n_5^3}{2E}(p_{11}-p_{12})(1+\mu)S_{xz}(x,y,z)$$

$$\Delta n_{xy}(x,y,z) = -\frac{n_6^3}{2E}(p_{11}-p_{12})(1+\mu)S_{xy}(x,y,z) \tag{5.12}$$

Therefore, refractive index changes at any point $M(x,y,z)$ in FBG's grating zone and developed to the first-order are given by following formulae:

For x-polarization,

$$\begin{aligned}\left(\Delta n_{eff}\right)_x(x,y,z) = -\frac{\left(n_{eff,0}\right)^3}{2E}\times\{\ &(p_{11}-2\mu p_{12})S_x(x,y,z)\\ &+\left[(1-\mu)p_{12}-\mu p_{11}\right]\times\left[S_y(x,y,z)+S_z(x,y,z)\right]\ \}\end{aligned} \tag{5.13}$$

For y-polarization,

$$\begin{aligned}\left(\Delta n_{eff}\right)_y(x,y,z) = -\frac{\left(n_{eff,0}\right)^3}{2E}\times\{\ &(p_{11}-2\mu p_{12})S_y(x,y,z)\\ &+\left[(1-\mu)p_{12}-\mu p_{11}\right]\times\left[S_x(x,y,z)+S_z(x,y,z)\right]\ \}\end{aligned} \tag{5.14}$$

where $n_{eff,0}$ is the intrinsic effective refractive index of the core of undisturbed FBG grating.

On the other hand, when FBG is subject to external load F and temperature variation T, its grating wavelength shift is given by

$$d\lambda_B = \left[2\Lambda_{B,0} \left(\frac{\partial n_{eff}}{\partial F} \right)_{T=c^{te}} + 2n_{eff,0} \left(\frac{\partial \Lambda_B}{\partial F} \right)_{T=c^{te}} \right] dF + \left[2\Lambda_{B,0} \left(\frac{\partial n_{eff}}{\partial T} \right)_{F=c^{te}} + 2n_{eff,0} \left(\frac{\partial \Lambda_B}{\partial T} \right)_{F=c^{te}} \right] dT \tag{5.15}$$

If consider isothermal condition ($T = c^{te}$) and the thermal expansion of FBG fiber is negligible compared to load effect, equation (5.15) can be reduced to

$$d\lambda_B = \left[2\Lambda_{B,0} \left(\frac{\partial n_{eff}}{\partial F} \right)_{T=c^{te}} + 2n_{eff,0} \left(\frac{\partial \Lambda_B}{\partial F} \right)_{T=c^{te}} \right] dF \tag{5.16}$$

Using equation (5.13) and (5.14), one can derive through equation (5.16) that grating wavelength shift at any point of the disturbed FBG is given by:

For x-polarization,

$$\begin{aligned} (\Delta\lambda_B)_x (x,y,z) = & -\frac{(n_{eff,0})^3 \Lambda_{B,0}}{E} \\ & \times \{ (p_{11} - 2\mu p_{12}) S_x (x,y,z) \\ & + [(1-\mu) p_{12} - \mu p_{11}] \times [S_y (x,y,z) + S_z (x,y,z)] \} \\ & + \frac{2n_{eff,0}\Lambda_{B,0}}{E} \times \{ S_z (x,y,z) - \mu [S_x (x,y,z) + S_y (x,y,z)] \} \end{aligned} \tag{5.17}$$

For y-polarization,

$$\begin{aligned} (\Delta\lambda_B)_y (x,y,z) = & -\frac{(n_{eff,0})^3 \Lambda_{B,0}}{E} \\ & \times \{ (p_{11} - 2\mu p_{12}) S_y (x,y,z) \\ & + [(1-\mu) p_{12} - \mu p_{11}] \times [S_x (x,y,z) + S_z (x,y,z)] \} \\ & + \frac{2n_{eff,0}\Lambda_{B,0}}{E} \times \{ S_z (x,y,z) - \mu [S_x (x,y,z) + S_y (x,y,z)] \} \end{aligned} \tag{5.18}$$

Eventually, upon strain – stress relationship, above deduction of FBG's birefringent photoelastic behavior can be further expressed in more explicit form [43]:

$$\frac{\Delta\lambda_{B,x}}{\lambda_0} = \varepsilon_z - \frac{n_{eff}^2}{2}\left[p_{11}\varepsilon_x + p_{12}\left(\varepsilon_y + \varepsilon_z\right)\right] \tag{5.19}$$

$$\frac{\Delta\lambda_{B,y}}{\lambda_0} = \varepsilon_z - \frac{n_{eff}^2}{2}\left[p_{11}\varepsilon_y + p_{12}\left(\varepsilon_x + \varepsilon_z\right)\right] \tag{5.20}$$